Design, Analysis, Fabrication, and Testing of a Nanosatellite Structure

Craig L. Stevens

Thesis submitted to the Faculty of the
Virginia Polytechnic Institute and State University
in partial fulfillment of the requirements for the degree of

Master of Science
in
Aerospace Engineering

Dr. Christopher D. Hall – Committee Chair
Dr. William L. Hallauer Jr. – Committee Member
Dr. Eric R. Johnson – Committee Member

May 28, 2002
Blacksburg, Virginia

Keywords: Satellite, Structural, Modal, Isogrid, Enviromental

Design, Analysis, Fabrication, and Testing of a Nanosatellite Structure

Craig L. Stevens

(ABSTRACT)

The satellite industry is undergoing a transition toward "smallsat" engineering. Small satellites are becoming more attractive to customers as a method of decreasing cost. As the launch costs remain relatively constant, the industry is turning towards nano–technology, such as microelectromechanical systems, and distributed satellite systems to perform the same missions that once required super-satellites. Nanosatellites form one group of these high risk/low cost spacecraft. The Virginia Tech Ionospheric Scintillation Measurement Mission, known as HokieSat, is a 40 lb nanosatellite being designed and built by graduate and undergraduate students. The satellite is part of the Ionospheric Observation Nanosatellite Formation (ION–F) which will perform ionospheric measurements and conduct formation flying experiments. This thesis describes the design of the primary satellite structure, the analysis used to arrive at the design, the fabrication of the structure, and the experimentation used to verify the analysis. We also describe the internal and external configurations of the spacecraft and how we estimate the mass properties of the integrated satellite.

The design of the spacecraft uses a composite laminate isogrid structure as a method of structural optimization. This optimization method is shown to increase the structural performance by over 20%. We conduct several finite element analyses to verify the structural integrity. We correlate these analyses with several static and modal tests to verify the models and the model boundary conditions. We perform environmental testing on the integrated spacecraft at NASA Wallops Flight Facility to investigate the properties of the structural assembly. Finally, we create a model of the ION–F stack to verify the integrity of the structure at the launch loads. We prove that the HokieSat structure will survive all environmental loads with no yielding or failures.

Acknowledgments

I would like to first thank Professor Christopher Hall for the opportunity to conduct such exciting research. I would also like to thank my committee members, Professor William Hallauer and Professor Eric Johnson, who guided me through the structural analysis and testing. I would like to thank Jana Schwartz who tirelessly provided assistance and leadership throughout the entire project. This research would not have been possible without the structures team members: Will Stacy; Ann Bergquist; Dan Rabin; and Scott Lennox. I would also like to thank the members of ION–F and the Air Force Research Laboratory for their constant technical assistance. I would like to acknowledge the work of Professor Alfred Wicks and his modal experimentation class in performing the isogrid assembly modal testing. I wish to thank the Aerospace and Ocean Engineering employees, specifically: Kent Morris; Bruce Stanger; and Mike Vaught for their assistance in the machine shop and throughout the design process. I would like to thank the people at NASA Wallops Flight Facility, including Glenn Maxfield and Rob Marshall, for their technical support during the environmental testing. I also wish to acknowledge Ray Pages and the NASA Goddard Space Flight Center for their support throughout the testing process. I also thank the sponsors of the HokieSat program who made the project possible: the Air Force Research Laboratory; the NASA Goddard Space Flight Center; the Space Dynamics Laboratory; the Air Force Office of Scientific Research; and the Defense Advanced Research Projects Agency. I would like to thank Walter Holemans and the Planetary Systems Corporation for their support throughout the development process. Finally, I wish to thank my family and friends whose support has enabled me to persevere through my six wonderful years at Virginia Tech.

Contents

List of Figures

List of Tables

List of Abbreviations

AFRL	Air Force Research Laboratory
AOE	Aerospace and Ocean Engineering
ASD	Acceleration Spectral Density
CAD	Computer Aided Drafting
CEE	Computer Electronics Enclosure
CGRO	Compton Gamma–Ray Observatory
CNC	Computer Numerical Controlled
CTE	Coefficient of Thermal Expansion
D/L	Downlink
FEM	Finite Element Model
FS	Factor of Safety
Hz	Hertz
ION–F	Ionospheric Observation Nanosatellite Formation
ksi	Kips Per Square Inch
MFS	Multifunctional Structure
MS	Margin of Safety
MSDS	Multi–Satellite Deployment System
NASA	National Aeronautics and Space Administration
PPT	Pulsed Plasma Thrusters
SAMPEX	Solar, Anomalous and Magnetic Particle Explorer
SHELS	Shuttle Hitchhiker Experimentation Launch System
STS	Space Shuttle
SUG	SHELS User's Guide
U/L	Uplink
X/L	Crosslink

Nomenclature

α	Isogrid Nondirectional Parameter
γ_{xy}	Shear Strain
ν	Poisson's Ratio
σ_1	Rib Stress (1–Direction)
σ_2	Rib Stress (2–Direction)
σ_3	Rib Stress (3–Direction)
σ_x	Isogrid Normal Stress (x–Direction)
σ_y	Isogrid Normal Stress (y–Direction)
τ_{xy}	Isogrid Shear Stress
a	Distance Between Node Centers
b	Width of Rib Web
d	Depth of Web
h	Height of Triangle
E	Young's Modulus
$\overline{E}$	Equivalent Young's Modulus
e_1	Uniaxial Bar Strains (1–Direction)
e_2	Uniaxial Bar Strains (2–Direction)
e_3	Uniaxial Bar Strains (3–Direction)
e_x	Isogrid Strains (x–Direction)
e_y	Isogrid Strains (y–Direction)
f_n	Natural Frequency
K	Isogrid Panel Extensional Stiffness
LX	Limit Load Factor (x–Direction)
LY	Limit Load Factor (y–Direction)
LZ	Limit Load Factor (z–Direction)
N_x	Membrane Stress Resultant (x–Direction)
N_y	Membrane Stress Resultant (y–Direction)
N_{xy}	Membrane Shear Stress Resultant
P_1	Uniaxial Bar Loads (1–Direction)
P_2	Uniaxial Bar Loads (2–Direction)
P_3	Uniaxial Bar Loads (3–Direction)
t	Thickness of Skin

Chapter 1

Introduction

The Virginia Tech Ionospheric Scintillation Measurement Mission, also known as HokieSat, is part of a student-built nanosatellite formation known as the Ionospheric Observation Nanosatellite Formation (ION–F) mission. Constraints that are unique to the university project and formation flying mission influence the design of the HokieSat structure. Mission constraints typically guide the design of any satellite structure. We begin this chapter by presenting an overview of previous space missions. We investigate how some of these past missions influenced the design of the respective satellites. We then describe the ION-F mission and its effect on the HokieSat structural design. Finally, we conclude this chapter with an overview of the thesis

1.1 Previous Satellite Missions

Satellites provide numerous services for modern society. They perform essential duties for military, governmental, and commercial organizations. The missions of these spacecraft include science ventures such as earth observation, interplanetary exploration, astronomy, and solar physics. They also include commercial endeavors such as television signal transmission, data transmission, and satellite telephone communication. In this section, we examine the history of science and commercial space missions. However, we omit the history of military missions due to the lack of available information.

The majority of the space science missions are performed by NASA–built spacecraft. The design and size of these spacecraft are highly dependent on the mission goals. These goals are constantly evolving due to changes in technology, political agenda, and budget. As a result, the design and size of satellites reflect these changes. This phenomenon is readily proven by examining the masses of civilian spacecraft launched throughout history. Figure 1.1 displays the launch mass of several NASA spacecraft as a function of time. The plot shows a gradual mass increase until the early 1990s at which point the spacecraft masses suddenly begin to decrease. This sharp decrease is primarily due to the change in policies

at NASA towards the "faster, better, cheaper" program [17] and a decrease in the overall NASA budget [32]. These smaller spacecraft are inherently less expensive to launch due to costs ranging from \$5K per kg to \$130K per kg [43]. The subsystems can therefore afford to take a high risk/low cost approach toward the design and offer less redundancy. This decrease in redundancy also decreases the overall cost and size of the spacecraft. NASA is now using constellations or formations of small-satellite systems to perform missions that once required large multi-million dollar spacecraft.

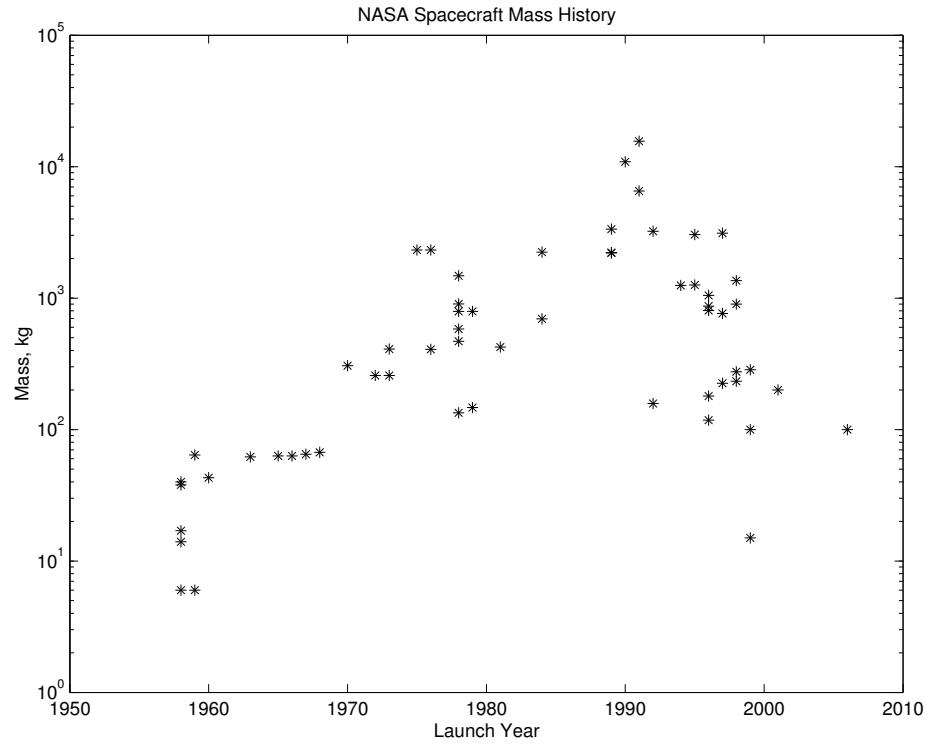

Figure 1.1: Launch Mass History of NASA Spacecraft

The commercial spacecraft industry has also evolved throughout history, as shown in Figure 1.2. However, the masses have not decreased as significantly due to several factors. A major factor for this trend are the high gain antennas and large power requirements inherent to the communications satellites placed in geosynchronous orbit. The communications industry has long exploited the phenomena of "fixed" geosynchronous spacecraft to provide a stationary signal to it's ground-based antennas. This current practice appears to be changing, however, as distributed spacecraft systems become more prevalent (*e.g.* XM radio, Globalstar, etc.).

As we have shown, the satellite industry has transformed to match the ever–changing environment of technology. Spacecraft mass, as a result, has also demonstrated this trend. We now discuss some examples of key spacecraft that accurately define the history of the industry.

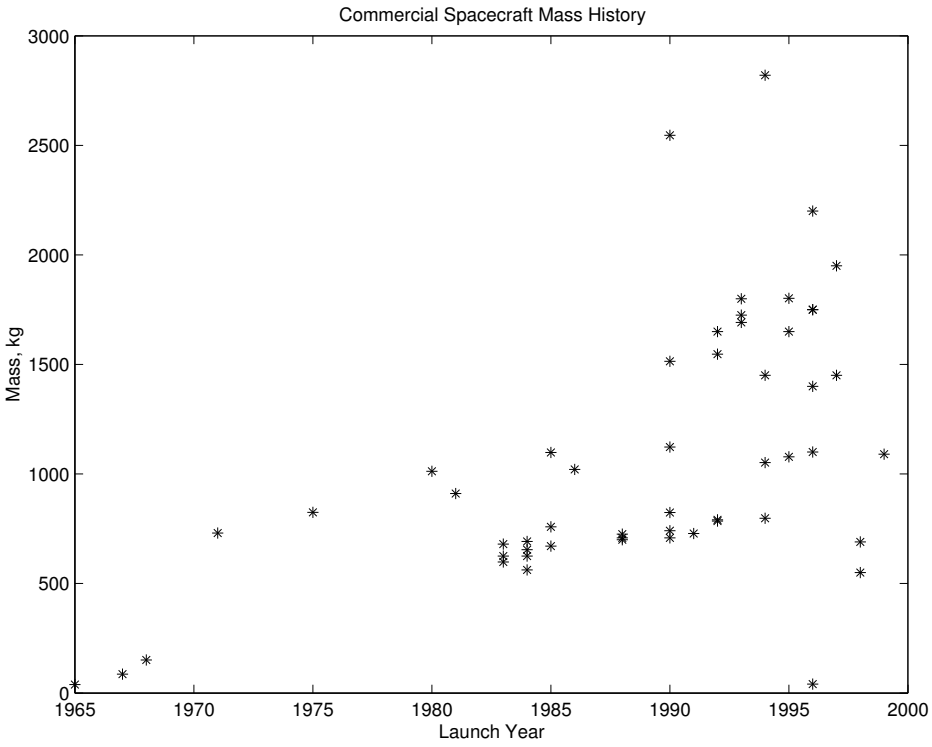

Figure 1.2: Launch Mass History of Commercial Spacecraft

1.1.1 NASA Missions

Explorer 1, shown in Figure 1.3, was the first United States (US) satellite. It was launched by the US Army on January 31, 1958 aboard a four–stage version of a Jupiter C rocket. It was placed into a 224 $\times$ 1575 mi orbit at 65° inclination. The spacecraft measured approximately 6 ft long (including the rocket case structure) and weighed 31 lb. The payload weighed 18 lb and recorded cosmic rays and micrometeoroids. It also discovered the Van Allen Belt, an area of intense radiation beginning 965 km above the surface of the earth, and made contributions to theoretical spacecraft dynamics. The success of the Explorer 1 mission provided an impetus to continue the Explorer program. The program was turned over to NASA at the creation of the agency in October of 1958 and has amassed over 75 launches [44].

The Compton Gamma–Ray Observatory (CGRO) was one of the largest NASA astronomical spacecraft ever to launch (see Figure 1.4). It was launched on April 5, 1991 aboard the Space Shuttle into a low–earth–orbit (LEO) approximately 280 mi in altitude. The observatory was safely deorbited on June 4, 2000 after nine years on orbit. It measured 25 ft long by 12.5 ft in diameter and weighed 34,371 lb. The program was conceived in 1978 with a payload containing four instruments: Oriented Scintillation Spectrometer Experiment (OSSE), Imaging Compton Telescope (COMPTEL), Energetic Gamma–Ray Experiment Telescope (EGRET), and Burst and Transient Source Experiment (BATSE). The instruments were

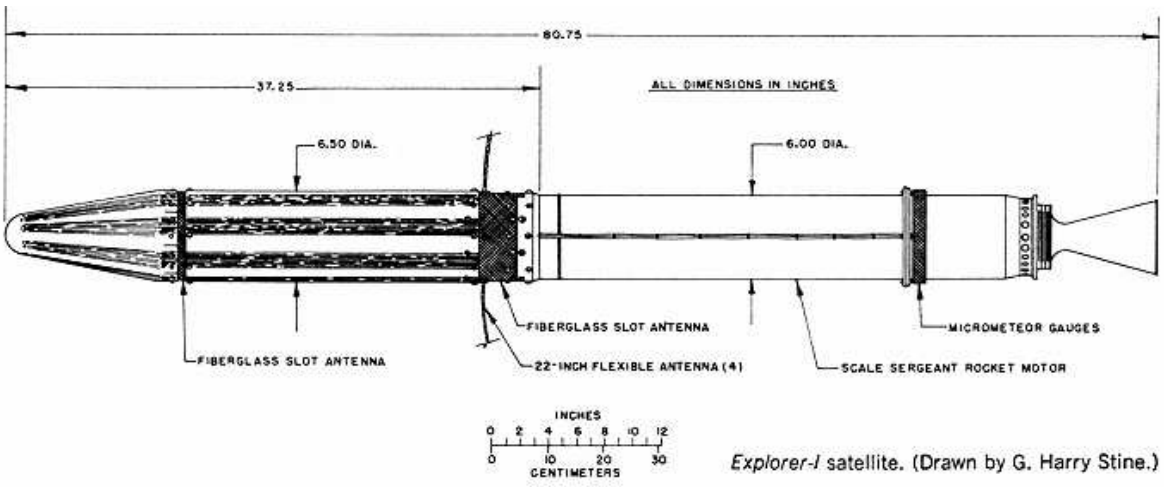

Figure 1.3: Sketch of Explorer 1 [24]

designed to gather data on the most energetic form of radiation known. The long schedule, massive size, and sensitive instrumentation all contributed to the immense development budget of $557 million [44].

Figure 1.4: Compton Gamma–Ray Observatory [24]

The Solar, Anomalous and Magnetic Particle Explorer (SAMPEX) marked a turning point in the NASA satellite design program towards the "faster, better, cheaper" philosophy [32]. The spacecraft, shown in Figure 1.5, was launched into a 342 × 420 mi altitude, 82° inclination orbit on July 3, 1992 aboard a Scout. The satellite weighed approximately 348 lb and measured 4.9 ft in length and 2.8 ft in diameter. The mission goals included

observing and measuring galactic charged particles and cosmic rays. The spacecraft was part of the Small Explorers (SMEX) program which is designed to provide low cost, rapid turnaround LEO science missions. It preceded several other similar satellites in the program such as the Sub-mm Wave Astronomy Satellite (SWAS), the Fast Auroral Snapshot Explorer (FAST), the Transition Region and Coronal Explorer (TRACE), and the Wide–Field Infrared Explorer (WIRE) [44].

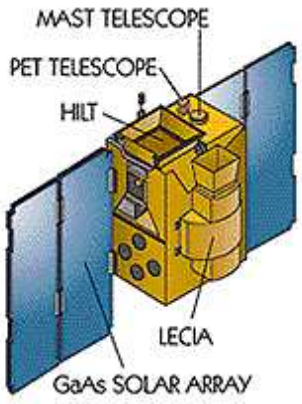

Figure 1.5: SAMPEX External Configuration [24]

The Explorer 1, CGRO, and SAMPEX missions all incorporated unique satellite structural designs. Commercial spacecraft initially used the same design concept due to a lack of space heritage. However, expansion of the satellite communications market required companies to become more productive and efficient. As a result, satellite manufacturers began to design structures that were more modular and robust. We next discuss some key commercial satellite missions that are representative of this trend.

1.1.2 Commercial Missions

Intelsat 1 was the first commercial communications satellite. It was launched to geosynchronous orbit over the Atlantic on April 6, 1965 aboard a Delta rocket. The spacecraft measured 2 ft in length and 2.3 ft in diameter and weighed 85 lb. The satellite allowed more accessible transatlantic telephone communications and made scheduled transoceanic television possible. It was reactivated in 1984 in celebration of the organization's 20th anniversary. This spacecraft was the first of over 23 to be put on orbit by the Intelsat organization. Currently, the organization is a commercial cooperative of over 136 nations and corporations that provide international and transoceanic telecommunications support [44].

The Globalstar constellation consists of 48 spacecraft that work cooperatively in a distributed satellite system. The spacecraft were launched in several installments by Boeing

Satellite Systems. The satellites, shown in Figure 1.6, weigh 988 lb and were designed such that four can be launched simultaneously aboard a Delta class rocket. The constellation is configured with six spacecraft in eight orbital planes. The orbits have an altitude of 764 nm and inclination of 52°, with arguments of perigee chosen for optimal ground coverage.

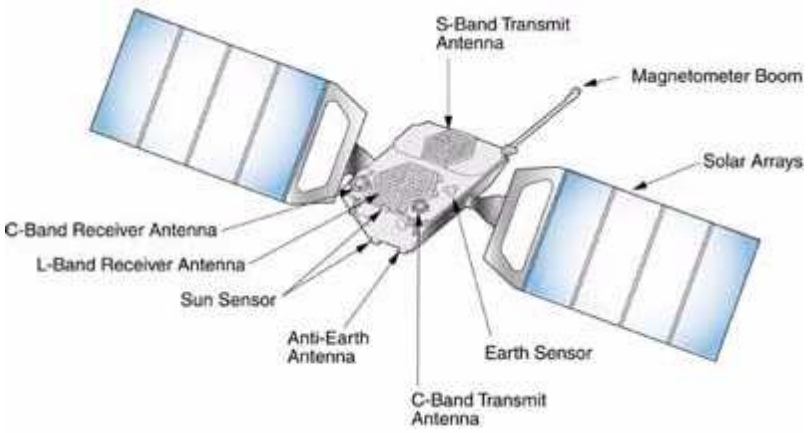

Figure 1.6: Schematic of Globalstar Satellite Configuration [5]

The ORBCOMM spacecraft constellation is the world's first commercial communications constellation. It consists of 35 spacecraft with a mission goal to provide a global two–way data messaging system. The satellites were launched into six distinct orbital planes with altitudes ranging from 484 mi to 621 mi between 1995 and 2000. All satellite designs use the Orbital Sciences Corporation's Microstar spacecraft platform. The Microstars are configured as circular cylinders measuring 40 inches in diameter and 6 inches in height and weighing 99 lb. The compactness of the design allows for integration aboard a Pegasus XL rocket in an eight–satellite stack configuration (see Figure 1.7). The configuration combines the launch cost of several individual satellites. The ORBCOMM spacecraft constellation demonstrates a possible commercial market for distributed small–satellite systems [27].

1.2 ION-F and HokieSat Mission

HokieSat is part of a three-satellite formation known as the ION–F mission. The ION–F mission is comprised of three nanosatellites designed and built by students at the University of Washington (Dawgstar), Utah State University (USUSat), and Virginia Tech (HokieSat). The program provides technology demonstration for future high risk, low cost nanosatellite formation missions such as TechSat21 [7]. The mission includes several nano–technology

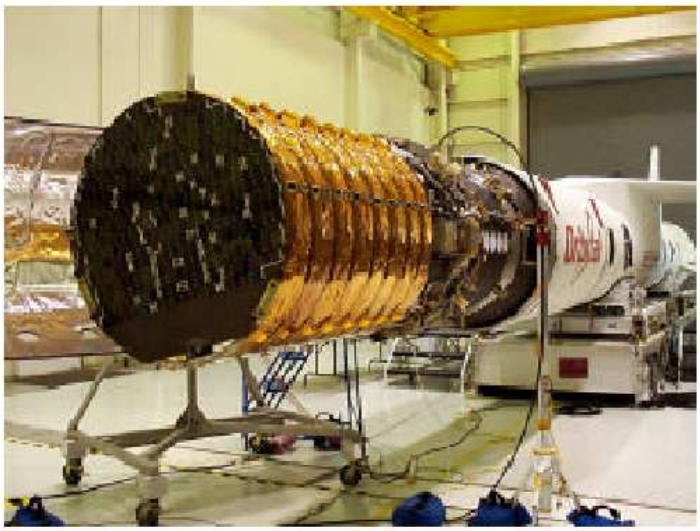

Figure 1.7: ORBCOMM Microstars Aboard a Pegasus Rocket [27]

demonstrations, three-dimensional mappings of the ionospheric scintillation effects on global positioning system (GPS) signals, and ionospheric plasma density measurements. The formation flying mission requirements dictate that the three spacecraft have nearly identical initial conditions [7]. Therefore, the formation must be launched aboard the same launch vehicle. The launch vehicle chosen for this mission is the Shuttle Hitchhiker Experiment Launch System (SHELS), via the Space Shuttle (STS). Due to safety issues and tracking limitations, NASA prohibits the nanosatellites from deploying separately from the Shuttle Orbiter Payload Bay. The solution to the safety issues is the Multiple Satellite Deployment System (MSDS) designed by AFRL (see Figure 1.8). The MSDS is designed as an operational platform that supports nanosatellites in a stack configuration aboard the SHELS[6]. Use of the MSDS allows ION-F to be deployed from the SHELS in an unpowered state, which helps address many of the STS safety requirements. The ION-F launch configuration consists of the three nanosatellites mounted to the MSDS in one stack. The mission profile calls for the MSDS to deploy from the SHELS with the stack mounted to the platform. While in this mode of operation, the MSDS issues a signal to release the power inhibits on the nanosatellites and provide power to the electrical components to perform satellite–level check–outs. Once a specified time has elapsed, the stack is ejected from the MSDS and stabilizes itself using permanent magnets aboard USUSat. The desired attitude in this mode is the unstable equilibrium with the stack minor axis aligned in the ram, or velocity vector, direction. Finally, after an initial system checkout with the specified ground station, the ION-F nanosatellites separate from each other and begin the formation flying mission [37].

The three satellites, University of Washington's Dawgstar, Utah State's USUSat, and Virginia Tech's HokieSat, are all hexagonal prisms weighing between 33 and 44 lbs. The configuration of each satellite varies slightly based on the formation and nanosatellite mis-

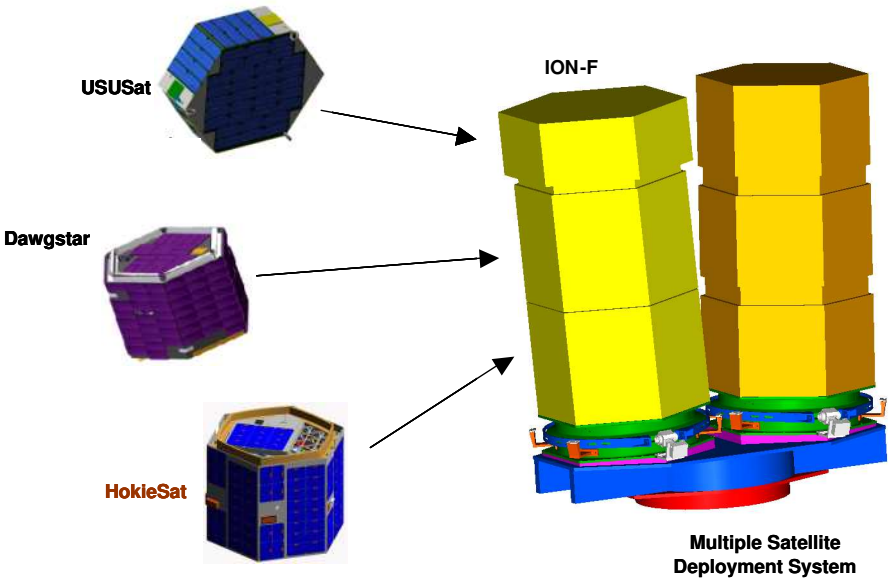

Figure 1.8: The MSDS Configuration [6]

sion requirements. The HokieSat configuration is also strongly influenced by the structural requirements because of its position at the base of the ION-F stack.

The basic design of the HokieSat structure is a hexagonal prism 18 inches in major diameter, and approximately 12 inches in height. The structure is designed to support the components that are essential to perform the mission. Along with the ION-F formation flying and science goals, HokieSat will demonstrate several low cost/high risk nano–technologies such as micro-pulse plasma thrusters for orbital control, torque coils for attitude control, GPS crosslink for orbit determination, and digital cameras for attitude determination. All of these mission goals are accomplished along with the main mission goal of producing a low cost/high risk nanosatellite with high student involvement.

1.3 Thesis Overview

This thesis describes the design, analysis, fabrication, and testing of the Virginia Tech HokieSat structure. We examine several previous satellite designs and their influence on the existing HokieSat structural design. The mission of the spacecraft and its effects on the satellite design are also described. We present the design variables that determine the internal and external configurations. We provide a comprehensive description of each stage of

the HokieSat development.

In Chapter 2 we review the history of spacecraft structures with a focus on isogrid applications. In Chapter 3 we describe the HokieSat structural design. We include the design process and objective function analysis that were used in the optimization process. In Chapter 4 we describe the manufacturing techniques used to fabricate the primary structure and the methods used to protect the satellite in transit and on-orbit. Chapter 5 presents the analyses and tests that were performed to verify the structural design. We include both preliminary analysis, and stress, buckling, and modal analyses performed using I-DEAS software. We also demonstrate the accuracy of the model using correlation with static, modal, and vibrational experiments. Finally, in Chapter 6 we close this investigation with a summary of the results and lessons learned throughout the qualification process.

Chapter 2

Literature Review

The purpose of this chapter is to review several basic concepts from the areas of satellite design. We begin with a literature review of previous satellite structural designs. We include conventional spacecraft design methods and materials. We conclude the literature review chapter with a review of research on isogrid structures. Although many past satellite structural design trends are included in this chapter, we focus primarily on trends most relevant to this mission.

2.1 Previous Satellite Structures

Aerospace structures generally require lightweight designs. The goal of these designs is to optimize the strength per weight, or efficiency of the design. Satellite structural design has evolved greatly over the past four decades. Traditionally, efficiency has been accomplished using a combination of various structural designs and materials. We begin this section by discussing basic primary structural designs and conclude by presenting traditional materials used in spacecraft.

2.1.1 Conventional Structural Designs

Primary structures are designed using several criteria that depend on the mission requirements. Conventional spacecraft incorporate 4 basic primary structural designs: 1) skin–frame structures; 2) truss structures; 3) monocoque cylinders; and 4) skin–stringer structures [31].

The skin–frame structural design uses an interior skeletal network of axial and lateral frames to mount exterior skin panels using fasteners or rivets. The frames support bending, torsional, and axial forces. The skin reinforces the structure by supporting the shear forces introduced by the interior member connections. The skin is sometimes minimized to save mass, even though the thin skin leads to some structural instabilities. When the skin

buckles due to shear, it transfers all additional shear loading to in–plane tension forces at 45° which must be supported by the connections. The buckling modes of the skin exhibit large deformations that make it insufficient for exterior mounted components such as solar cells. The buckling strength of the assembly is typically increased by adding intermediate members [31].

Truss structures use an array of members that can only support axial loads. Truss members are produced independently and arranged typically in arrays of triangles for stability. The members are manufactured using extruded tubes made of composite, metallic, or sheet metal materials. A stable truss is statically determinate and has no excess members to introduce alternate load paths. Trusses are generally mass–efficient when the members are configured into rectangular or triangular cross–sectional assemblies. However, they become less efficient as the cross-section becomes more circular or hexagonal. Also, the design of the structure creates inherent stress concentrations at interface mounting points, such as separation systems. Components may be mounted both internally and externally and the absence of shear panels enables easy access to a payload. However, this absence of shear panels is not helpful to spacecraft requiring body mounted solar cells [31].

Monocoque cylinders are axisymmetric shells that do not contain any stiffeners or frames. The shells are manufactured using metallic or sandwich panels with curved sections formed by rolling. Typically, two or three curved sections are fabricated and assembled into the cylindrical configuration. The strength of monocoque cylinders is usually limited by its buckling strength. The shells are most efficient when the loads are distributed evenly throughout the structure. Components are typically mounted to the walls using fasteners; however, care must be taken not to overlaod the shell and cause local failures. The monocoque cylinder design is applicable to spacecraft with body mounted solar cells and relatively lightweight components [31].

Cylindrical skin–stringer structures are designed using axial and lateral frame members attached to an outer skin. These designs are similar to skin–frame structures; however, this class of structures refers to circular cylinder configurations. The skin is sometimes minimized to save mass, even though the thin skin leads to some structural instabilities. The post–buckling behavior of the skin transfers the additionally applied shear loads to torsion by the diagonal tension phenomenon described above. The skin and members must attach uniformly to enable the assembly to act as a continuous structure. Typical connection methods include fasteners and/or rivets. Interior components are usually mounted to the walls at locations along the stringer assembly. This method is more efficient than monocoque cylinder component mounting at introducing local loads. The skin must be designed sufficiently stiff to enable sound mounting of exterior entities such as body mounted solar cells [31].

2.1.2 Materials

Satellite structural designs also use several different materials. Materials are chosen based on their properties, cost, and complexity. There are two typical materials used in spacecraft

applications: metals and fiber composites.

Metals

Aluminum alloys are the most widely used metallic materials in spacecraft manufacturing [43]. The advantages include high strength to weight ratios, high ductility and ease of machining. The stiffness to weight ratio is comparable to steel; however, the strength to weight ratio is typically higher. The disadvantages include low hardness and a high coefficient of thermal expansion (CTE). The alloys are typically tempered to increase the material strengths. Two typical alloys used in manufacturing are 6061-T6 and 7075-T7. Aluminum 6061-T6 contains silicon and magnesium which strengthens the alloy during tempering. This alloy has good machinability and corrosion resistance. Aluminum 7075-T7 contains zinc and trace amounts of magnesium. The alloy exhibits higher strength than 6061-T6, but is more difficult to machine [22].

Beryllium is used for very high-stiffness aerospace applications. It has a specific modulus 6.2 times the specific modulus of aluminum [8]. The material is non-isotropic due to its grain alignment and therefore exhibits low ductility and fracture toughness in its short–grain direction. It is commonly used in lightweight optics and mirrors because it performs well at cryogenic temperatures (*i.e.* low CTE and high thermal conductivity). However, beryllium is expensive, difficult to machine, and sparsely available in the US. Beryllium must be machined in a controlled environment because its powder is a known carcinogen when inhaled. The parts may be safely handled once machined [31].

Steel is mainly used in aerospace applications where low–volume strength and stiffness are important. Steel provides high wear resistance; however it is generally difficult to machine and is not efficient for structural stability. Steels are combined with many trace elements to address a wide range of needs. Austentic stainless steel is by far the most abundant steel alloy used in spacecraft. It contains 12% chromium which results in a tough chromium–oxide coating that protects parts from corrosion. Stainless steel is non-magnetic and certain low–carbon alloys can be welded without sensitization. Stainless steels are generally used for fasteners and mechanisms whereas many heat–resistant alloys are used for heat shields, rocket nozzles, and other high–temperature applications [31].

Titanium and titanium alloys are used for applications requiring very high strength materials. The materials exhibit high strength to weight ratios, low coefficients of thermal expansion, and excellent corrosion resistance [43]. However, they are difficult to machine and some alloys exhibit poor fracture toughness. Ti-6Al-4V, which contains 6% aluminum and 4% vanadium, is the most popular titanium alloy used in aerospace applications. The alloy has heritage in wings and missile bodies. Perhaps its most famous applications are the castings used to connect the external fuel tank to the Space Shuttle and its boosters [22].

Fiber Composite Structures

Composite structures consist of a matrix and a reinforcement. The matrix (metal, epoxy) binds the reinforcing fibers (carbon, graphite) together into a continuous system. The efficiency of composite structures is due its high specific modulus and unique load path. The flexural shear loads are transferred from the matrix to axial loads on the high–strength fibers, creating a structure 3 to 5 times as stiff as aluminum at 60% of the mass [31]. These fibers may be both discontinuous or continuous entities. Discontinuous–reinforced composites are comprised of ceramic or fiber particles that are randomly distributed throughout the matrix. Aluminum reinforced with silicon carbide particles is the most widely used discontinuous composite. The majority of continuous–fiber composites are generally called laminate composites. Laminate composites are manufactured from several layers of woven fibers called laminae. The laminae are composed of several parallel fibers arranged in sheets. The sheets themselves are anisotropic and have few structural applications. However, stacking several of the laminae with fibers aligned at different angles, called lamina angles, creates a more stable laminate composite structure. The laminate may be customized for individual applications by varying the fiber type and the layup. For example, some graphite/epoxy laminates are tailored to have a nearly zero CTE and others may be laid up to exhibit extraordinary specific stiffness properties. Polymer–matrix composites (PMCs) are the most widely used continuous–fiber composites used for spacecraft. The matrices consist of two polymers: thermoplastics, and thermosets. Thermoplastics may be remelted and solidified multiple times whereas thermosets are not reusable after curing. These properties enable a multitude of bonding techniques and layup procedures, many of which are currently proprietary. The downside to fiber composite structures is the large development cost required for reliable manufacturing. The large cost is due to the sensitivity of adhesive bonding to process variables. This sensitivity makes each part a unique entity which must be tested to verify strength. NASA and other programs require extensive testing of fiber composite flight hardware to verify its structural integrity. The requirements typically create the need to fabricate a protoflight structure dedicated to qualification testing followed by acceptance testing of the flight article. This qualification procedure presently prohibits the use of fiber composite structures on small–budget programs [31].

2.2 Structural Optimization Methods

Several methods are available to optimize the structural properties of spacecraft. The optimum method may vary depending on the design task. We present three of the most widely used methods: sandwich structures, multifunctional structures, and isogrid. We examine all of the technologies and their benefits for satellite structural designs. We conclude with a description of isogrid and a literature review of past research conducted in this field.

2.2.1 Sandwich Structures

Sandwich structures are often used in skin-frame designs. A sandwich structure consists of two thin face sheets attached to both sides of a lightweight core. The design of sandwich structures allows the outer face sheets to carry the axial loads, bending moments, and in-plane shears while the core carries the normal flexural shears [31]. Sandwich structures are susceptible to failures due to large normal local stress concentrations because of the heterogeneous nature of the core/face sheet assembly. Component mounting must therefore use potted inserts to distribute the point loads from connections. Sandwich panel face sheets are commonly fabricated using aluminum or graphite/epoxy composite panels. The core is typically fabricated using a honeycomb or aluminum foam construction.

Honeycomb sandwich panelling is the lightest option for compressive or bending loading specific applications [31]. Honeycomb sandwich cores are manufactured using thin strips formed into honeycomb cells. The honeycomb geometry is non–isotropic with greater stiffness in the longitudinal direction [43]. However, the core acts nearly isotropically for in–plane loads when assembled in a sandwich configuration. The disadvantages of using honeycomb cores are the potted inserts required for mounting and the thermal inefficiencies. These inefficiencies stem from the low thermal conductivity of the adhesive layers used in construction and make honeycomb prohibitive in optical and mirror aerospace applications.

Aluminum foam sandwich panels use a porous aluminum foam material for the core. The flexural shear stiffness dominates the overall panel stiffness for relatively small panels (*i.e.* less than 50 inches) [8]. Therefore, the core design is an integral part of the sandwich panel design for small spacecraft. The shear stiffness of foam core sandwich panels is generally less than that of honeycomb core sandwich panels of equal mass. However, radial ribs and shear rings may be embedded in the core to overcome the low shear stiffness. A major benefit of aluminum foam construction is an increase in thermal efficiency because the core may be brazed to aluminum facesheets rather than epoxied [8]. Brazing provides a continuous thermal path through the material which benefits applications such as cryogenic mirrors and solar arrays.

2.2.2 Multifunctional Structures

Multifunctional structure (MFS) technology incorporates several functions into the primary structure of a spacecraft. The main goal of these members is to minimize parasitic mass by incorporating chassis, cables, connectors and thermal control components into the satellite primary structural walls (see Figure 2.1). The walls are typically constructed out of fiber composites or sandwich panels, and the electrical components are embedded during manufacturing. The traditional ground plane/printed circuit board design is performed by copper/polymide (CU/PI) patches, multi-chip modules (MCMs), and the current cabling functions are performed using CU/PI flexible jumpers. The design allows for an easily-accessible, removable, and modular electrical system [13]. The benefits of this technology

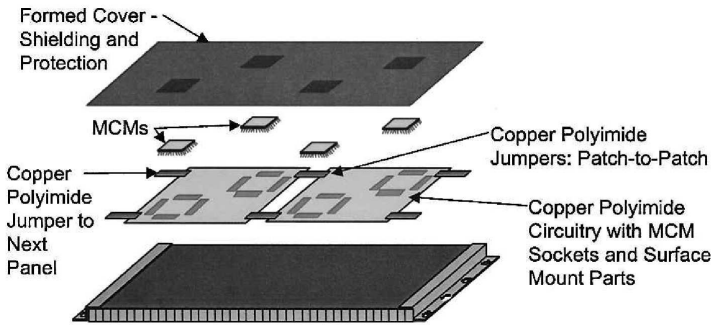

Figure 2.1: Schematic of MFS Configuration [13]

include a 70% reduction in electronic enclosures and harnesses, a 50% reduction in spacecraft volume required for these conventional components, a reduction in labor required for spacecraft assembly, and an extremely robust system with wide applicability to several missions [3]. Lockheed Martin has recently proven the technology as an experiment aboard the Deep Space 1 mission [13].

2.2.3 Isogrid Structures

Isogrid uses an array of equilateral triangle cutouts to increase the stiffness per weight of a structure. The pattern may be manufactured by machining a metallic panel, or it may be constructed using fiber composite materials. The concept began in the early 1960s using metal structures and development continues today with research focusing primarily on composite applications.

The Isogrid Design Handbook [23] is considered the foremost guide to isogrid structural design. The handbook contains the results of a study conducted by Dr. Robert Meyer beginning in 1964. The investigation examined optimum stiffening patterns for compressively loaded dome structures. The study determined that isogrid is an efficient stiffening technique for dome structures and the work was later extended to include plates and cylinders. This work led to application of the technique to Delta vehicle tanks, interstages, shrouds, and Orbital Workshop interiors.

The handbook presents the advantages of the isogrid design and the typical design situations when application of the technique is beneficial. It also defines the isogrid notation used in nearly all of the modern literature. The theory for the sizing and analysis of isogrid is presented and the manufacturing techniques are discussed. Correlation of the analysis results and the structural testing results obtained for the Delta launch vehicle are discussed to further verify the isogrid structural concept. This literature focuses primarily on the use of isotropic materials, such as metals; however, the basic geometrical theory can be applied similarly to composite materials.

Paul Slysh authored several papers and articles concerning analysis and manufacturing of isogrid structures in the 1970s and 1980s. Slysh conducted research on CNC manufacturing of aluminum circular cylinders [34], and buckling analysis and testing correlation [35]. He also demonstrated several uses of isogrid for structural applications.

The Isogrid Microspacecraft Structures Final Report [36] presents the design, analysis, and fabrication guidelines developed in the manufacturing of an aluminum isogrid spacecraft. The preliminary design and analysis were performed using the Isogrid Design Handbook. Modifications were made to the isogrid array and it was shown that the modifications had a negligible effect on the overall structural efficiency. The effectiveness of isogrid fabrication for small organizations was demonstrated using Computer Numerical Controlled (CNC) milling. Static testing data was correlated with the finite element model to investigate methods of mass savings.

Lauer *et al* [21] authored a technical paper describing the design, analysis, fabrication, and testing of an aluminum isogrid instrument mounting platform. The mounting platform was developed to support a meteorological optical instrument and sensor with stringent pointing requirements. The paper includes a trade study of an isogrid design versus a honeycomb sandwich design. The results indicate that aluminum isogrid outperforms honeycomb sandwich panels for this application because the sandwich panels exhibits a lack of peel strength, high stress concentrations from mounting points, poor thermal conduction without the use of thick face sheets, and poor thermal field–of–view to the instrument base plate. Several instruments mounted to the isogrid platform using the node attachment points and interface brackets. The paper presents the static and dynamic analyses performed and correlated with vibrational testing to verify the integrity of the panel.

Several technical papers and journal articles have been written regarding the design, analysis, and manufacturing of fiber composite isogrid structures. The Air Force Research Laboratory has researched fiber composite isogrid development since the early 1990s [20]. Thomas Kim has extended AFRL's research on analysis and fabrication techniques of composite isogrid panels [10] and cylinders [18]. Kim and AFRL developed fiber composite isogrid solar panel substrates for use on the Clementine spacecraft [19]. Parametric studies were undertaken to demonstrate the feasibility of the isogrid panels for solar array applications. As a result of these studies, fiber composite isogrid structures were shown to outperform honeycomb sandwich structures in stiffness, mass, cost, and thermal properties.

Dorsey *et al* [9] conducted a trade study of two concepts for an aerobrake hexagonal heat shield design. One concept is a sandwich panel construction with an aluminum honeycomb core and graphite/epoxy face sheets and the other concept is a graphite/epoxy skinned isogrid construction. The panels were compared using linear static, linear buckling, and nonlinear static analyses. Detailed presentation of the analysis was presented and the honeycomb sandwich panel was found to be superior for this application. We use this paper as a primary resource for finite element modeling of the isogrid structure.

NASA Langley Research Center, TRW, and Composite Optics, Inc. conducted a research and development program to evaluate the benefits to using fiber composite isogrid

for spacecraft components [33]. The study demonstrated that there are benefits to using composite isogrid for several applications such as solar array substrates, equipment avionics panels, and high frequency RF reflectors. The results further reinforce the results from the AFRL study by test/analysis correlation.

Several other resources are available to investigate the structural analysis of composite isogrid cylinders and panels. Research has been conducted in the fields of linear bifurcation and nonlinear buckling of these structures; for example Wang *et al* [41] conducted post–buckling and linear bifurcation analysis in parallel with experiments and Zhang [46] developed geometric and material nonlinear post–buckling equations for composite isogrid cylinders. Huybrechts and Tsai [16] investigated the effects of nodal offset and grid structure weaknesses such as missing ribs. Lockheed Martin, AFRL, and NASA have also conducted research on composite isogrid cylinders for future Space Shuttle fuel tank applications [28]. Estimations of the compaction forces necessary to maintain structural integrity of the cylinders were found using material nonlinear finite element analysis. Compaction forces are applied to the composite during lay–up and are difficult to exact in practice. These forces are related directly to the structural integrity of composite isogrid cylinders.

2.3 Summary

In this chapter we presented a literature review investigating past satellite structural designs. We described basic primary structural designs and the materials widely used in spacecraft structural design. We examined the advantages and disadvantages of each design and material. We also presented literature describing structural optimization methods. We included a review of modern optimization methods, such as multifunctional structures, and conventional optimization methods, such as sandwich and isogrid panels. Finally, we presented a detailed review of past research conducted in the field of isogrid structures. In the next chapter we use this information to design the structure of HokieSat.

Chapter 3

Structural Design

The development of any structure begins by establishing a design. In this chapter, we describe the process used to create the structural design of HokieSat. We begin with a description of the major design constraints that guided the mechanical design. We present the preliminary objective function analysis and results used to create a preliminary design. We also present the iterative design procedure used to create the current design. We then describe the configuration and the composite isogrid structure design.

3.1 Design Procedure

The current design procedure began when the Ionospheric Observation Nanosatellite Formation was established. The first step in the design procedure was to size the general spacecraft configuration due to the large number of organizations involved in the mission. The ION-F nanosatellites were configured as hexagonal cylinders with dimensions resembling the figures stated in Chapter 1 to minimize the inherent complications of integration. The hexagonal configuration allowed selection of a uniform separation system between the spacecraft.

The next step required a selection of the basic primary structural design. We rated the four basic designs studied in the literature review and decided to use a modified monocoque cylinder structure. We chose this design because the monocoque design had heritage in nanosatellite structures and was readily applied to our program [31, 36, 11, 45]. The design enabled a body–mounted solar cell configuration and allowed mounting of the relatively lightweight components to its side panels.

The next step in the design process was to select the optimum material for the primary structure. We presented the large number of panel materials with space heritage available for satellite structural design in the literature review. To reduce this number, we performed a parametric study and reduced the number of primary structural materials to three: 1) solid metallic panel, 2) honeycomb sandwich panel, and 3) fiber composite panel. We then evaluated each of these materials in more detail based on several design criteria. We chose

these standards by applying a list of design parameters described by Grooms, Debarro, and Paydarfar [12] to the unique programmatic and structural issues of the project. The design criteria selected for the mission are shown in Table 3.1. The list was modified to include student involvement in the spacecraft development, which is an integral goal of the HokieSat mission.

We subsequently constructed an objective function to evaluate the performance of each remaining material simultaneously. Each material was given a score, S_j, for each of the criteria ranging from 0.0 to 10.0 based on results of the literature review and comments from various specialists [14, 42]. The total score of the material design is thus calculated using equations 3.1 and 3.2:

$$S_{total} = \sum_{j=1}^{11} (W_j S_j) \tag{3.1}$$

The weighting factors, W_j, were chosen using the following constraint to ensure an objective and efficient analysis:

$$\sum_{j=1}^{11} W_j = 1.00 \tag{3.2}$$

A sensitivity analysis was conducted on the objective function using three weighting conditions. The first condition was that of a general structural engineer. Here we distributed most of the weights equally with an emphasis placed on the mechanical properties of the structure. The second condition was based on the viewpoint of the chief engineer. This viewpoint also distributed the weighting factors relatively evenly; however an emphasis was placed on low mass and project scheduling. The final condition placed an emphasis on rating the amount of student involvement resulting from application of the specified material. The three conditional weighting factors are presented in Table 3.2 and the preliminary design results are displayed in Table 3.3. The objective function clearly demonstrates that metallic panels are the most effective structural design for our project. There were several reasons for this decision. Fiber composite structures are expensive to manufacture and require costly structural testing. The honeycomb sandwich panels require potted inserts to attach fasteners which create safety concerns and parasitic mass. The metallic panels are relatively simple to manufacture and minimize the safety and testing requirements. Metallic panels also allow greater student manufacturing and handling.

The next step in the design process was to develop an optimum metallic plate design. Several metals are used in satellite fabrication, such as aluminum, titanium, beryllium, and stainless steel, which were discussed in detail in Chapter 2. These materials vary in cost, manufacturing time, mass, strength, durability, and required craftsmanship. Aluminum 6061 T–651 was selected as the primary material in the spacecraft structure for several reasons. The material is relatively abundant and economically feasible for a low budget program. It has a density of approximately 0.1 lb/in^3 which is roughly one third the density of steel and other metals used in manufacturing. Finally, aluminum is simple to manufacture and has relatively good workability [22]. Good workability is an important advantage to consider for a small budget program, which must minimize cost by using university machine shops, and

Table 3.1: Design Criteria Scores for Materials

j	Criteria	Metallic	Honeycomb Sandwich	Fiber Composite
1	Mass	9.0	9.5	10.0
2	Design/development/test cost	9.0	9.0	7.0
3	Student involvement	9.0	8.5	8.0
4	Ease of fabrication/assembly	8.5	9.0	8.5
5	Ease of subsystem/integration	8.0	9.0	8.5
6	Ease of inspection/repair	10.0	8.5	8.0
7	Availability of material	10.0	9.0	8.0
8	Thermal performance	9.5	8.5	9.0
9	Test requirements	9.5	8.0	6.0
10	Analysis techniques available	9.0	8.5	8.0
11	Operations schedule	9.0	9.0	8.5

Table 3.2: Distribution of Weighting Factors for Each Condition of Sensitivity Analysis

j	Criteria	Condition 1	Condition 2	Condition 3
1	Mass	0.15	0.20	0.05
2	Design/development/test cost	0.10	0.20	0.10
3	Student involvement	0.10	0.05	0.20
4	Ease of fabrication/assembly	0.10	0.10	0.20
5	Ease of subsystem/integration	0.10	0.05	0.10
6	Ease of inspection/repair	0.05	0.05	0.10
7	Availability of material	0.05	0.05	0.05
8	Thermal performance	0.10	0.10	0.05
9	Test requirements	0.10	0.05	0.05
10	Analysis techniques available	0.10	0.05	0.05
11	Operations schedule	0.05	0.10	0.05

Table 3.3: Objective Function Results

Condition	Metallic	Honeycomb Sandwich	Fiber Composite
1	9.050	8.850	8.175
2	9.075	8.975	8.300
3	9.075	8.975	8.300

relatively inexperienced students to perform the majority of the machine work.

The next consideration in the design process was optimizing the structural and mass properties of the spacecraft. The optimal structural design chosen for HokieSat was isogrid. Isogrid, illustrated in Figure 3.1, uses an array of equilateral triangle cutouts to increase the structural performance of a flat sheet of material. Ideally, machining an isogrid pattern reduces the mass of the original plate by approximately 75% and reduces the strength of the plate by approximately 25%. Nominally, this procedure may produce a 200% increase in structural efficiency compared to the original flat plate [36]. Another advantage to machining the triangle array is that the plate remains isotropic [23]. Therefore, it exhibits similar strength in all directions and locations of stress concentrations are minimized. We conducted a preliminary analysis, described in Chapter 5, to size the isogrid and establish the preliminary design of the spacecraft.

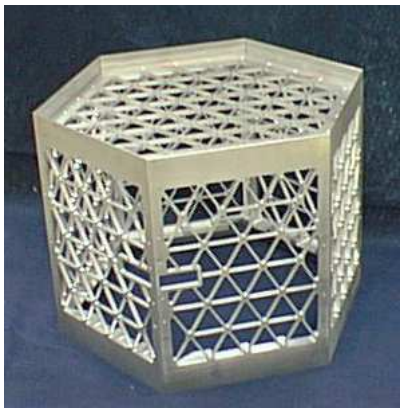

Figure 3.1: Photograph of HokieSat Isogrid Structure

In the final steps of the design process, we implemented an iterative method of design optimization similar to the method proposed by Grooms, Debarro, and Paydarfar [12] (see Figure 3.2). The steps in the iterative procedure used questions to help optimize the design. If we answered no to any of these questions the design was modified and the process was begun again. The process consisted of six steps. The first step ensured that all subsystems would fit into the spacecraft. The second step used CAD software and finite element analysis to ensure acceptable structural and mass properties. The next steps determined if the manufacturing cost and schedule of the structure were acceptable. Cost–saving methods were implemented throughout the manufacturing procedure. These methods included manufacturing several components in on–campus facilities and using undergraduate and graduate student labor throughout the process. The final steps in the design process examined the assembly, manufacturing, and operations aspects of the design. Many steps were taken to ease handling, assembly, and manufacturing issues throughout the process. We used finite element analysis techniques, which we discuss in the next section, coupled with development considerations to arrive at the most efficient design. Upon successful completion of the design process, we arrived at the final HokieSat structural design. We now discuss in detail the final structural design configuration.

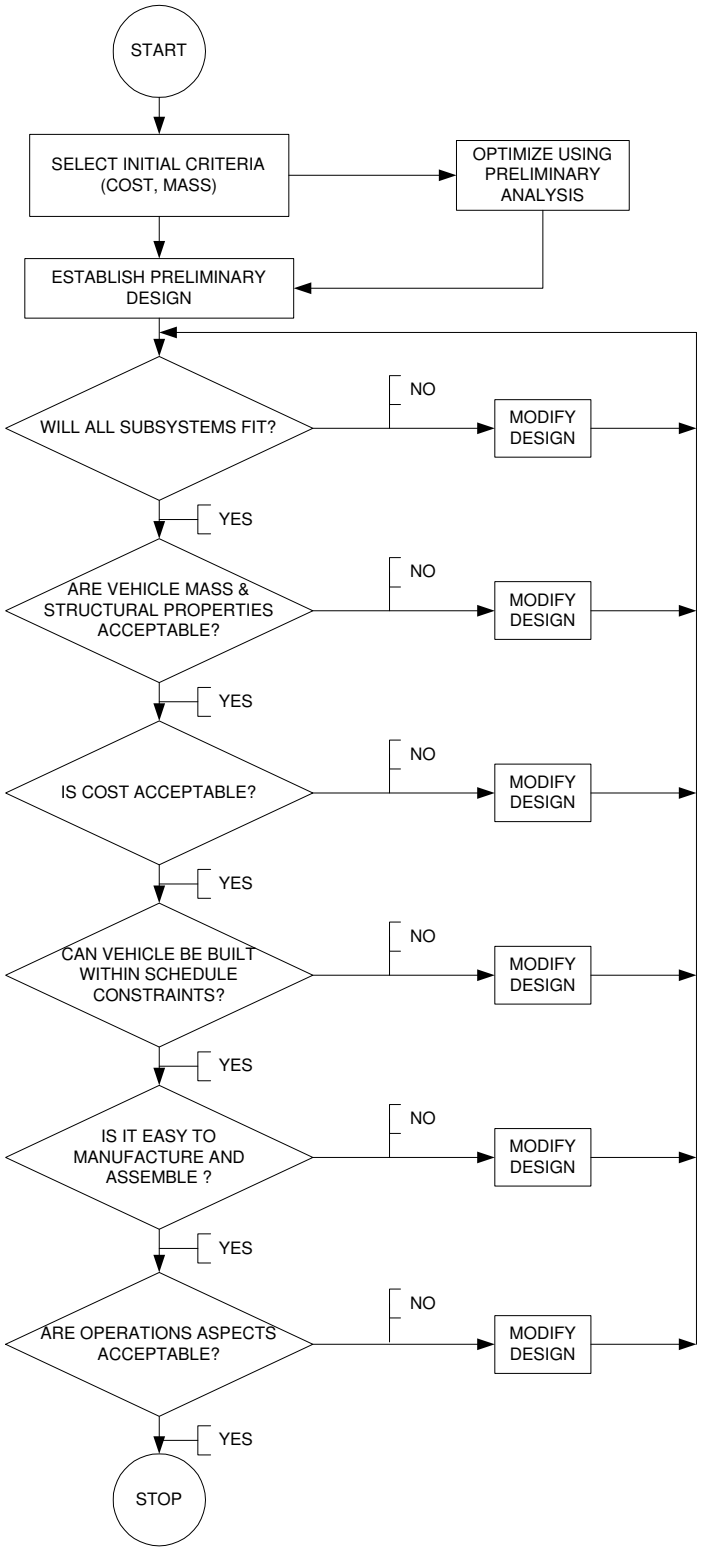

Figure 3.2: HokieSat Structural Design Process

3.2 Structural Configuration

The HokieSat structural configuration is designed to accommodate all of the mission components (see Figure 3.3 and Figure 3.4). The spacecraft uses body–mounted solar cells for power generation, torque coils for attitude control, digital cameras for attitude determination, micro–pulsed plasma thrusters for orbit control and several other components for data processing and communications. All of the electronics components connect to the isogrid at web intersection points, known as nodes. The isogrid pattern is configured with two–inch node spacing. This pattern allows for convenient mounting of the components while increasing the structural performance. The rib width dimension of 0.08 inch is minimized to eliminate mass and allow accurate machining without vibration [23, 36]. Minimizing the rib width dimension while maximizing the rib depth is also critical to preserve much of the panel bending stiffness.

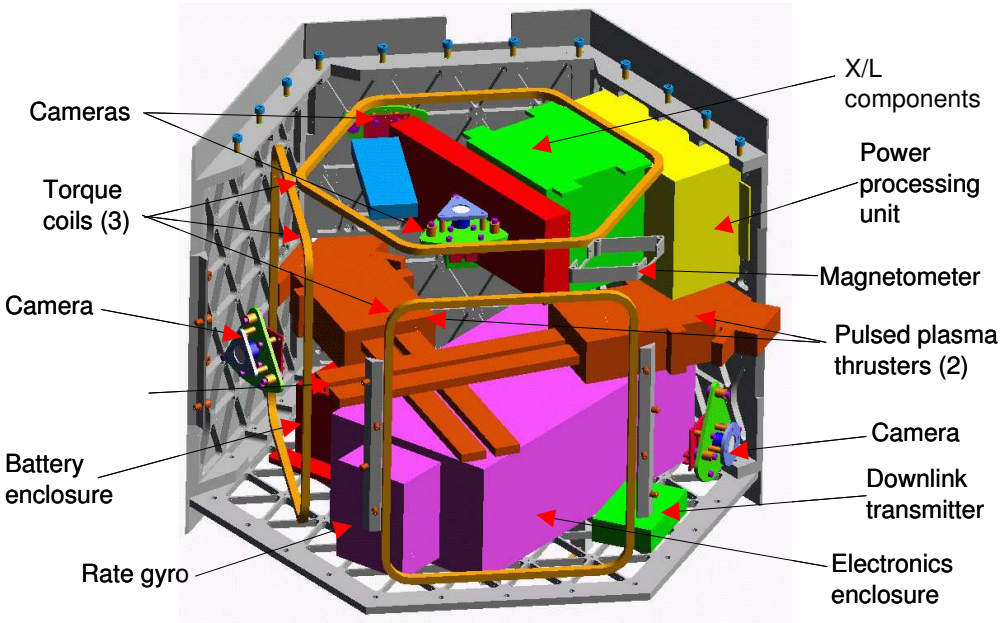

Figure 3.3: Internal Configuration of HokieSat

The separation system interfaces strongly govern the structural design. The separation systems chosen for our mission are the Lightband and the Starsys separation systems. HokieSat interfaces with the Starsys separation system on the nadir panel and the Lightband separation system on the zenith panel. The Lightband separation systems interconnect the ION–F spacecraft. The systems support the spacecraft during launch and separate at a specified time on orbit. The Lightband is configured as a hexagonal cylinder with a major diameter measuring 18 inches and a total height measuring 3 inches (see Figure 3.5). The system uses 24 #10–32 fasteners to connect to the host spacecraft. The Starsys separation system connects the ION–F stack to the MSDS. It uses the same bolt hole pattern; however the system uses steel to provide a stronger connection. It also has approximately the same footprint dimensions.

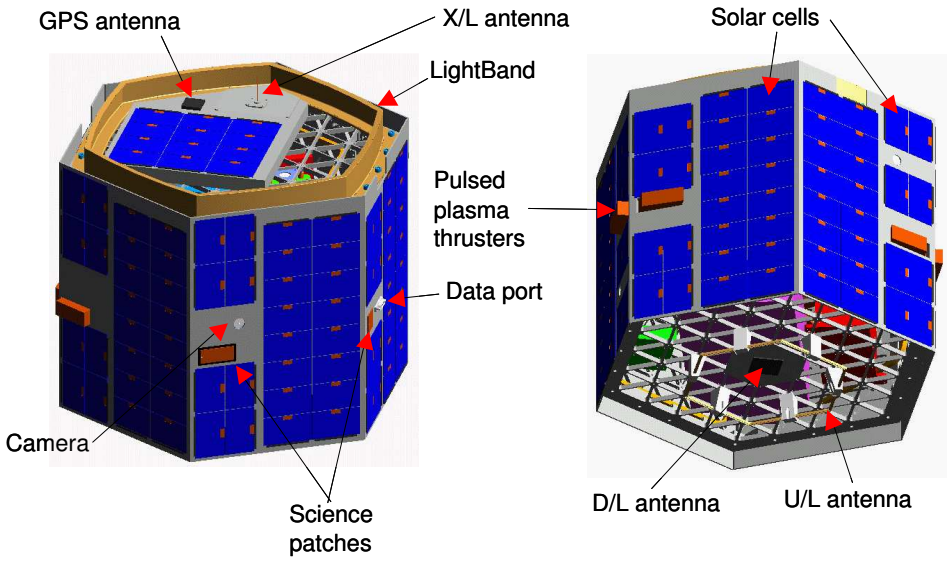

Figure 3.4: External Configuration of HokieSat

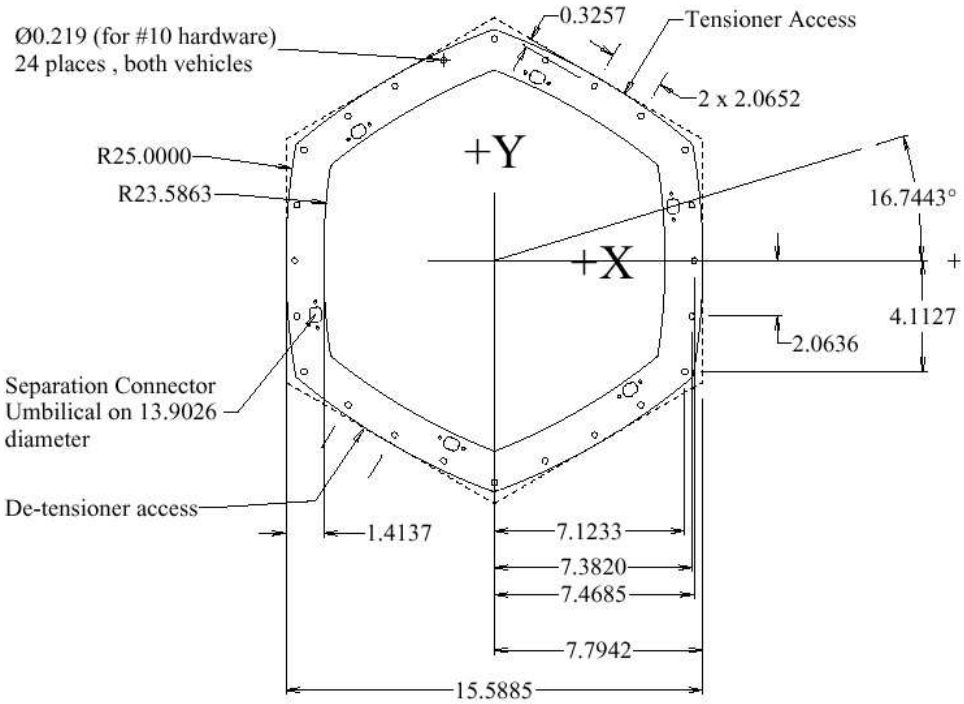

Figure 3.5: Lightband Footprint Bolt Pattern [15]

The structural assembly consists of eight isogrid plates (see Figure 3.6). The two end panels are hexagonal plates measuring 18 inches in major diameter and 0.25–inch in thickness. The panels use an open isogrid plate design with 24 #10–32 through holes defined by the Lightband separation system to connect to the side panel flanges. The side panels are manufactured using open 0.23–inch thick isogrid plates adhered to 0.02–inch outside skins. These composite side panels, shown in Figure 3.7, are less expensive to manufacture than a monocoque structure. The skins reinforce the side panels and provide a stiff, stable surface to affix body mounted solar cell arrays. The side panels are modified to extend one inch above and below the end panel surfaces to provide more area to support the cell arrays. The corner interfaces are designed using shear tabs to stiffen the joints and alleviate the shear loading on the bracket fasteners. Flanges protrude at the top and bottom of the panels to interface with the end panels and Lightband fasteners. The flanges are cut at a 60° angle along one edge to allow the corner Lightband fastener to connect efficiently. Modifications to the isogrid occur in four of the side panels to allow the nozzles of the pulsed plasma thruster (PPT) nozzles to protrude outside the structure. Two webs are cut out of the array to provide camera mounting for the attitude determination system. Based on previous analysis of isogrid structures, these modifications have a negligible effect on the structural integrity of the panels [36, 23].

Figure 3.6: End Panel Design

The structural assembly procedure requires that all of the side panels and internal components be assembled prior to attachment of the end panels. The side panels are assembled using two bracket designs. Bracket Design 1, shown in Figure 3.8, is the more robust bracket that is approximately 0.25–inch thick. The bracket is fabricated using Aluminum 6061–T651. The bracket design provides adequate shear and pull–out strength for the fasteners

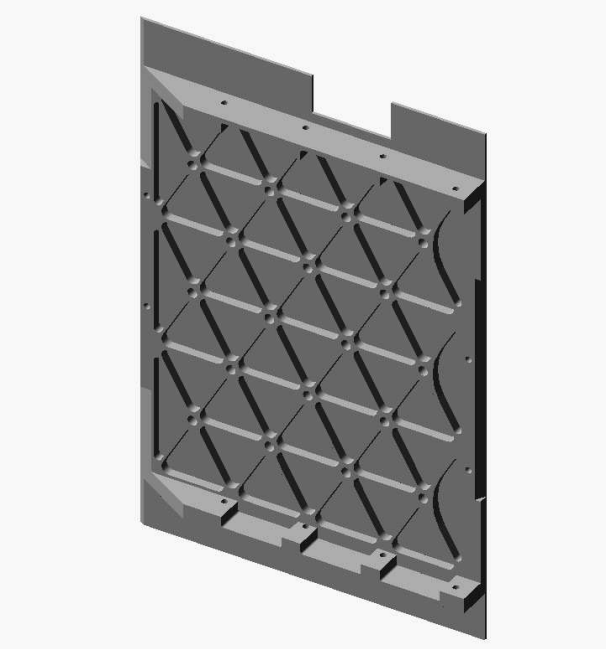

Figure 3.7: Composite Side Panel Design

and also reinforces the bending stiffness of the joint. Bracket Design 2, shown in Figure 3.9, is brake–formed using a 0.063–inch sheet of Aluminum 6061–T651. This design allows the PPTs and mounts to fit into the two corners. Both bracket designs connect the side panels using four #10–32 fasteners. The end panels and separation systems are attached to the flanges after all of the side panels and internal components are assembled, as shown in Figure 3.10. The Lightband separation system requirements specify that the system is to exhibit a flatness of less than 0.0005–inch per inch. The end panel is designed to accomodate this requirement. However, the final step of the assembly checks the Lightband flatness to ensure proper assembly of the system [15].

3.3 Summary

In this chapter we described the design process used to arrive at the existing HokieSat structural design. We presented the criteria and objective function used to select the optimum design. We also presented the panel designs and the final composite isogrid structural configuration. In Chapter 4, we discuss the manufacturing techniques used to fabricate the design and the quality assurance methods implemented to ensure hardware protection.

Figure 3.8: Side Panel Assembly (Bracket Design 1)

Figure 3.9: Side Panel Assembly (Bracket Design 2)

Figure 3.10: Structural Assembly

Chapter 4

Fabrication

The purpose of this chapter is to present the fabrication methods used to manufacture the HokieSat structure. We begin by describing the machining methods used to fabricate the structural assembly. We then describe the corrosion protection and quality assurance methods implemented to maintain integrity of the structure. We conclude with a description of the bonding process used to manufacture the composite side panels.

4.1 Structure Manufacturing

Manufacturing of the structure was completed using multiple machining methods to minimize cost. Several components were machined on a conventional mill in the on–campus Aerospace and Ocean Engineering (AOE) machining facility. These machines typically provide a tolerance of $\pm$ 0.001 inches. The panels were manufactured using an alternate method due to time, geometrical, and tolerance constraints.

The fabrication of the isogrid panels was performed using computer numerical controller (CNC) milling machines. The CNC milling machines use a computer interface to control the mill position. This interface enables parts to be fabricated with small tolerances. It also minimizes machine time by using a computer–aided–manufacturing (CAM) software to generate the mill control code, or "g-code," from computer–aided–drafting (CAD) software used to create design drawings. A CNC code was developed and implemented for all eight isogrid panels using AutoCAD and SolidWorks software. The side panels were machined from 1–inch blocks of aluminum to provide adequate thicknesses for the flanges. The end panels were machined from 0.25–inch sheets of aluminum.

All of the other components were manufactured using traditional means in the AOE machining facility. The skin face sheets were fabricated on a conventional mill from 0.02–inch sheets of aluminum. The brackets were machined and hand–formed from 0.25–inch and 0.125–inch aluminum sheets. All mechanical connections in the primary structural design were designed to use #10–32 standard fasteners.

Some structural components have special tolerance requirements. The zenith end panel outer surface is required to have no variations greater than 0.0005 inch per inch due to Lightband separation system reliability issues [15]. This was verified by using an indicator and a granite table as shown in Figure 4.1. The flatness must also be verified during the final assembly as variations may be introduced by errors in the torque margins of the fasteners.

Figure 4.1: Method Used to Verify Lightband Flatness Requirements

4.2 Composite Side Panel Bonding

The side panels were designed to be reinforced using a composite structure. Each side panel was adhered using a standard 2216 gray epoxy purchased through 3-M. The epoxy was chosen for its effectiveness at bonding aluminum and its durability in the arduous space environment [2]. It also exhibits relatively simple handling characteristics which enable the bonding to be used for small programs such as HokieSat.

A meticulous procedure was implemented to ensure a sufficient cure of the bond and satisfy all of the NASA safety criterion. The panels were first masked leaving only the bonding surfaces exposed to ensure that none of the other surfaces were contaminated with excess epoxy. The panels and instruments were then cleaned using seven 0.005–inch diameter monofilament lines were laid across the isogrid panel in the lateral direction (see Figure 4.2). The epoxy was mixed and then applied to the skin and the isogrid panels(see Figure 4.3). The panels and the skins were then wiped with a spatula to control the thickness of the bondline, as shown in Figure 4.4. The epoxy was less than 0.001–inch thick on the skin and the lines on the isogrid panels ensured that there was an even 0.005–inch distribution of epoxy over the entire surface. The skins were then placed on the isogrid panels and the assemblies were placed in fixtures to ensure a square lay–up, as shown in Figure 4.5. Finally, the panels were placed in an oven at approximately 80° Celsius for 120 minutes to cure [4].

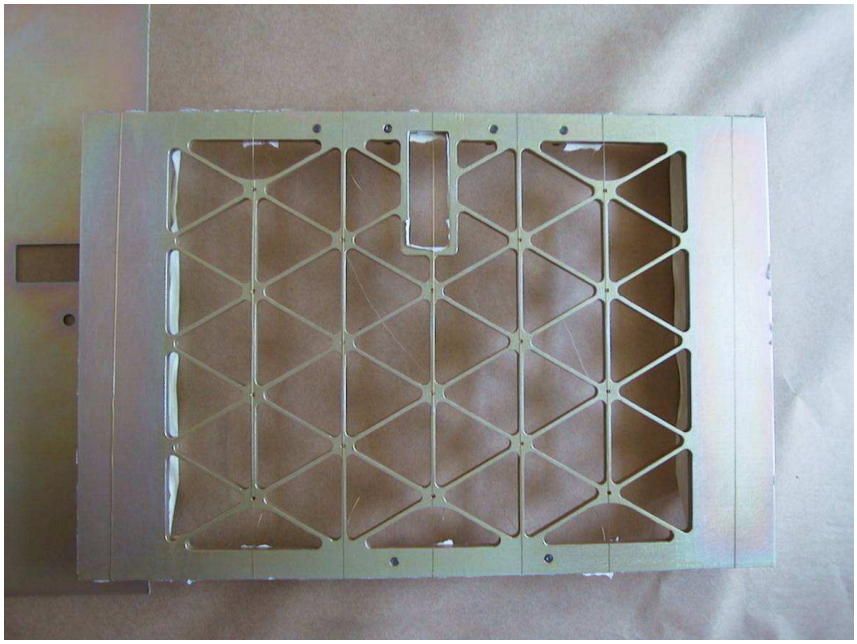

Figure 4.2: Isogrid Panel Surface Bonding Preparation

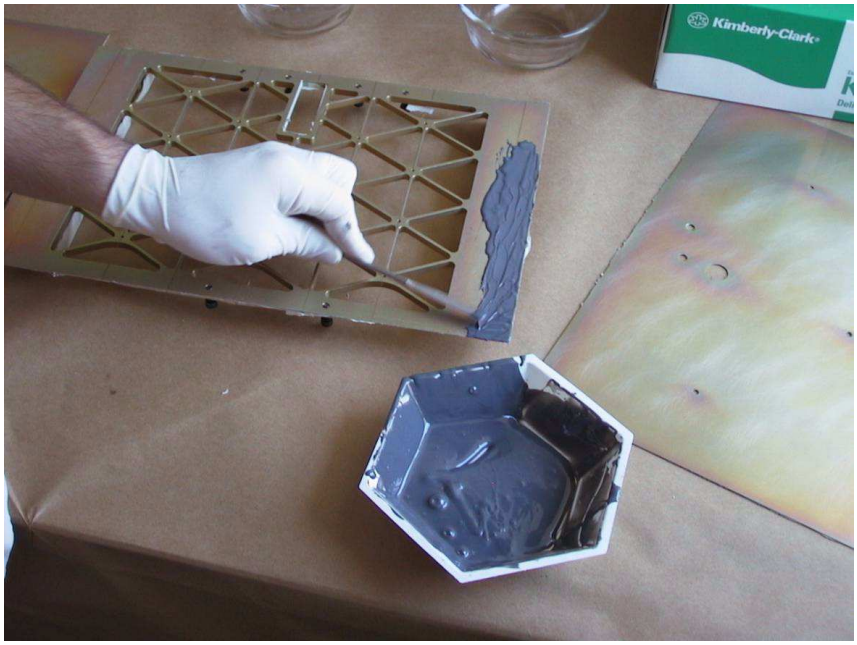

Figure 4.3: Application of the Epoxy to Isogrid Panel

Figure 4.4: Spatula Method Used to Ensure Even Epoxy Distribution

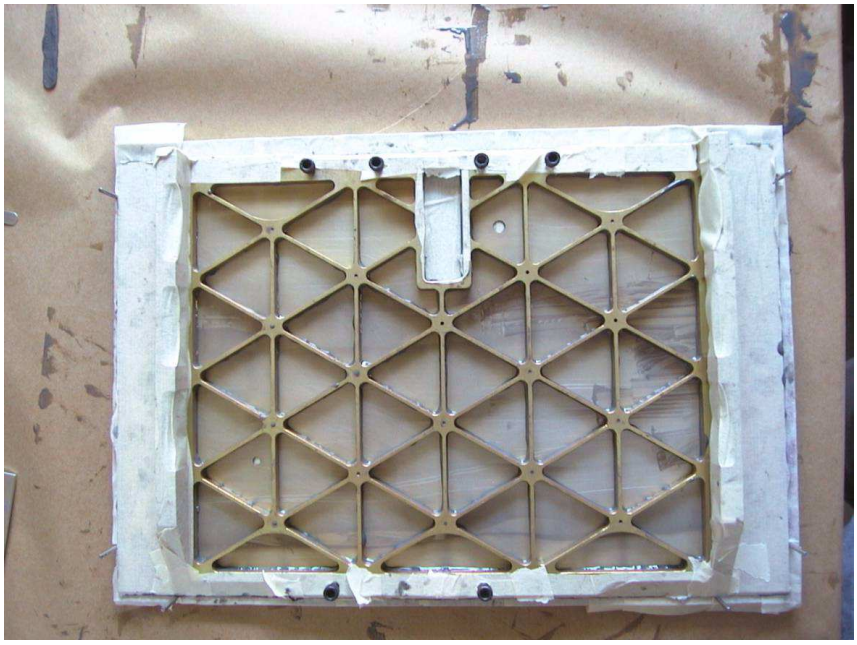

Figure 4.5: Method Used to Lay–Up the Composite Side Panels for Curing

4.3 Hardware Quality Assurance

All of the aluminum in the flight structure was coated with an iridescent chemical film for corrosion protection according to MIL-C-5541E [40]. The film protects the aluminum surfaces from oxidation without altering the dimensions. It also allows adequate thermal and electrical conductivity through the panels [1].

All of the hardware is stored in a Class 100,000 clean facility. Adequate clean room attire is required to handle the hardware to prevent contamination. The environment is maintained at temperatures between 65 and 75° Fahrenheit and humidities between 40 to 60%. These ideal conditions prevent oxidation of the aluminum and minimize the risk of damage to the electronic components (*e.g.* electrostatic discharge).

4.4 Summary

In this chapter we presented the manufacturing techniques used for fabrication. We also discussed the bonding procedure used to lay–up the composite side panels. We concluded by presenting the current methods used to assure quality of the hardware. We now discuss the analysis and test techniques used to verify the integrity of the structure.

Chapter 5

Structural Verification

In this chapter, we describe the methods used to verify the integrity of the HokieSat structure. We begin with the preliminary static analysis that guided the nanosatellite mechanical design. We then refine the analysis using correlation of the finite element model with static and modal testing. Finally, we present the results of a detailed ION–F finite element analysis to ensure survivability of the stack configuration during launch.

5.1 Preliminary Analysis

We began the structural analysis by performing a simplified analysis on the satellite to size the preliminary design of the structure. We used an iterative procedure as shown in Chapter 3 and performed finite element analyses of the structure using the launch environment loading conditions. Basic isogrid theory was then applied to establish criteria for choosing the initial isogrid structural design.

The loading conditions were computed using requirements from the SHELS User's Guide [26] (SUG). The limit load factors are shown in Table 5.1. These load factors were considered simultaneously and in all possible permutations. We also applied factors of safety, *FS*, to the limit load factors equal to 1.25 on yield and 1.4 on all ultimate failures (see Table 5.2). The margins of safety, *MS*, were calculated using the following formula:

$$MS = \frac{\sigma_{allowable}}{FS \times \sigma_{actual}} - 1 \geq 0 \tag{5.1}$$

where $\sigma_{allowable}$ is either the allowable yield stress or the allowable failure stress for the material (depending on the factor of safety), and σ_{actual} is the stress calculated in the analysis. The margins must be positive for all failure modes, including material failure and buckling.

The structure was first modeled using arrays of shell elements. The preliminary dimensions of the structure were defined as a hexagonal prismatic shell with a height measuring 11.5 inches and a major diameter measuring 18 inches. We performed a stress analysis on

Table 5.1: SHELS Structural Design Limit Load Factors

LX (g)	LY (g)	LZ (g)
±11.0	±11.0	±11.0

Table 5.2: SHELS Structural Design Factors of Safety

FS_{yield}	$FS_{ultimate}$
1.25	1.4

the structure for different shell element thicknesses. We then found the equivalent isogrid panel stresses using theory described in the Isogrid Design Handbook [23]. The handbook derives the stress equations based on the isogrid geometrical parameters. The parameters defining isogrid geometry are shown in Figure 5.1 and presented in Table 5.3.

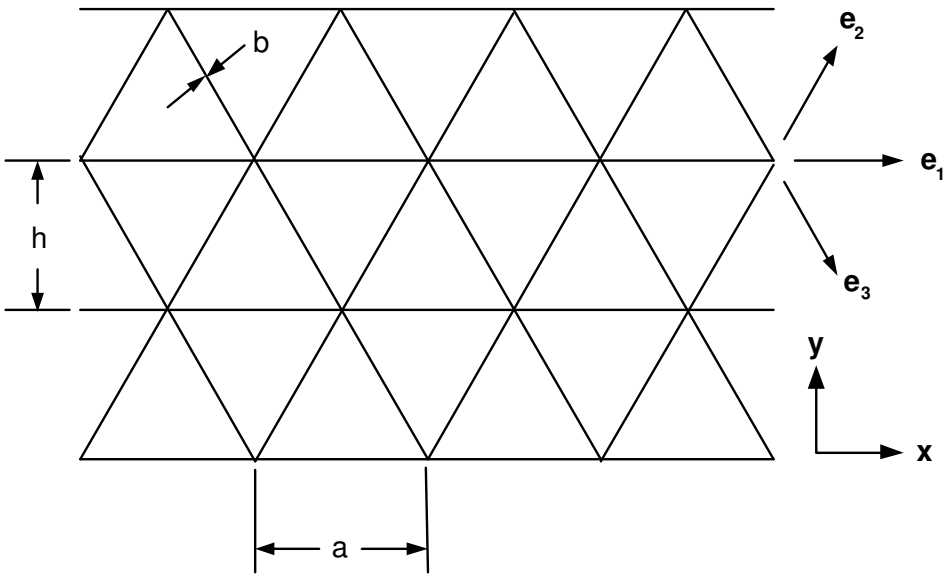

Figure 5.1: Isogrid Parameters

We first explain the isogrid theory and assumptions to present the method used for the preliminary analysis. We begin by examining a web element of the gridwork and assuming it is in a state of uniaxial stress. Only one of the principal stresses in each member is assumed to be nonzero, therefore, the uniaxial bar strains, e_1, e_2, and e_3, are defined as the longitudinal strains of the webs in the three corresponding directions. Applying the strain transformation law yields the following relationship between the uniaxial bar strains and the

Table 5.3: Isogrid Definitions

Parameter	Definition
t	Thickness of Skin
b	Width of Rib Web
h	Height of Triangle
a	Distance Between Node Centers
d	Depth of Web
$\overline{E}$	Equivalent Young's Modulus

grid coordinate strains:

$$\begin{pmatrix} e_x \\ \gamma_{xy} \\ e_y \end{pmatrix} = \frac{1}{3}\begin{bmatrix} 3 & 0 & 0 \\ 0 & 2\sqrt{3} & -2\sqrt{3} \\ -1 & 2 & 2 \end{bmatrix}\begin{pmatrix} e_1 \\ e_2 \\ e_3 \end{pmatrix} \tag{5.2}$$

The uniaxial bar loads for a unit thickness, P_i, are defined by recalling the generalized form of Hooke's law:

$$P_i = bEe_i \qquad i = 1, 2, 3 \tag{5.3}$$

We now seek to develop Hooke's law for the entire membrane. For a first approximation, the changes in curvature and the corresponding bending stresses are neglected. Poisson's ratio is also assumed to be $\frac{1}{3}$. The membrane stress resultants, N_x, N_{xy}, and N_y, may thus be found using plane stress solutions or equilibrium conditions. The relationships between the stress resultants and the grid strains are as follows:

$$\begin{pmatrix} N_x \\ N_{xy} \\ N_y \end{pmatrix} = K\begin{bmatrix} 1 & 0 & \frac{1}{3} \\ 0 & \frac{1}{3} & 0 \\ \frac{1}{3} & 0 & 1 \end{bmatrix}\begin{pmatrix} e_x \\ \gamma_{xy} \\ e_y \end{pmatrix} \tag{5.4}$$

where the extensional stiffness, K, is equal to the following:

$$K = \frac{9}{8}Et(1+\alpha) \tag{5.5}$$

The nondimensional parameter α is computed using the following relationship:

$$\alpha = \frac{bd}{th} \tag{5.6}$$

Solving Equation 5.4 for the grid strains as functions of the stress resultants yields:

$$\begin{pmatrix} e_x \\ e_y \end{pmatrix} = \frac{1}{Et(1+\alpha)}\begin{bmatrix} 1 & -\frac{1}{3} \\ -\frac{1}{3} & 1 \end{bmatrix}\begin{pmatrix} N_x \\ N_y \end{pmatrix} \tag{5.7}$$

$$\gamma_{xy} = \frac{8}{3}\frac{N_{xy}}{Et(1+\alpha)} \tag{5.8}$$

We now find the skin stress equations using the derived relations. The skin stresses are found using Hooke's Law and substituting in the above equations. The generalized form of Hooke's law for planar stress problems is given in the following equation:

$$\begin{pmatrix} \sigma_x \\ \sigma_y \end{pmatrix} = \frac{E}{1-\nu^2} \begin{bmatrix} 1 & \frac{1}{3} \\ \frac{1}{3} & 1 \end{bmatrix} \begin{pmatrix} e_x \\ e_y \end{pmatrix} \tag{5.9}$$

$$\tau_{xy} = \frac{E}{2(1+\nu)} \gamma_{xy} \tag{5.10}$$

The skin stresses are therefore found by substituting Equations 5.7 and 5.8 into Equations 5.9 and 5.10:

$$\begin{pmatrix} \sigma_x \\ \tau_{xy} \\ \sigma_y \end{pmatrix} = \frac{1}{t(1+\alpha)} \begin{pmatrix} N_x \\ N_{xy} \\ N_y \end{pmatrix} \tag{5.11}$$

We now find the rib stress equations using the above derivations. The rib stresses are the normal stresses calculated along the three rib directions. Therefore, the rib stresses are found from Equations 5.2 and 5.3 as:

$$\begin{aligned} \sigma_1 &= \frac{P_1}{b} = E e_x \\ \sigma_2 &= \frac{P_2}{b} = \frac{E}{4}(e_x + \sqrt{3}\gamma_{xy} + 3e_y) \\ \sigma_3 &= \frac{P_3}{b} = \frac{E}{4}(e_x - \sqrt{3}\gamma_{xy} + 3e_y) \end{aligned} \tag{5.12}$$

We formulate the rib stress equations by substituting in Equations 5.7 and 5.8 into Equation 5.12 to obtain:

$$\begin{aligned} \sigma_1 &= \frac{1}{3t(1+\alpha)}(3N_x - N_y) \\ \sigma_2 &= \frac{2}{3t(1+\alpha)}(N_y + \sqrt{3}N_{xy}) \\ \sigma_3 &= \frac{2}{3t(1+\alpha)}(N_y - \sqrt{3}N_{xy}) \end{aligned} \tag{5.13}$$

We next choose the skin thickness, t, to be zero to simplify the analysis and create a worst case loading condition. We substitute Equation 5.6 into Equation 5.13 and establish the zero skin–thickness condition to obtain:

$$\begin{aligned} \sigma_1 &= \frac{h}{3bd}(3N_x - N_y) \\ \sigma_2 &= \frac{2h}{3bd}(N_y + \sqrt{3}N_{xy}) \\ \sigma_3 &= \frac{2h}{3bd}(N_y - \sqrt{3}N_{xy}) \end{aligned} \tag{5.14}$$

Due to the isotropic nature of isogrid it is possible to relate the extensional stiffness parameters and rib stress equations to a monocoque plate. In this case, the open isogrid is modeled as a solid plate of equal thickness and reduced stiffness. We model the reduced stiffness by using an equivalent Young's modulus, $\overline{E}$, that is based on the stiffness reduction due to the grid geometry. This formulation reduces to the following:

$$\overline{E} = E\frac{b}{h} \tag{5.15}$$

where the E is Young's modulus of the isogrid material. Thus, it is possible to create a monocoque plate that represents the equivalent isogrid panel.

We created a finite element model in I-DEAS [38] using a linear shell element array (see Figure 5.2). We first simplified the analysis by minimizing the number of parameters. The width of the rib, b, and the distance between node centers, a, were previously chosen based on machining and integration constraints as discussed in Chapter 3. These constants therefore make the equivalent Young's modulus constant. The web depth (panel thickness), d, is the only other independent parameter and is equal to the monocoque panel thickness in this case. We performed an iterative analysis by calculating the rib stresses at different web depths. The results are shown in Table 5.4. The values of the yield and ultimate stresses of Aluminum 6061-T651 are 35 kips per square inch (ksi) and 38 ksi, respectively [39]. The margins were calculated using Equation 5.1 and the factors of safety shown in Table 5.2. The preliminary results show that 0.200–inch thick plates are sufficient. However, we were forced to increase the panel thickness for the following reasons:

- meeting the stiffness requirements of the entire payload assembly (ION–F and MSDS) [2]
- surviving the conservative testing requirements (discussed later in the chapter)
- neglecting the component masses and assuming an simplified load path
- threading the component fasteners into the isogrid panels
- increasing the stack mass

The ION–F stack stiffness was a major concern in the design. HokieSat is a major contributor to the overall stack stiffness due to its position at the base of the stack. A preliminary stack modal analysis was performed and the results demonstrated that 0.200–inch plates were insufficient. We were also concerned about incorrect load paths in the model and failure to model non–structural mass (components). Providing sufficient thread length for fasteners for component integration was also another concern. Finally, satisfaction of the conservative test requirements, which will be explained later in this chapter, and a substantial stack mass increase further required an increase in panel thickness. Therefore, we increased the plate thickness to 0.250–inch to accommodate all of the requirements.

In the next section, we refine the analysis to model the actual isogrid webs. We present the modal analysis and testing used to verify the model. We discuss the analysis and test correlation of the isogrid end panel, isogrid side panel, and isogrid assembly models.

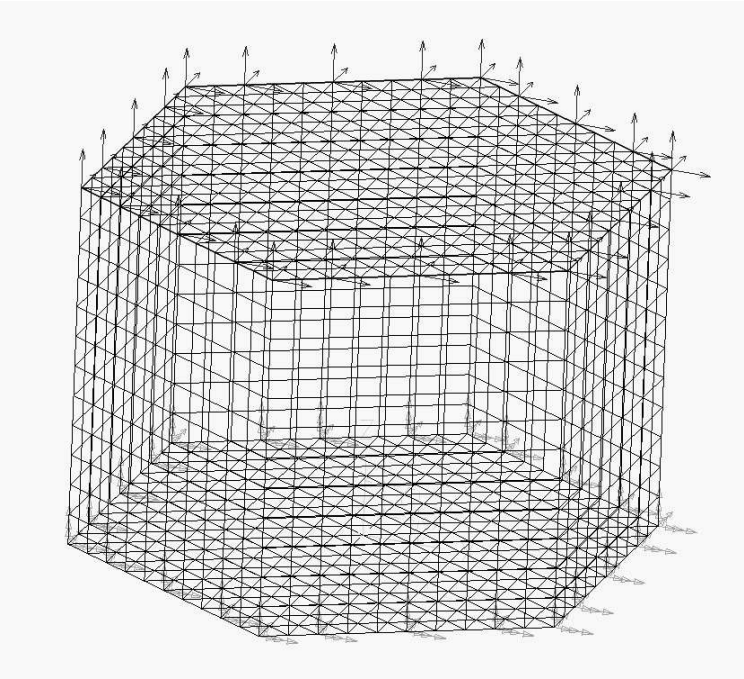

Figure 5.2: Preliminary Analysis Mesh Configuration

Table 5.4: Preliminary Analysis Results

d (inch)	σ_{max} (ksi)	MS_{min}
0.063	74.2	-0.663
0.125	36.0	-0.306
0.150	30.2	-0.173
0.175	25.6	-0.025
0.200	22.2	0.124
0.225	19.6	0.274
0.250	17.8	0.407

5.2 Isogrid Satellite Model

We next refined the model and created a finite element model of the physical isogrid structure. We modeled the isogrid panels using arrays of beam and shell elements. We began by creating models of the isogrid side and end panels. We then assembled the panels into the isogrid structural assembly. We verified the model in several steps throughout the process using modal analysis and testing correlation.

We first modeled an isogrid end panel using an array of 0.25–inch thick beam and shell elements. The isogrid webs were modeled as several 2–inch discrete beam elements, as shown in Figure 5.3. The edge stiffener, or separation system mounting area, is modeled using 0.25–inch thick linear quadrilateral and triangular shell elements. The separation system mounting points were modeled as nodes which created a nonuniform element geometry.

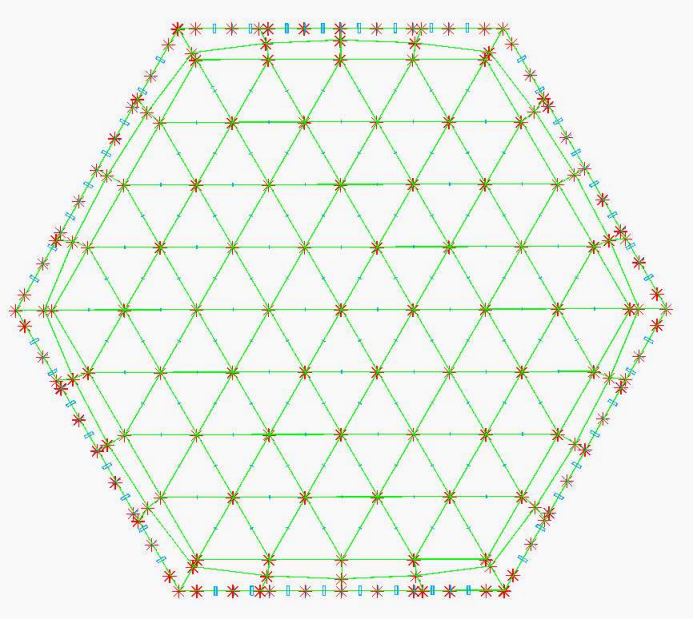

Figure 5.3: Isogrid End Panel FEM

We next performed a modal analysis to investigate the unrestrained stiffness properties of the end panel. We used the Lanczos solver in I-DEAS to calculate the first 2 resonances of the panel. The solver incorporates frequency shifting for efficient solving of the normal modes. The first two modes are shown in Figures 5.4 and 5.5. The first mode exhibits a twisting/bending mode shape (hyperbolic parabaloid) at a natural frequency of 105 Hz. The second mode is a "drum" mode occurring at 182 Hz. A "drum" mode occurs when the center of the panel vibrates similar to a drum head.

We modeled an isogrid side panel using an array of beam and shell elements. The side

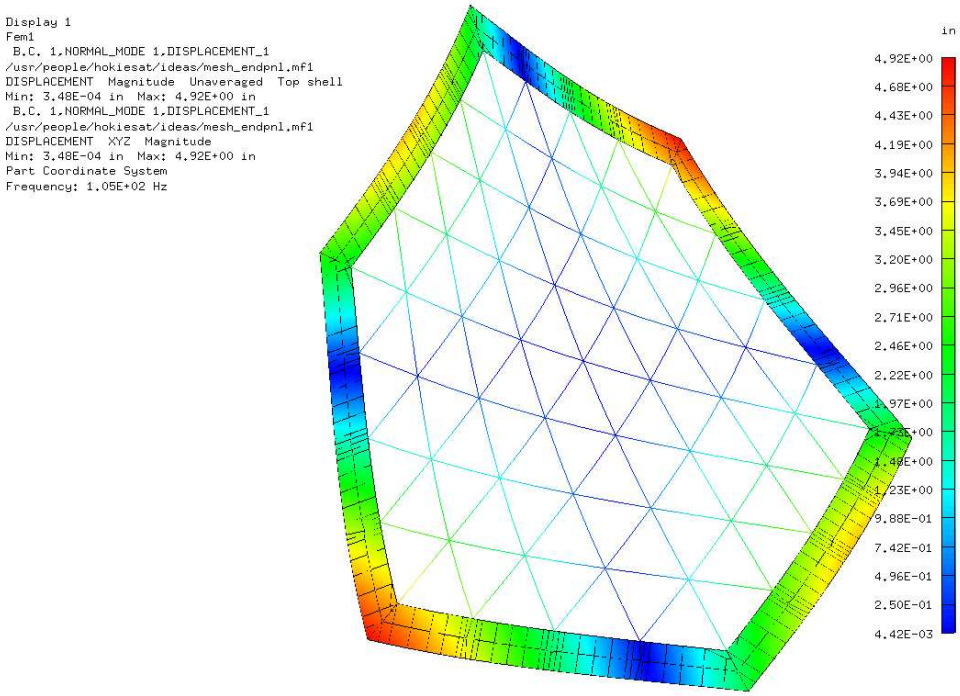

Figure 5.4: Isogrid End Panel FEM First Mode

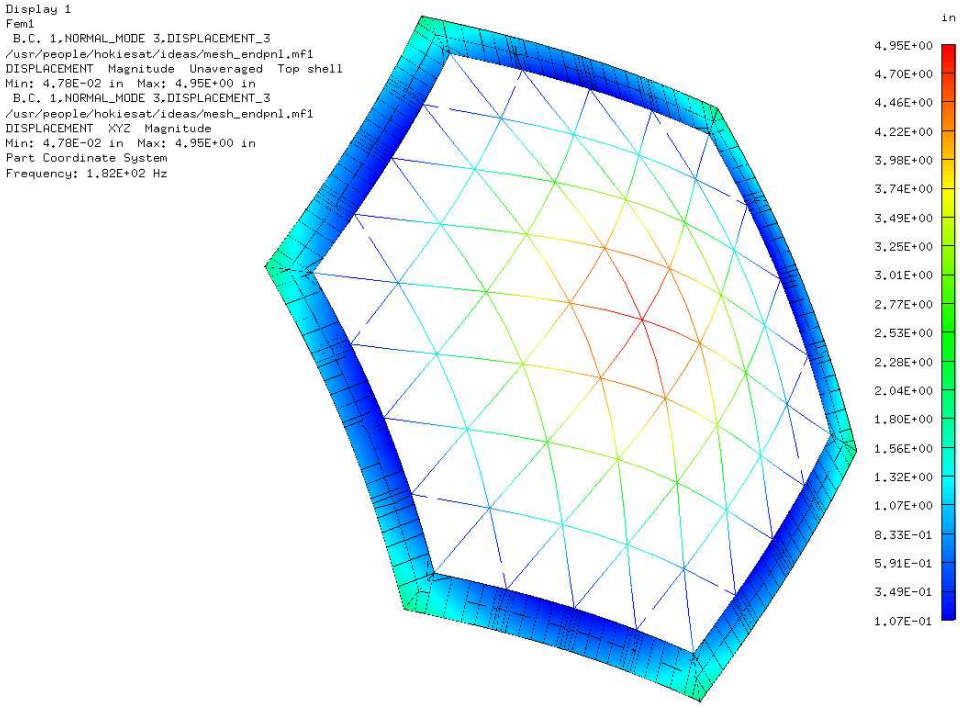

Figure 5.5: Isogrid End Panel FEM Second Mode

panel was modeled similar to the end panel model; however, we included the flanges and overhangs. The stiffeners were modeled using 0.23–inch thick linear quadrilateral shell elements. The webs were modeled using 0.23–inch thick linear beam elements. We represented the flanges and overhangs using solid and shell elements, respectively. The elements were offset from the neutral–axis nodes of the webs and stiffeners to create the proper stiffness properties of the panel. Rigid elements were used to connect the element nodes and transfer the loads [9] between the elements.

We also performed a modal analysis on the side panel to examine the unrestrained stiffness properties. The first two modes are shown in Figures 5.6 and 5.7. The unrestrained model exhibits a fundamental torsional mode of vibration at 131 Hz. The top and the bottom of the panel vibrate 180° out of phase. The second mode of vibration is a plate bending mode shape occurring at 171 Hz. The plate bends about its minor axis.

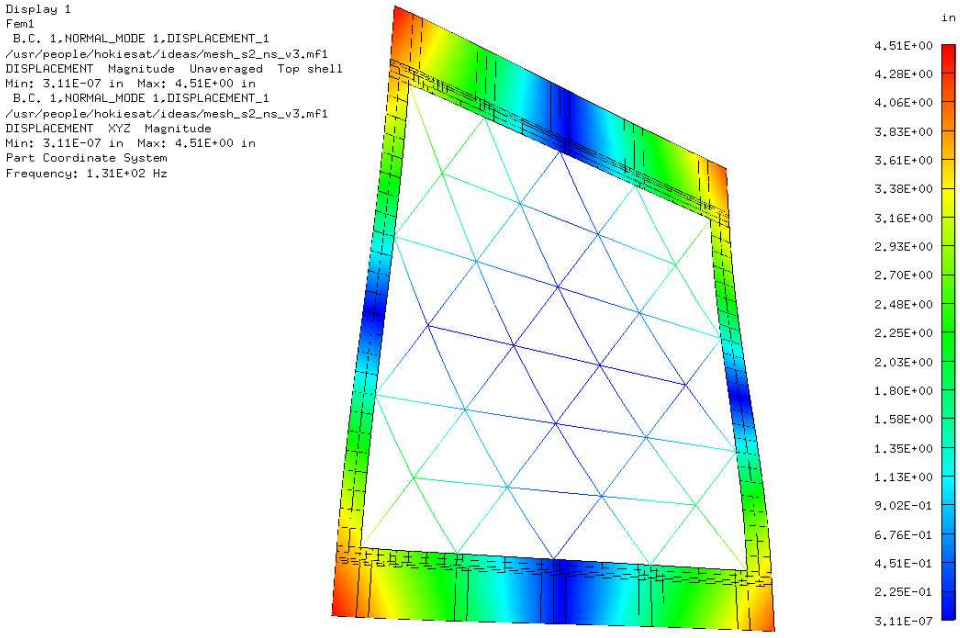

Figure 5.6: Isogrid Side Panel FEM First Mode

We next verified the accuracy of the models using modal experiment data correlation. We performed a tap test using a tap hammer and piezoelectric accelerometers. The experiment was conducted at Virginia Tech in the Mechanical Engineering Modal Analysis Laboratory and the Aerospace and Ocean Engineering Structures Laboratory. The panels were supported using tape and bungee cord configurations, as shown in Figure 5.8. All instruments were calibrated according to MIL–STD–45662A. The panel was struck with the tap hammer which measures the impulse. The accelerometers measured the response and the signals were processed using a Fourier analyzer system. The frequency response function (FRF) was calculated using a fast Fourier transform algorithm and the resonances and phases were examined. The results for the panels are shown in Figures 5.9, 5.10, and 5.11. The end panel

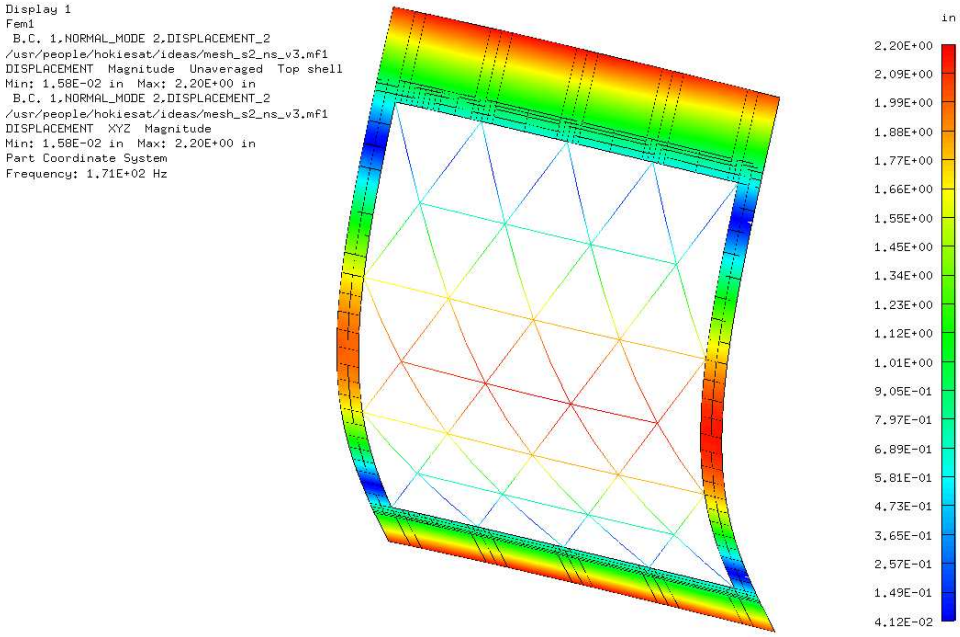

Figure 5.7: Isogrid Side Panel FEM Second Mode

and side panel mode shapes correlate well with the analysis. The side panel analytical natural frequencies are within 1% of the experimental data. However, the frequencies of the end panel analytical modes are approximately 6% below the experimental natural frequencies. This error is most likely due to deficiencies in inertial properties modeling and stiffness modeling (fillets) and is considered acceptable. We consider both finite element models verified within acceptable margins.

We next configured the FEM panels into the isogrid structural assembly. The panels were connected using coincident edge nodes that transfer the loads between the corner shell elements. We did not model the flanges and the overhangs to reduce complexity and because the overhangs have relatively little contribution to the structural integrity of the assembly. We first performed a modal analysis to examine the stiffness properties of the model. The results are shown in Figures 5.12 and 5.13. The first mode of the assembly has a natural frequency of 249 Hz. At this frequency, the mode shape exhibits large deflections of the end panels (also called a "drum mode") that resonate 180° out of phase. The second mode of the structure occurs at 263 Hz. The second mode shape is also a "drum mode;" however, the nadir panel vibrates in phase with the zenith panel. The analysis demonstrates that components mounted on the center of these panels will experience the greatest accelerations during launch.

Figure 5.8: End Panel Modal Test Configuration

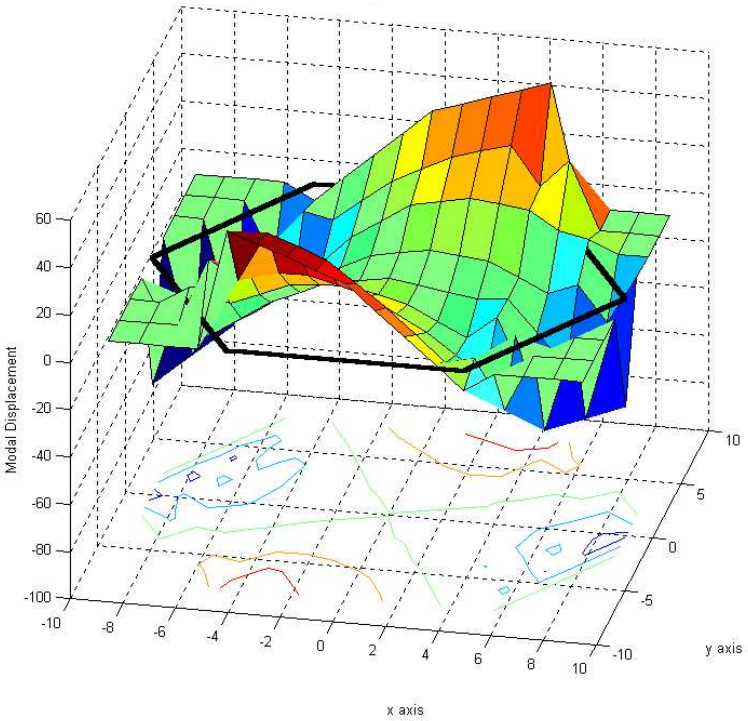

Figure 5.9: Isogrid End Panel Modal Testing Results (f_n = 111 Hz)

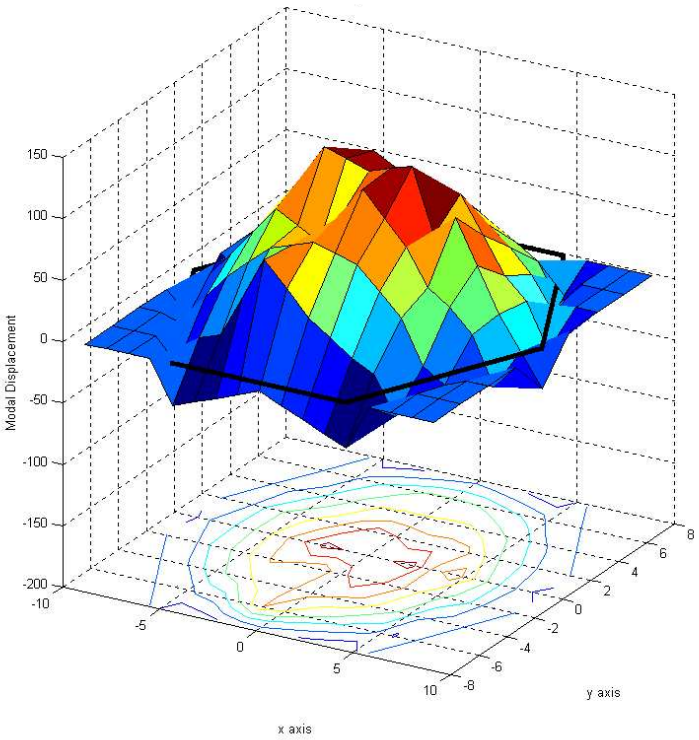

Figure 5.10: Isogrid End Panel Modal Testing Results (f_n = 193 Hz)

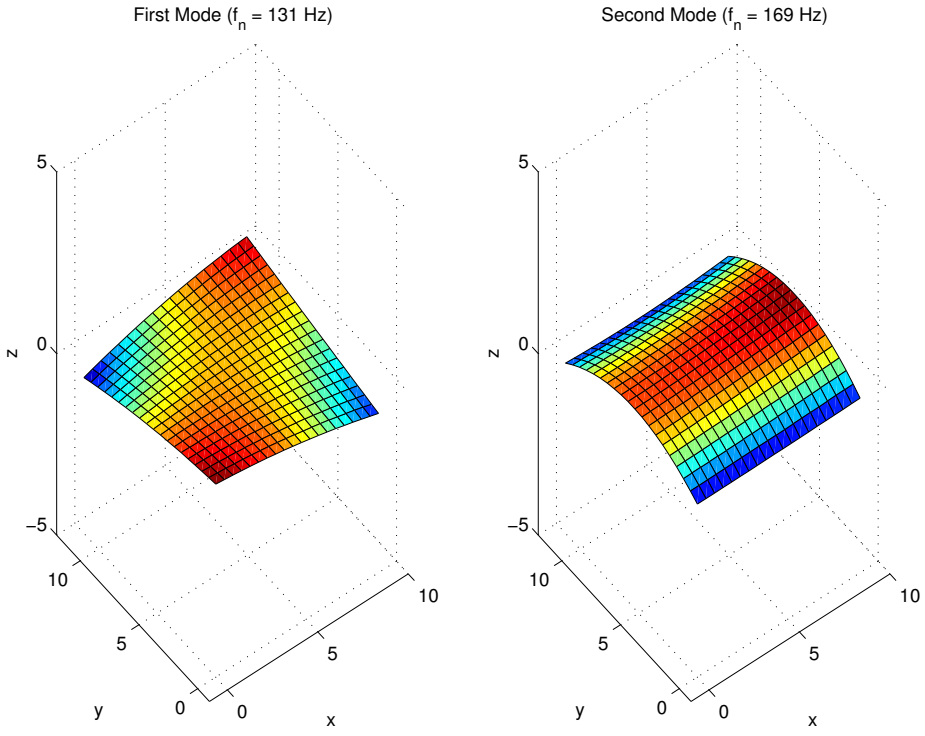

Figure 5.11: Isogrid Side Panel Modal Testing Results

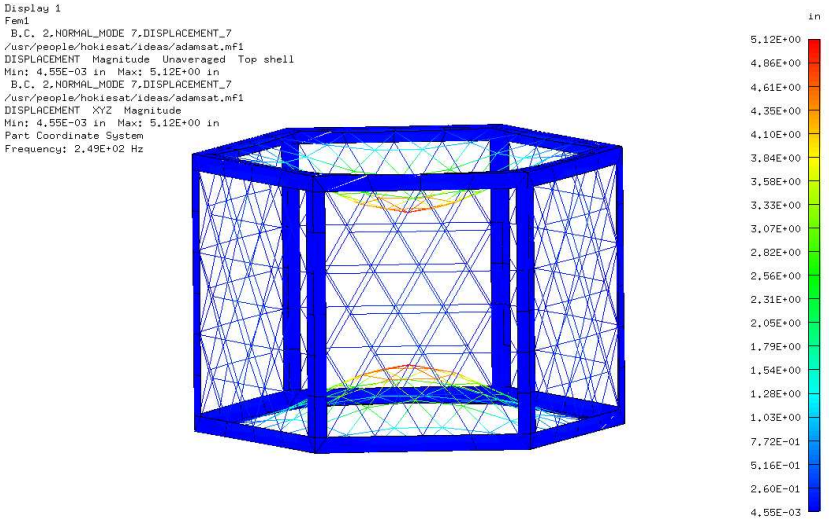

Figure 5.12: Isogrid Assembly FEM First Mode

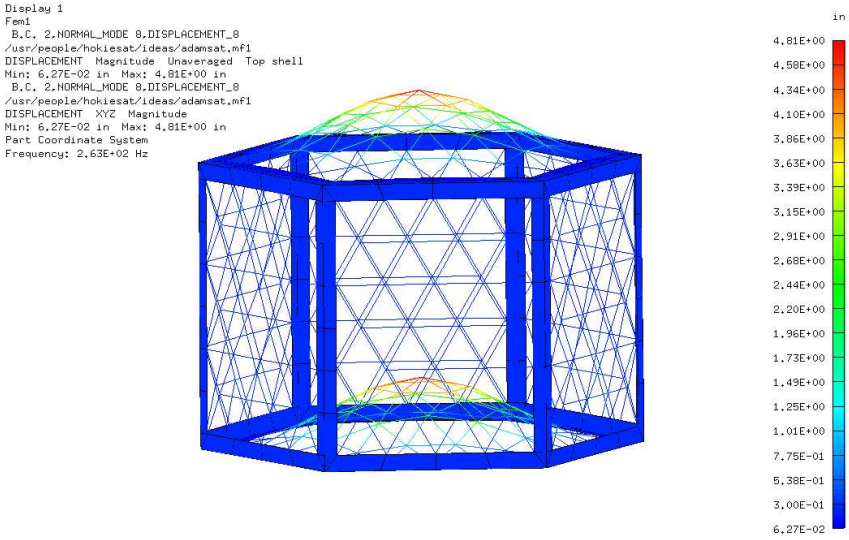

Figure 5.13: Isogrid Assembly FEM Second Mode

A modal survey was also conducted on the isogrid structure to evaluate the correlation between the analytical and experimental data. The structure was tethered from a crane with elastic cords to provide unrestrained boundary conditions. A 75 pound shaker with a four-inch vertical stinger was used to apply a burst chirp impulse to the structure ranging from 20 Hz to 1000 Hz. A three-axis accelerometer was attached at different locations on the spacecraft for each test. A statistical analysis was performed on the results and the mean values for the first and second modal natural frequencies are shown in Table 5.5. A comparison demonstrates that the first and second mode shapes are similar and the first mode analytical natural frequency deviates approximately 1% from the mean experimental result. These results demonstrated that the isogrid assembly model was a sufficient model of the spacecraft isogrid structure.

Table 5.5: Modal Survey Test Data

Mode	Analysis (Hz)	Experiment (Hz)
1	249	246
2	263	272

5.3 Composite Satellite Model

We next refined the isogrid model further to incorporate the epoxied skin side panel (composite) construction. We began the analysis by modifying the isogrid side panel model described above. We created 0.020–inch thick shell elements offset from the web and flange neutral–axis nodes (see Figure 5.14). We modeled the skin using linear quadrilateral and triangular shell elements to efficiently fit the geometry. The nodes of the skin elements were connected to the web and flange elements using rigid elements, as described in the previous section [9, 16].

We also conducted a modal analysis in I-DEAS to determine the structural properties of the composite structure. Figures 5.15 and 5.16 show that the mode shapes are similar to the isogrid panel modes. However, the corresponding first mode natural frequency increases to 159 Hz and the second mode natural frequency increases to 219 Hz. The analysis results therefore demonstrates a gain in structural stiffness of approximately 21% by adding the skins.

We once again verified the model using modal experimentation. The side panels were tested using two configurations. The panels were again hung vertically using tape as described above (see Figure 5.17), and hung horizontally using a bungee cord configuration. The accelerometer was placed at several locations on the panel and the tap hammer was used to induce an impulse. The frequency response functions (FRFs) were examined resulting in the modes depicted in Figure 5.18. The mode shapes were also verified by finding the Chladni patterns [29] of the panel. A five–pound shaker was connected to the panel in the

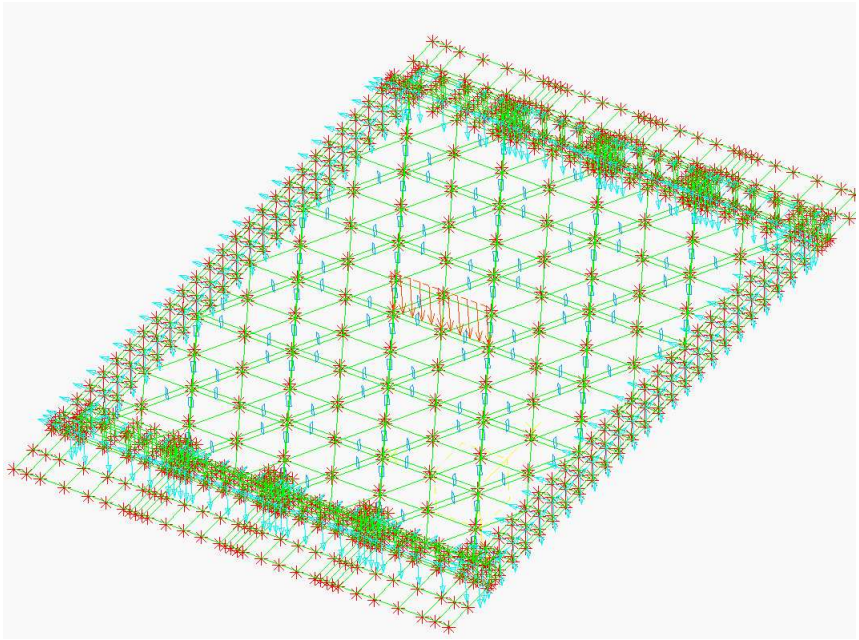

Figure 5.14: Composite Side Panel Mesh

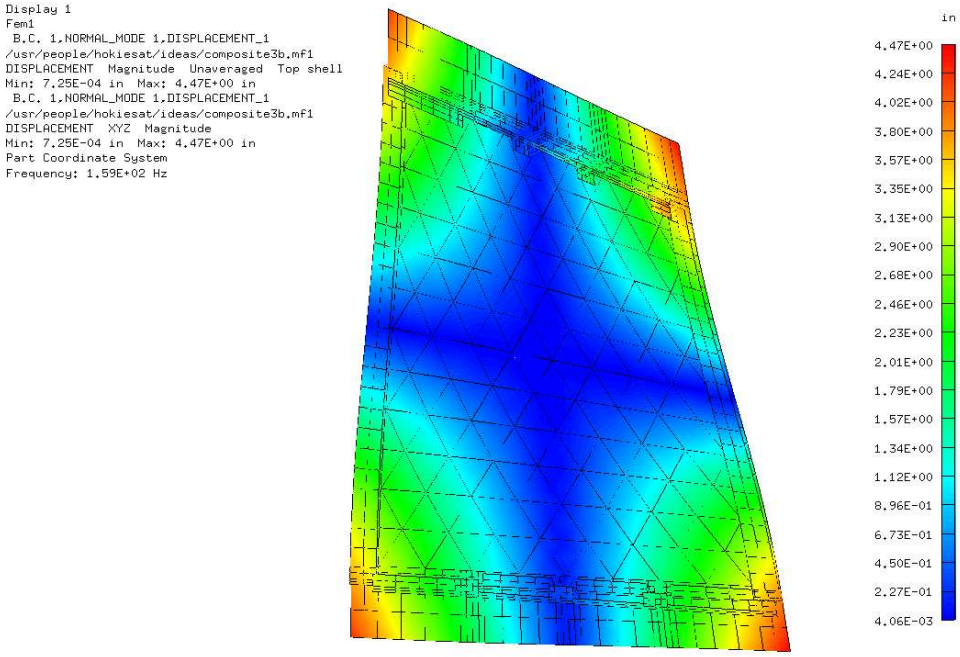

Figure 5.15: Composite Side Panel FEM First Mode (f_n = 159 Hz)

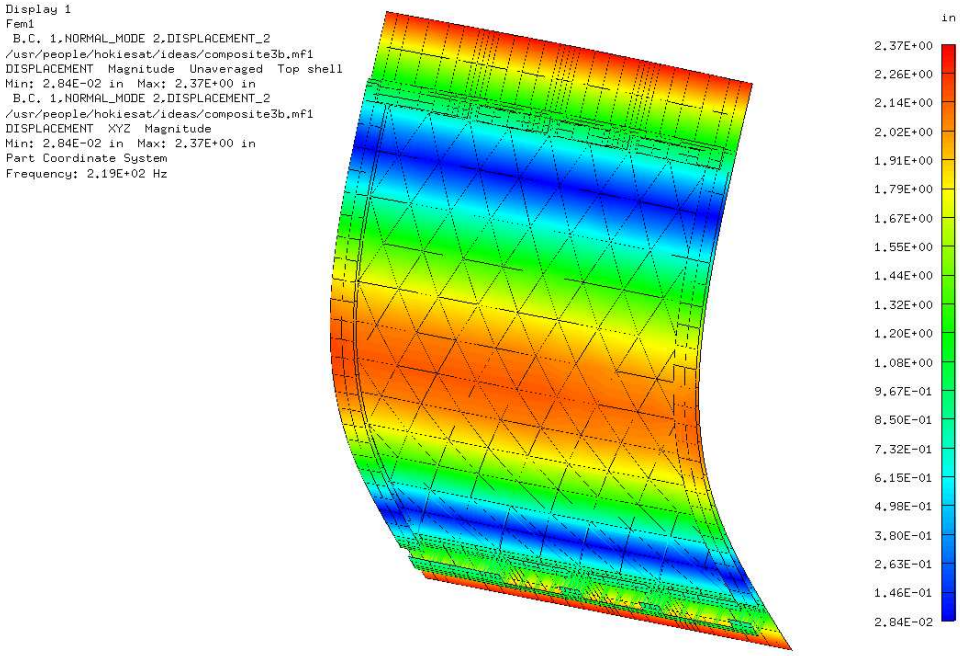

Figure 5.16: Composite Side Panel FEM Second Mode (f_n = 219 Hz)

horizontal configuration using a #10–32 vertical stinger which allowed efficient connection to existing threaded holes. Sand was then evenly dispersed over the top of the panel. A signal generator was used to create sine wave signals at the first two resonant frequencies. Each signal was amplified and used as input to the shaker. As the panel resonated at its respective natural frequency, the sand migrated from the excited regions of the panel to the regions of least response, known as nodal regions. The results, shown in Figures 5.19 and 5.20, show excellent correlation with the nodal regions computed in the analysis. The modal experiments demonstrate that the first 2 mode shapes and frequencies correlate with the analysis to within 1% error. We therefore considered the FEM an accurate model of the composite side panels.

We next performed static testing on the composite panels to mitigate concerns with the epoxy procedure. We constructed a modified plate bending test to evaluate the peel strength of the bonds. The panel was placed on four 1–inch diameter aluminum dowels arranged in a rectangular configuration (see Figure 5.21). The load was applied to the center web using an Instron 4204 Universal Testing Machine and rectangular aluminum jig measuring 0.3" $\times$ 0.3" $\times$ 2". The jig and dowels were covered in felt to prevent scratching of the iridite protective coating. A jack screw lowered the head and the displacement of the head was recorded. A load cell mounted on the head measured the resistance force. A prototype panel was first tested until audible cracking was heard. We tested the flight panels to 70% of the corresponding load. The results are shown in Figure 5.22. None of the panels experienced any yielding or failures. The results also validate the assumption to neglect the thruster holes in the side panel FEM since all of the panels exhibit similar stiffness curves.

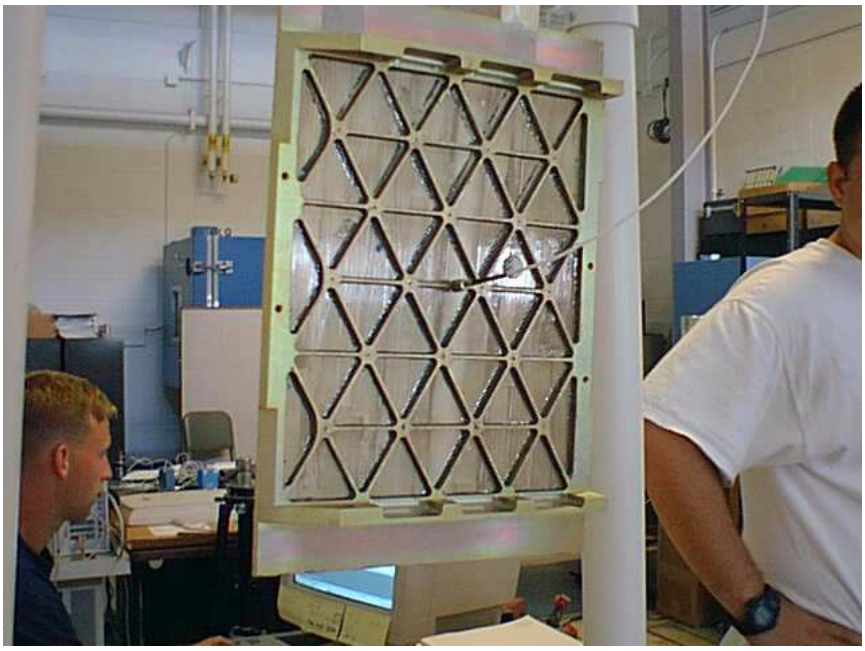

Figure 5.17: Side Panel Modal Test Configuration

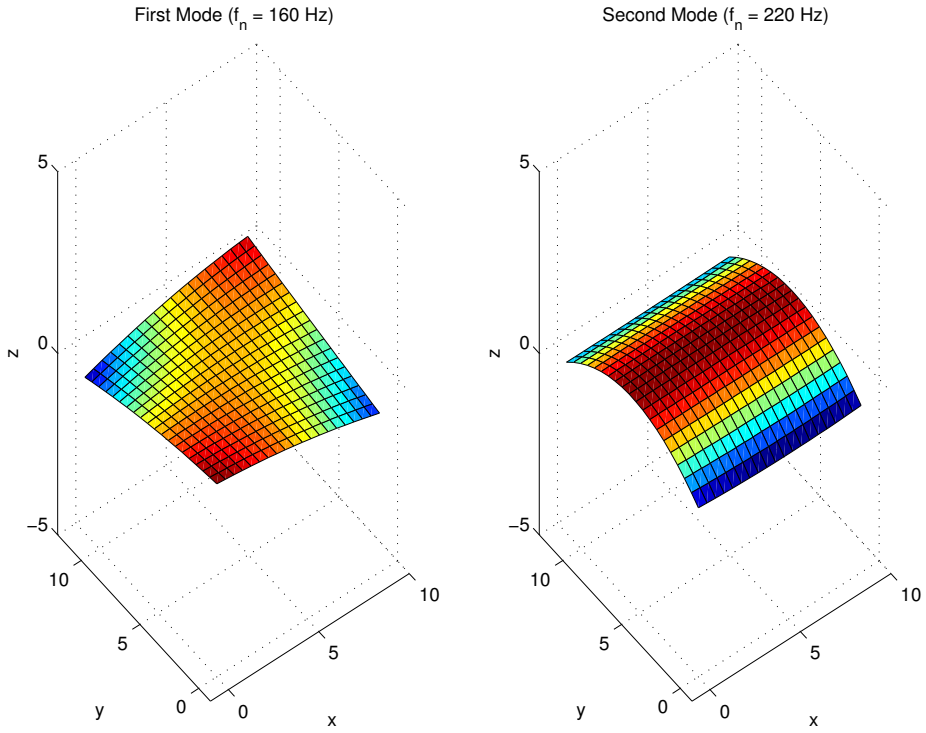

Figure 5.18: Composite Side Panel Modal Analysis Results

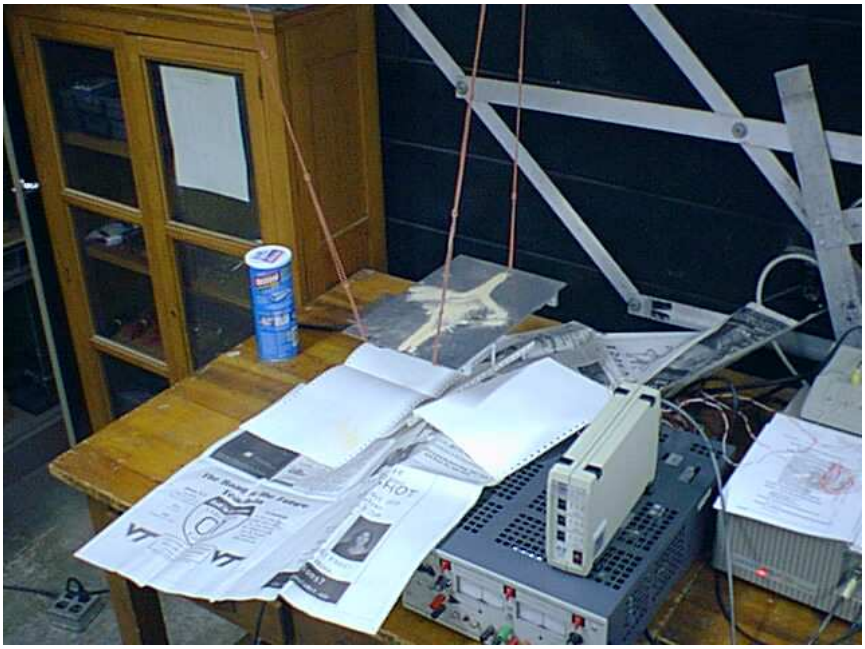

Figure 5.19: Composite Side Panel Chladni Pattern (Mode 1)

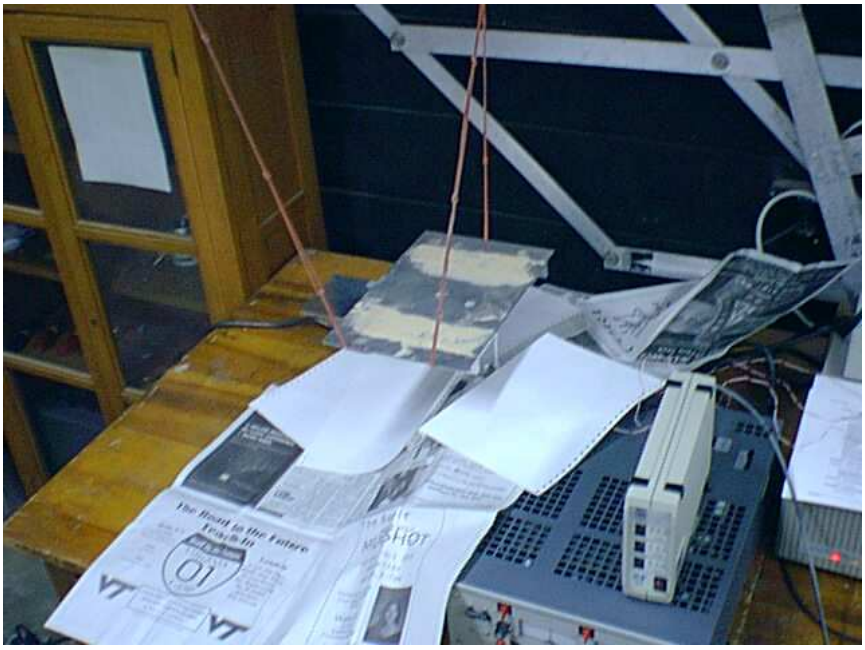

Figure 5.20: Composite Side Panel Chladni Pattern (Mode 2)

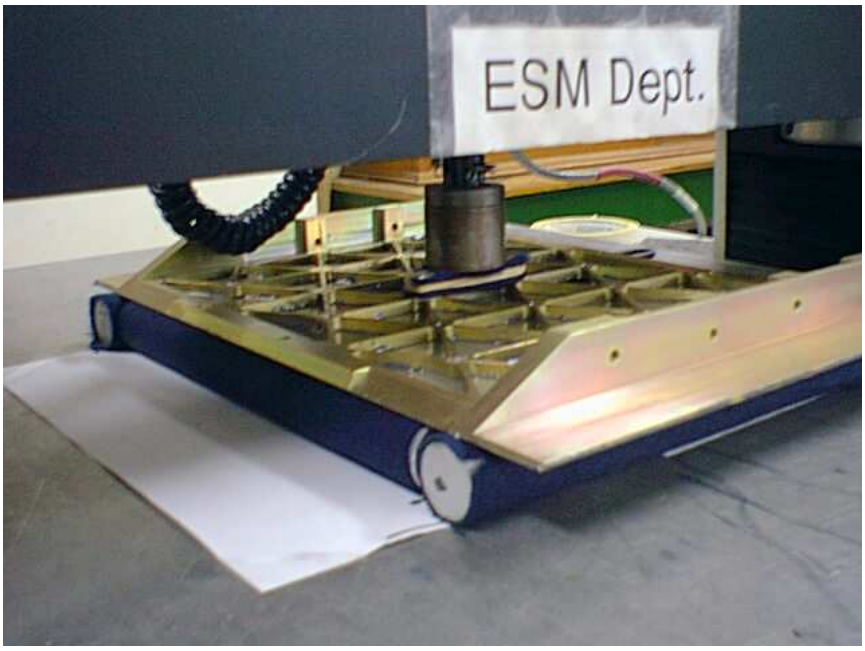

Figure 5.21: Composite Side Panel Static Test Configuration

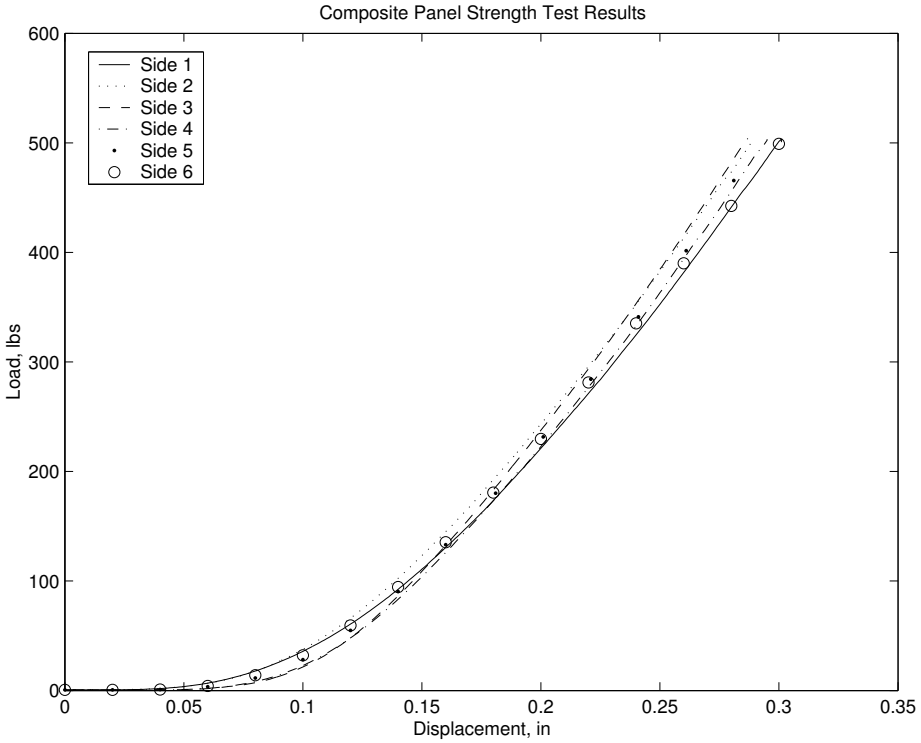

Figure 5.22: Plate Bending Test Results

5.4 Spacecraft Environmental Testing

We conducted the HokieSat environmental testing at NASA Wallops Flight Facility. Vibrational, strength, and mass properties tests were performed to examine the structural integrity of the composite spacecraft assembly. We first tested the prototype structure to investigate the integrity and stiffness properties of the restrained satellite assembly. We then tested the flight structural assembly to test the integrity of the flight components and determine preliminary values of the mass properties.

The SHELS User's Guide [26] requires three types of vibrational and strength tests. The first test typically conducted is a sine sweep, which is a low level modal test (approximately 0.5 *g's*). The sine sweep test uses the vibration table to excite the test article using a sine wave input signal at a range of frequencies. The response is then recorded from mounted accelerometers and both signals are used to compute the frequency response function using fast Fourier transform theory. The test is conducted on three mutually orthogonal axes to determine the complete three–dimensional spectrum. We excited the satellite assembly for frequencies ranging from 20 Hz to 2000 Hz.

The second type of test conducted is a random vibration test. The random vibration test also uses a vibration table to excite the test article. The random frequency spectrum is typically a stationary random process determined using load–coupling analysis and data from a launch vehicle. The stationary random process is typically quantified using an autocorrelation function or a power spectral density. We use a form of the power spectral density called the acceleration spectral density to quantify the accelerations induced by the STS during launch. The acceleration spectral density (ASD) used for the ION–F random vibration test is shown in Figure 5.23. We subjected the HokieSat structural assembly to the same vibroacoustic test environment for 60 seconds.

The final type of test is the sine burst test. The sine burst test is a quasi-static test designed as a strength test for complicated structures. The test is also performed on a vibration table during vibrational testing which makes it more economical than centrifuge or static testing. The shaker induces accelerations on the spacecraft with amplitudes equal to the required limit load factor. The frequency of the sine burst signal is required to be less than one–third the fundamental frequency of the test item to prevent load coupling and dynamic amplification [25]. We performed this test on the HokieSat structural assembly to ensure survivability of components and reveal any design flaws in the developmental process. The sine burst input signal used for the HokieSat test procedure is shown in Figure 5.24. The test is performed on each axis separately to simplify the testing procedure, however, this creates relatively conservative loading requirements. The load factor used in our case is the magnitude of the limit loading vector, 19.05, times the factor of safety for all yielding, 1.25. This corresponds to three uniaxial tests at 23.8 *g's* acceleration. We tested the spacecraft at approximately 27 *g's* for an added factor of safety.

Prototype spacecraft environmental testing was performed at NASA Wallops Flight Facility. Mass models of the major components were constructed and attached to the satellite

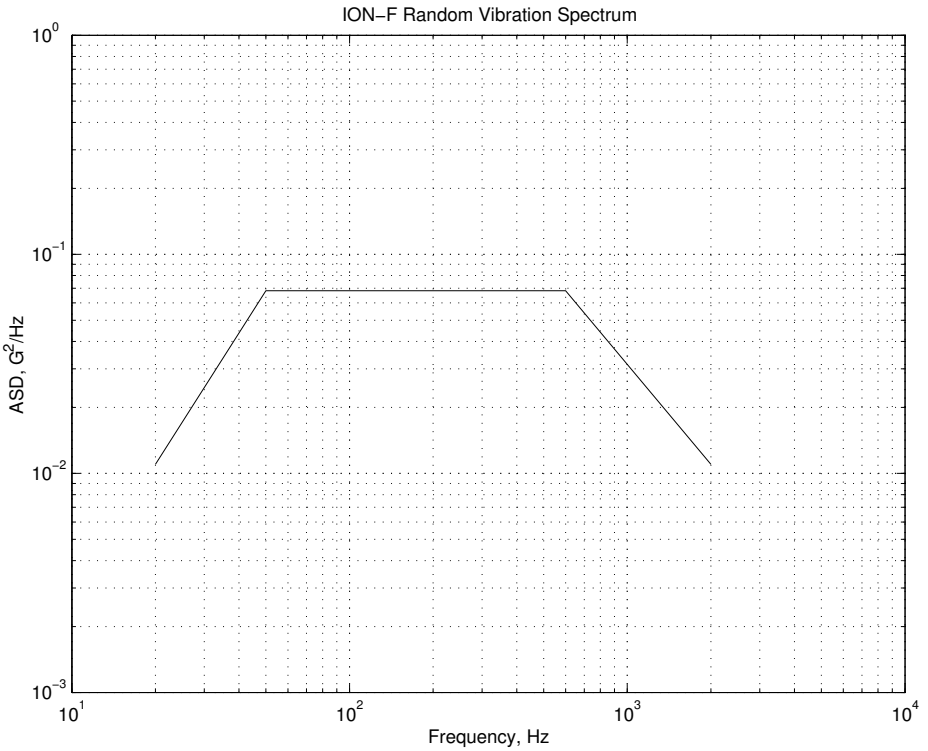

Figure 5.23: Random Vibrational Spectrum Requirements

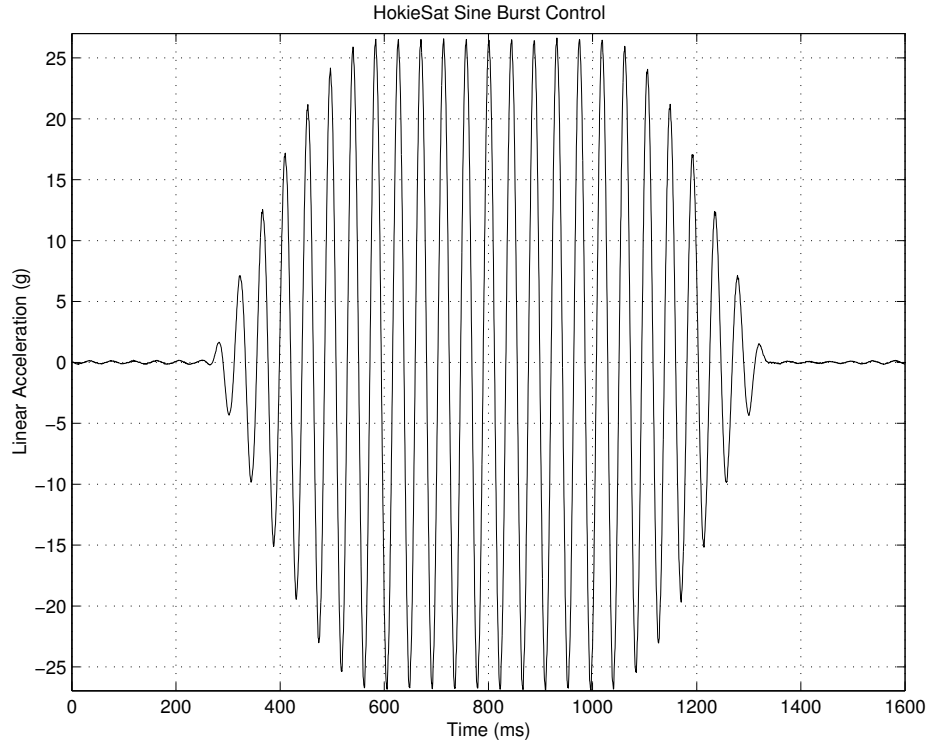

Figure 5.24: HokieSat Sine Burst Test Input Signal

to simulate the integrated system. We also fabricated a fixture to mount the spacecraft to the shaker and simulate the Starsys separation system. Fifteen accelerometers were used to record the accelerations of the major components and panels. We placed the accelerometers at several key locations throughout the spacecraft as shown in Figures 5.25 and 5.26. We inspected the spacecraft for any yielding or failure after each test. The test sequence and results are tabulated in Table 5.6. The assembly passed all testing with no damage except for the final sine burst test. The rectangular torque coil was damaged in the thrust test due to inadequate mounting, as shown in Figure 5.27. The sine sweep results, shown in Figure 5.28, demonstrate a structural fundamental frequency of approximately 78 Hz. The computer electronics enclosure FRF, shown in Figure 5.29, exhibits the nadir panel first mode at approximately 99 Hz. The low end panel natural frequencies are attributed to the added mass of the components. The ill–placed GPS mass model at the center of the zenith panel and high mass concentration are the primary reasons for the lower resonant frequency and higher FRF magnitude of the zenith panel. The prototype dynamic testing provided valuable information about the satellite stiffness properties and survivability of the spacecraft in the launch environment. Using the results of these tests, we were able to devise integration strategies in an attempt to increase the fundamental frequencies of the spacecraft. The structure also exhibited no yielding or buckling during the testing which aided to verification of the design.

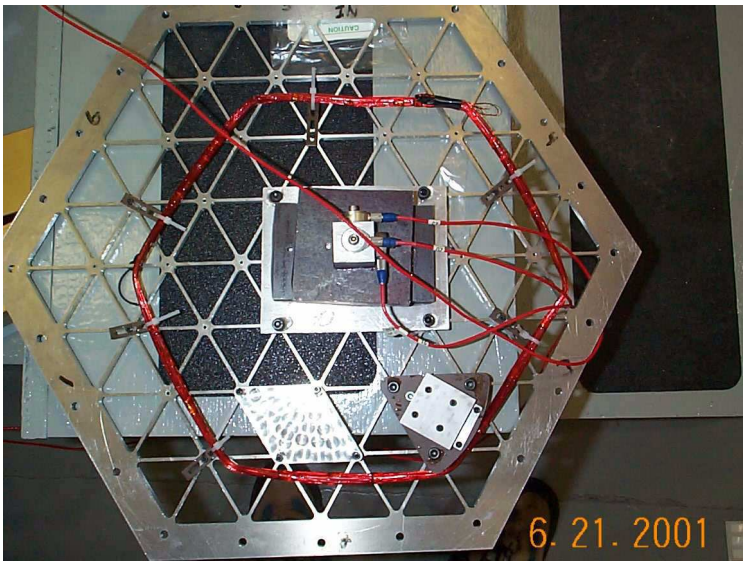

Figure 5.25: Prototype Vibrational Testing Accelerometer Configuration (Zenith Panel)

We also conducted the flight spacecraft environmental testing at NASA Wallops Flight Facility. Similar vibrational testing was performed while adding mass properties testing to determine the inertial properties and the center of mass location of the spacecraft. We began by assembling the spacecraft with all key structural components. Mass models were fabricated for most of the electronics to mitigate overtesting of the electronics boards and

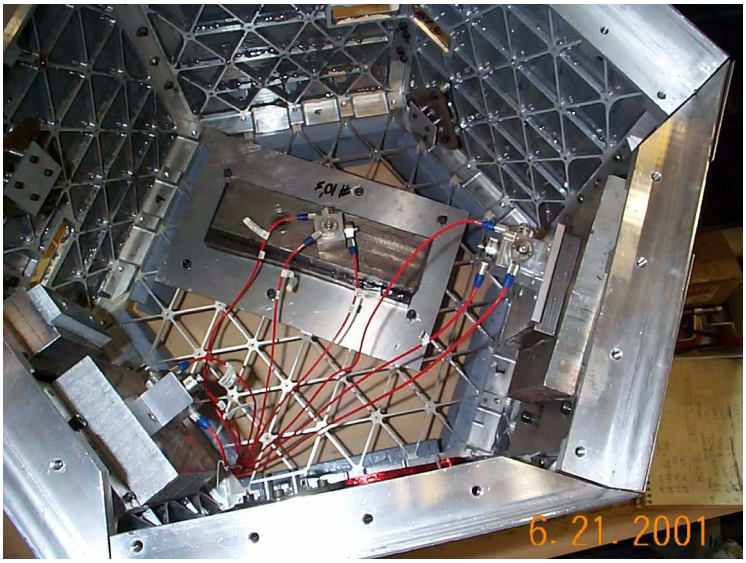

Figure 5.26: Prototype Vibrational Testing Accelerometer Configuration (Nadir Panel)

Table 5.6: Prototype Structure Dynamic Test Sequence and Results

Test	Description	Result
Sine Sweep X	20 – 2000 Hz, 0.5 g RMS	Pass
Random Vibe X	9 g RMS, 1 min	Pass
Sine Burst X	24 g, 23 Hz,	Pass
Sine Sweep Y	20 – 2000 Hz, 0.5 g RMS	Pass
Random Vibe Y	9 g RMS, 1 min	Pass
Sine Burst Y	24 g, 23 Hz	Pass
Sine Sweep Z	20 – 2000 Hz, 0.5 g RMS	Pass
Random Vibe Z	9 g RMS, 1 min	Pass
Sine Burst Z	24 g, 23 Hz	Fail

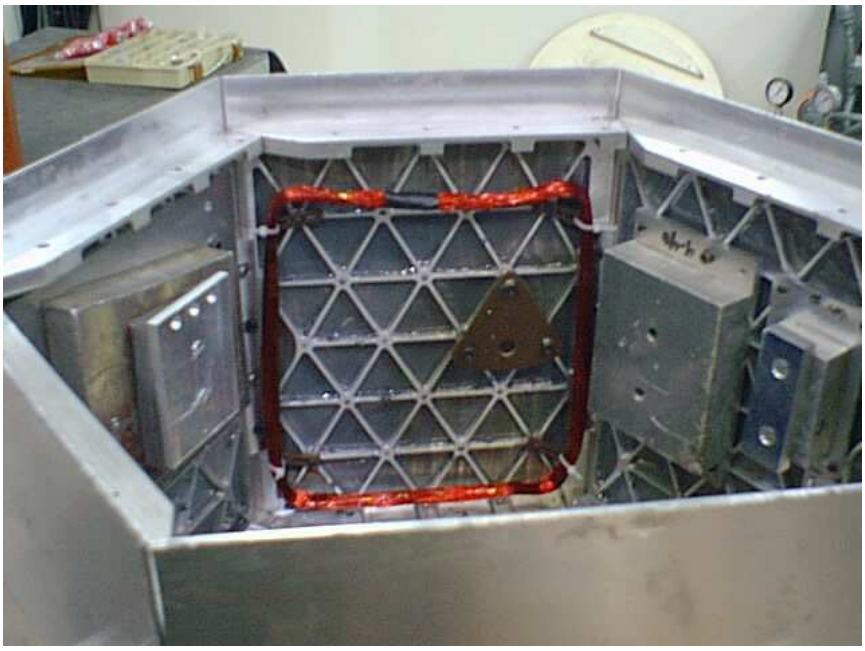

Figure 5.27: Prototype Torque Coil Damaged During Thrust Sine Burst Test

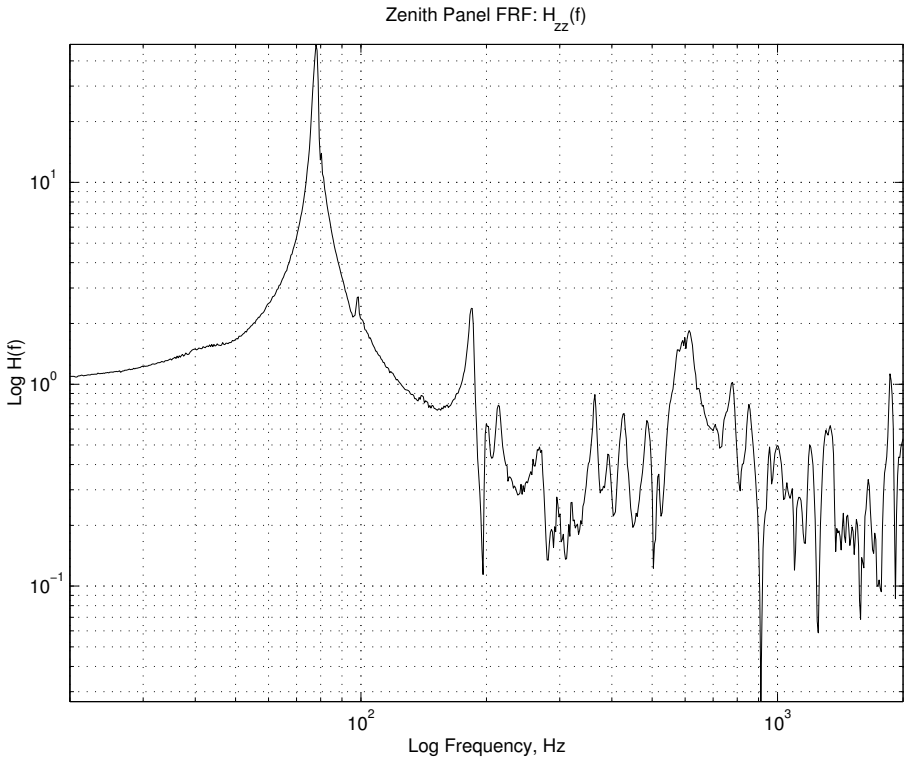

Figure 5.28: Prototype FRF Magnitude for Zenith Panel

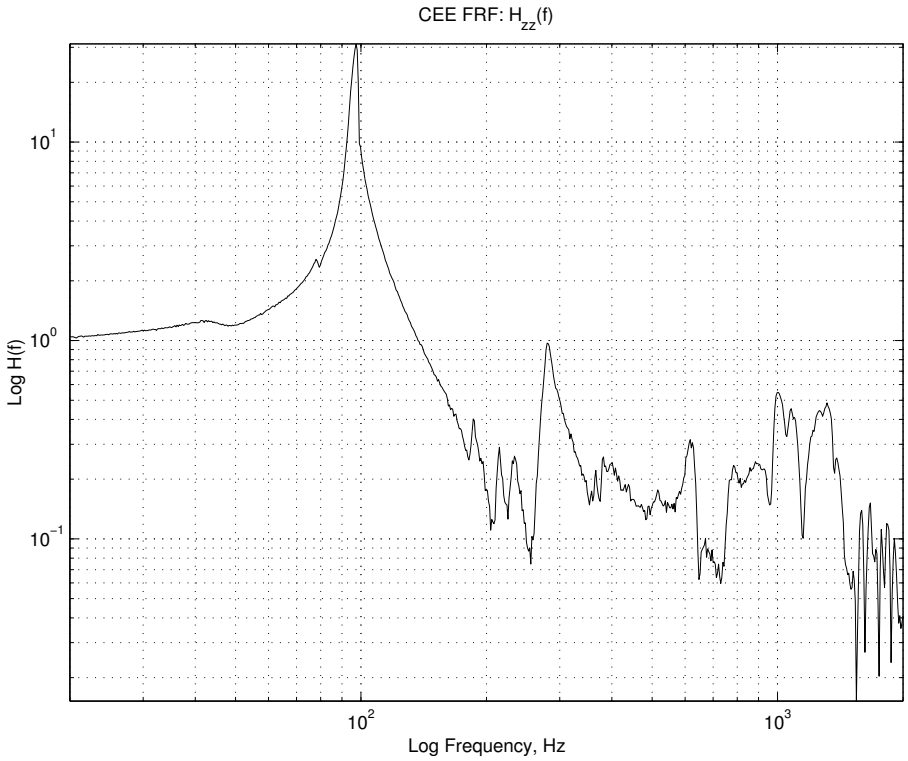

Figure 5.29: Prototype FRF Magnitude for Computer Electronics Enclosure

connections. The test configuration is shown in Figures 5.30 through 5.32 with accelerometers once again placed at key locations throughout the spacecraft assembly. We relocated several components in an attempt to stiffen the end panels and modified the torque coil mounting scheme. We also modified the test procedure to include sine sweep testing after the strength and vibroacoustic tests. This modification enables verification of the structural integrity of the spacecraft by comparing the two frequency response functions. The FRF is examined for large frequency shifts in resonance peaks or large changes in magnitude. Any failures or shifting is usually evident from this analysis. The procedure and results are shown in Table 5.7. The structure passed all tests with no yielding or failures. Improvements were also demonstrated from the prototype testing. The fundamental frequency of the structure increased 35% to approximately 105 Hz, as seen in the CEE FRF shown in Figure 5.34. The first mode remained a "drum mode;" however, it occured on the nadir panel instead of the zenith panel. This change was primarily due to the application of the epoxied honeycomb and the relocation of the GPS hardware. The fundamental frequency of the zenith panel, shown in Figure 5.33, increased over 156% from 78 Hz to nearly 200 Hz using this integration technique. We also see less energy in the fundamental mode due to damping from the epoxy. The CEE assembly was lightened which resulted in a 6 Hz increase in fundamental frequency. The random vibration testing also provided valuable information on the system load coupling. The information learned from the dynamic testing dramatically aided in the development of the spacecraft assembly.

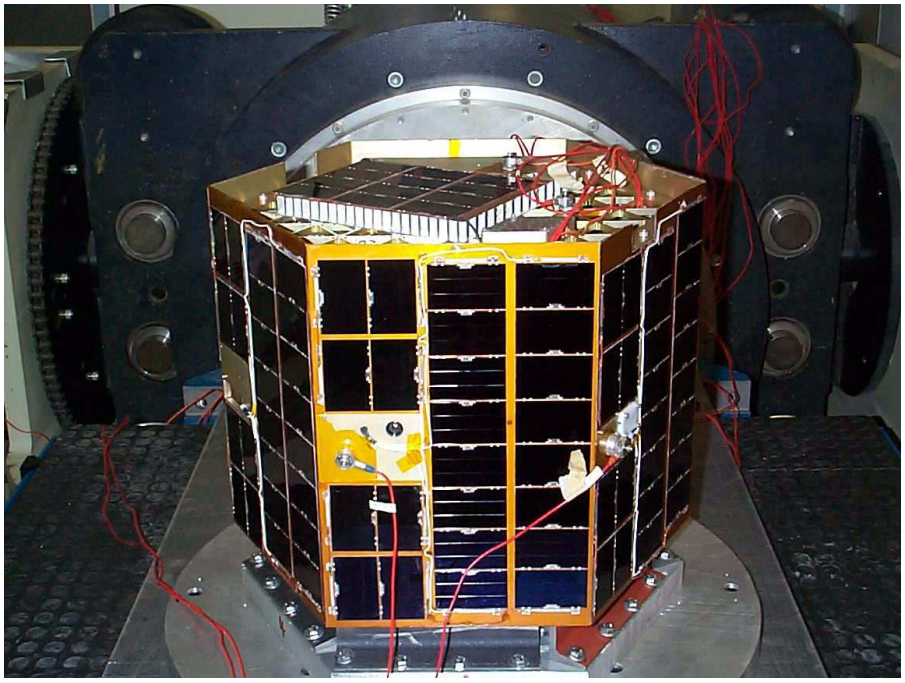

Figure 5.30: Flight Dynamic Testing Accelerometer Configuration

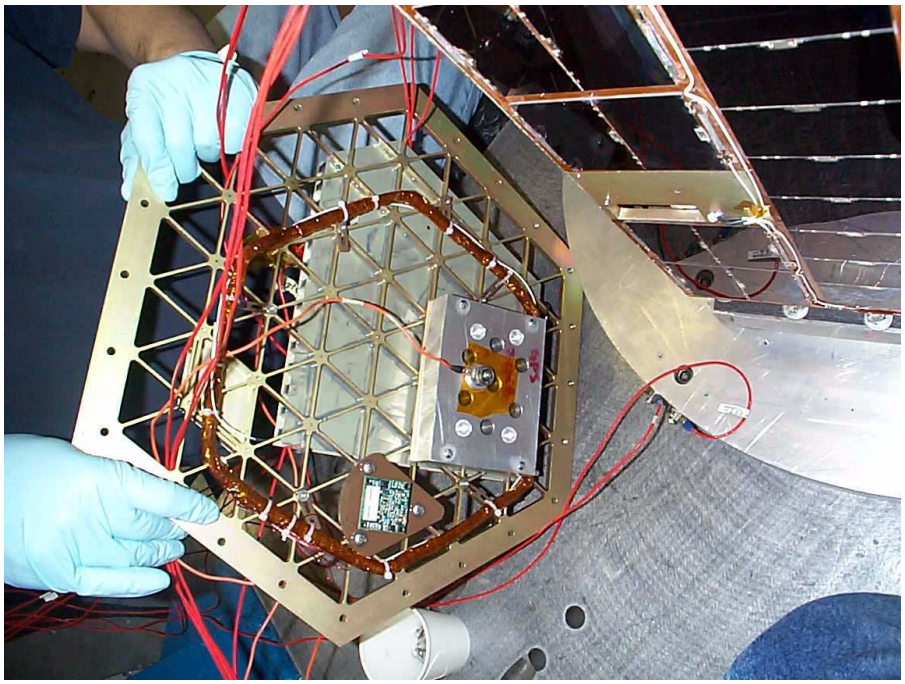

Figure 5.31: Flight Dynamic Testing Accelerometer Configuration (Zenith Panel)

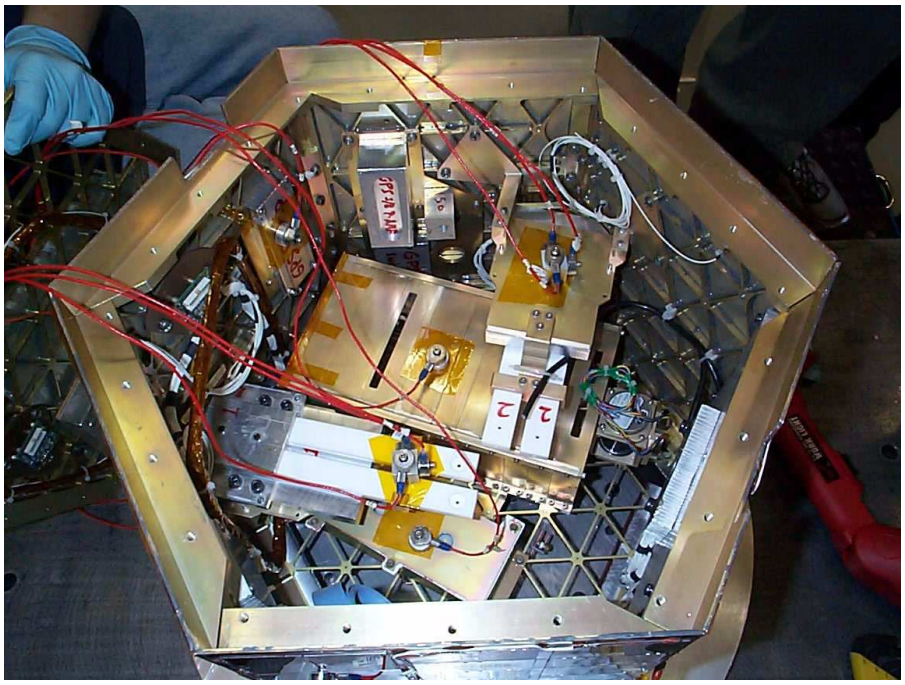

Figure 5.32: Flight Dynamic Testing Accelerometer Configuration (Nadir Panel)

Table 5.7: Flight Structure Dynamic Test Sequence and Results

Test	Description	Result
Sine Sweep X	20 – 2000 Hz, 0.5 g RMS	Pass
Random Vibe X	9 g RMS, 1 min	Pass
Sine Burst X	24 g, 23 Hz,	Pass
Sine Sweep X	20 – 2000 Hz, 0.5 g RMS	Pass
Sine Sweep Y	20 – 2000 Hz, 0.5 g RMS	Pass
Random Vibe Y	9 g RMS, 1 min	Pass
Sine Burst Y	24 g, 23 Hz	Pass
Sine Sweep Y	20 – 2000 Hz, 0.5 g RMS	Pass
Sine Sweep Z	20 – 2000 Hz, 0.5 g RMS	Pass
Random Vibe Z	9 g RMS, 1 min	Pass
Sine Burst Z	24 g, 23 Hz	Pass
Sine Sweep Z	20 – 2000 Hz, 0.5 g RMS	Pass

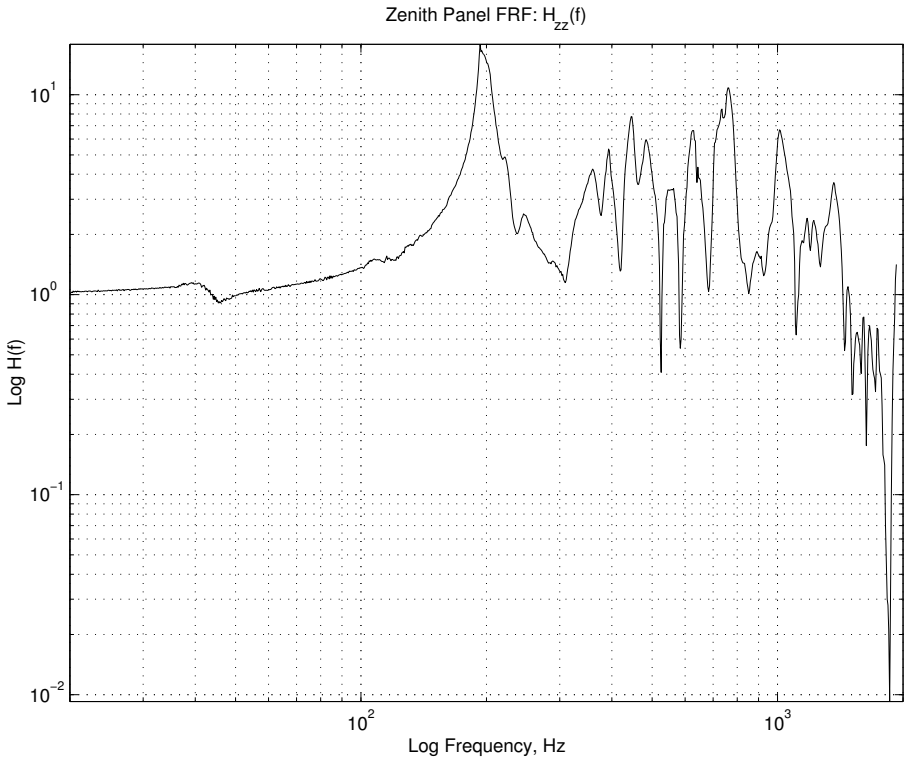

Figure 5.33: Flight FRF Magnitude For Zenith Panel

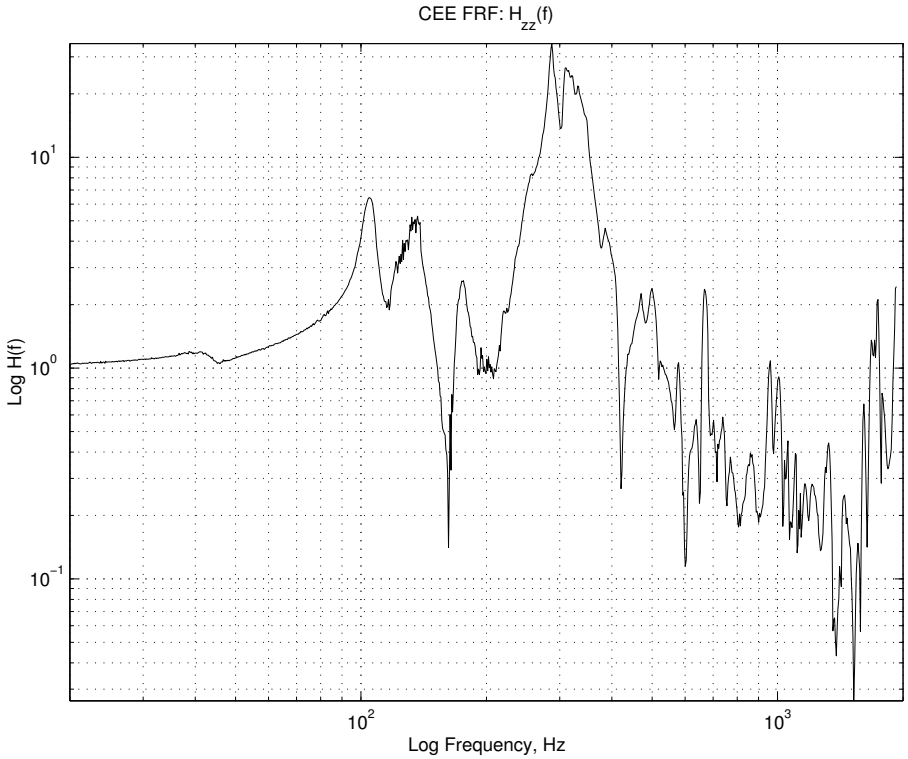

Figure 5.34: Flight FRF Magnitude For Computer Electronics Enclosure

Finally, we experimentally determined the mass properties of the spacecraft. HokieSat was placed on a mass properties table in several different configurations as shown in Figures 5.35, 5.36, and 5.37. These configurations enabled the center of mass to be measured in three dimensions. However, we were unable to tilt the spacecraft due to safety considerations; therefore we did not obtain data for the products of inertia I_{xz} and I_{yz}. We therefore assumed that the z–axis is a principal axis and calculated the principal moments of inertia using eigenvalue theory for rigid body dynamics. The results are shown in Equations 5.16. The center of mass location is measured from the center isogrid node on the nadir panel outer surface. The center of mass is very close to the centroid of the satellite which will enable easy ballasting during the final spacecraft assembly. The location also helps satisfy the ION–F mass properties SUG requirements.

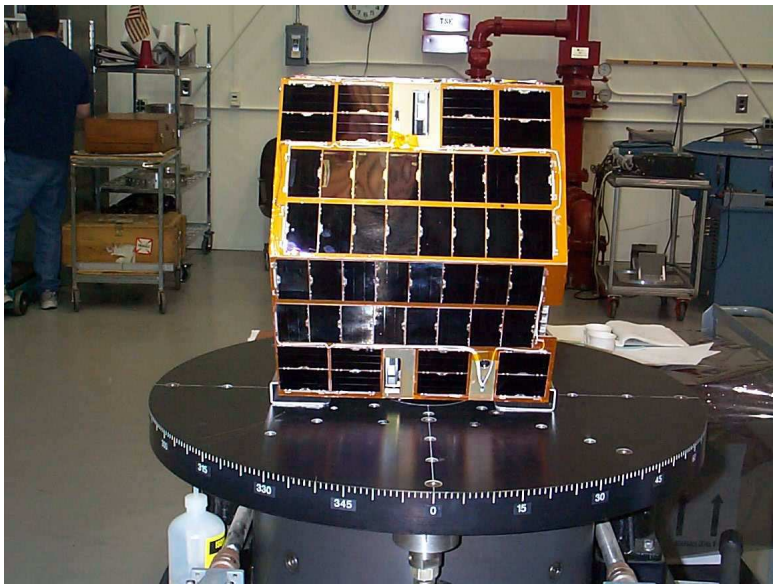

Figure 5.35: Mass Properties Testing Configuration

$$\begin{aligned} \vec{r}_{c/o} &= \{0.10871, 0.03608, 5.81398\} \text{ inches} \\ \vec{I}_p &= \{0.2799, 0.3017, 0.3341\} \text{ slug-ft}^2 \end{aligned} \tag{5.16}$$

Figure 5.36: Mass Properties Testing Configuration

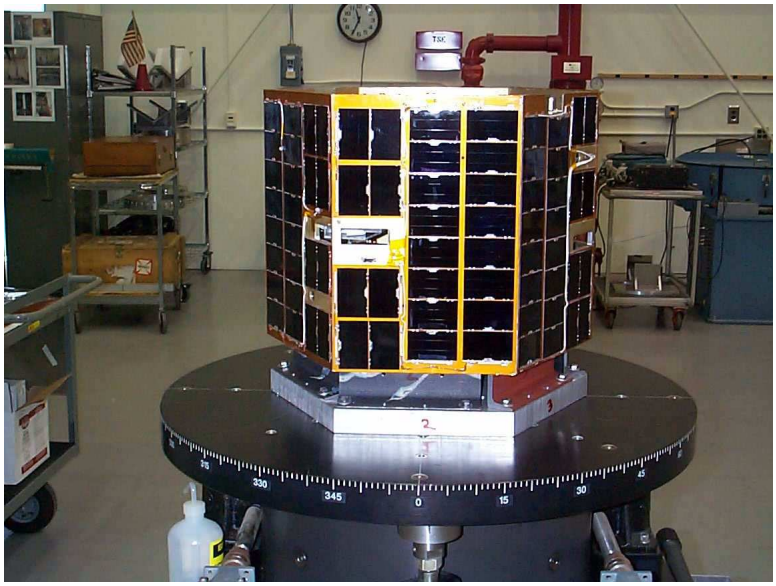

Figure 5.37: Mass Properties Testing Configuration

5.5 ION-F Model

We constructed a finite element model of the ION–F stack configuration. The other satellites, Dawgstar and USUSat, and the Lightbands were modeled using previous stack model properties [2]. The model is shown in Figure 5.38. We created a composite isogrid structure for Dawgstar in I-DEAS using an array of elements similar to the HokieSat FEM assembly. USUSat was constructed using 0.25–inch thick linear quadrilateral and triangular shell elements. The USUSat isogrid was not modeled due to its relatively little contribution to the stack stiffness. Non–structural mass was added as point masses at central nodes in the corners of the other two spacecraft to account for the component masses. We also represented component masses in HokieSat by distributing point masses at the component mounting locations. The Lightband model was attached to the satellites at the end panel attachment points. The separation systems were modeled using uniform 0.150–inch thick linear quadrilateral shell elements.

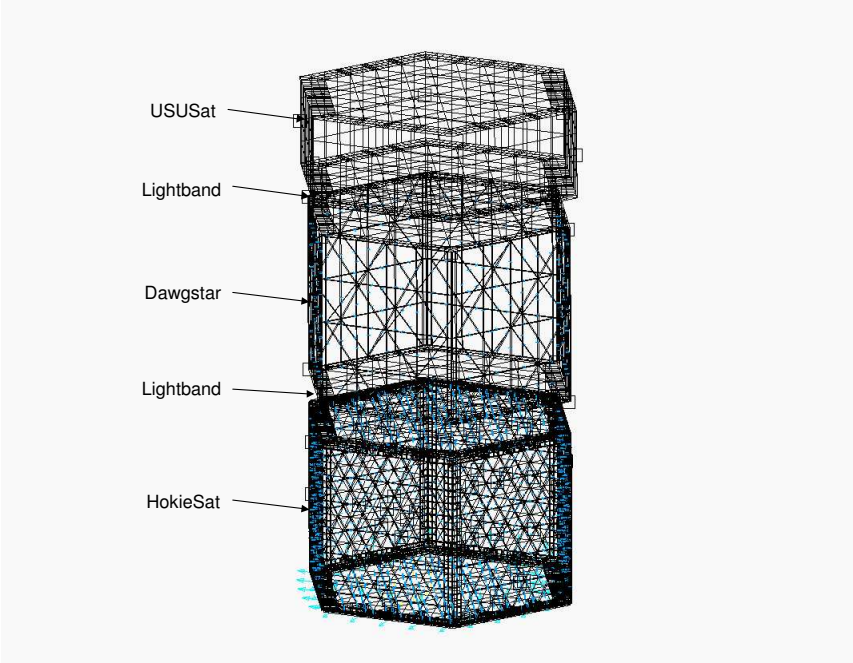

Figure 5.38: ION–F FEM Mesh Configuration

We first verified the boundary conditions of the stack FEM using static strength and stiffness testing. We assumed that the first mode is a cantilever mode. We also assumed that the largest accelerations during launch are along the STS x–axis (roll axis). We thus tested HokieSat in a cantilever configuration as it will be oriented in the Space Shuttle. The test was conducted in three phases [30]. The first phase involved testing of the truss fixture built to apply the loads to the spacecraft (see Figure 5.39). The truss measured 35 inches in length and was assembled using aluminum members. The truss applied a significant moment to the spacecraft to simulate the launch load conditions. The truss was attached

to several solid aluminum entities that allowed connection to the spacecraft and application of the loads. The entire fixture was mounted to a rigid back wall constructed out of steel I-beams to provide rigid boundary conditions. A load was then applied at the end of the fixture and the corresponding deflections at that point were recorded using a linear dial gage. The next phase of the testing included the isogrid structural assembly. The spacecraft was mounted to the back wall using a separation system fixture to simulate the correct load path (see Figure 5.40). We next mounted the truss fixture to the spacecraft as shown in Figure 5.41. The loads and deflections were then applied and measured, respectively. The last phase of the static testing examined the composite structural assembly in a similar set up as the isogrid testing. This testing procedure provided a thorough investigation of all of the configurations. We used the truss testing as a tare measurement of the experiment. This measurement enabled values of the satellite deflections to be calculated. The experiment also allowed a comparison of the isogrid panel assembly and the composite panel assembly stiffnesses. The results are plotted in Figure 5.42. The composite side panels demonstrate a 32% increase in stiffness in the cantilever mode while increasing less than 8% in total mass. The results therefore show a 22% increase in stiffness per mass of the spacecraft in the cantilever mode. These results show similar correlation with the side panel modal analysis results above. The results also allow correlation of the test and model boundary conditions. We first created a finite element model of the truss and attach it to the satellite separation system nodes as shown in Figure 5.43. We then solved the model for the loading conditions used in the testing and determine the corresponding deflection. Using an iterative procedure, we determined the stiffness of the truss material required to give the measured truss deflection. The results are shown in Figure 5.44. We demonstrated an error in stiffness of less than 1% using a linear least squares analysis. We considered this an acceptable error.

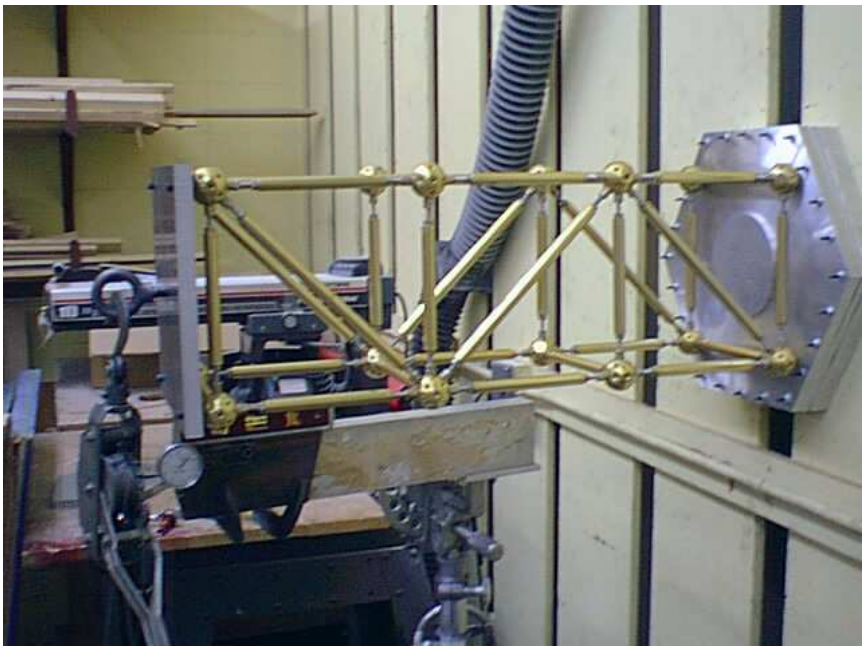

Figure 5.39: Truss Fixture Testing Configuration

Figure 5.40: Separation System Fixture

We next correlated the testing boundary conditions of the composite structural assembly with the FEM. We began by solving the composite model and truss fixture test configuration model at the corresponding test load conditions. We refined the boundary conditions using an iterative procedure until the deflections matched the measured deflections within acceptable error. The results are shown in Figure 5.45. The truss exhibited geometric nonlinearities at the higher loads. We therefore correlated the linear section of the experimental curve to the FEM to less than 5% error using a linear least squares analysis. The corresponding boundary conditions incorporated changes to the original assembly model. The nadir Starsys separation system attachment points are constrained in all translational degrees of freedom. The flanges are modeled using solid elements due to their contribution to the structural stiffness. The end panels are connected to the flanges using rigid elements to simulate the clamping effect of the separation systems. We therefore considered these boundary conditions to be correct.

We also performed a modal analysis on the ION–F stack configuration. The boundary conditions of the stack interface plane were chosen based on the correlation analysis above. The first and second modes are shown in Figures 5.46 and 5.47. The fundamental mode occurs at a frequency of 47 Hz. Both modes are cantilever modes flexing nominally about the major and minor axes of the stack. The strain energy plot reveals that the majority of the flexing in the assembly occurs in the Lightband FEM. We assumed that the model is sufficient for our analysis; however further investigation of the Lightband structural properties is recommended. A fundamental frequency of 47 Hz for the ION–F stack reveals possible stiffness problems for the MSDS and stack assembly. The SHELS User's Guide [26] requires that the payload have a fundamental frequency greater than 35 Hz. Satisfaction of these requirements may be difficult to attain as a payload assembly. The ION–F stack

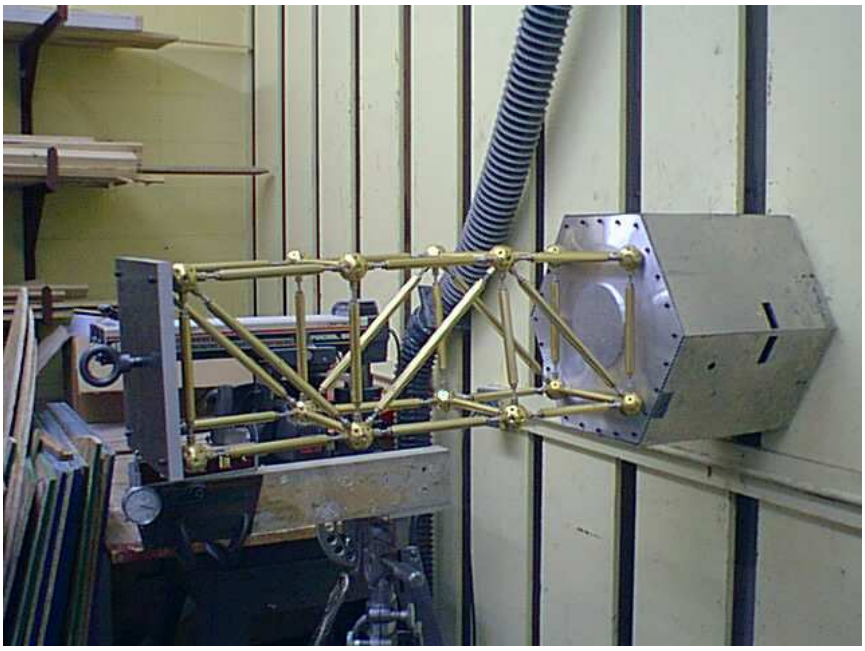

Figure 5.41: Satellite Testing Configuration

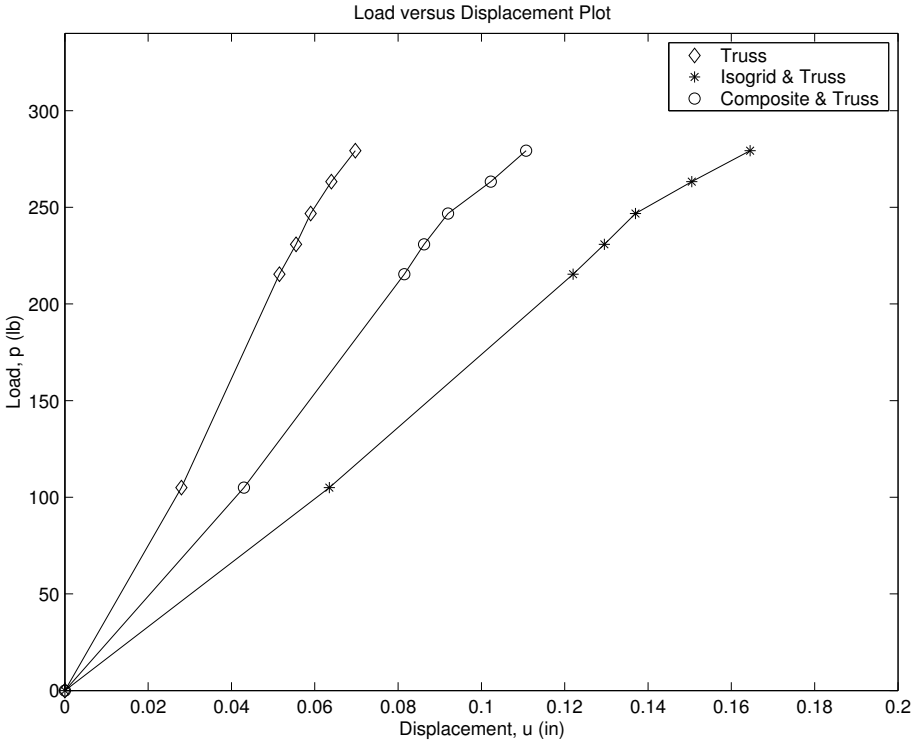

Figure 5.42: Results of Cantilever Strength and Stiffness Tests

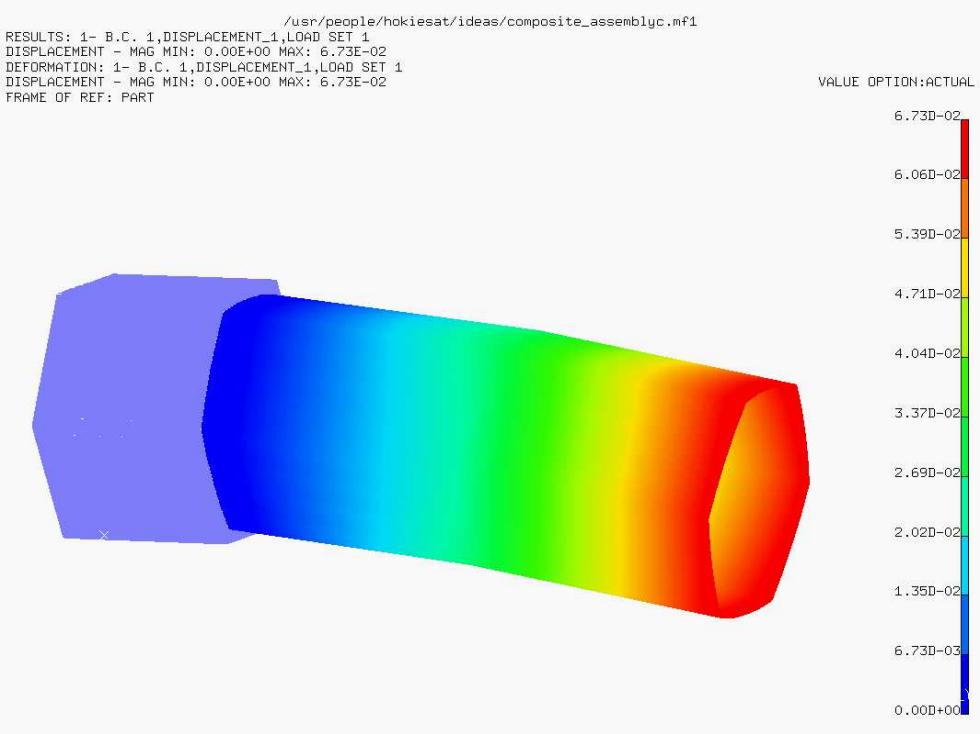

Figure 5.43: Truss FEM Analysis

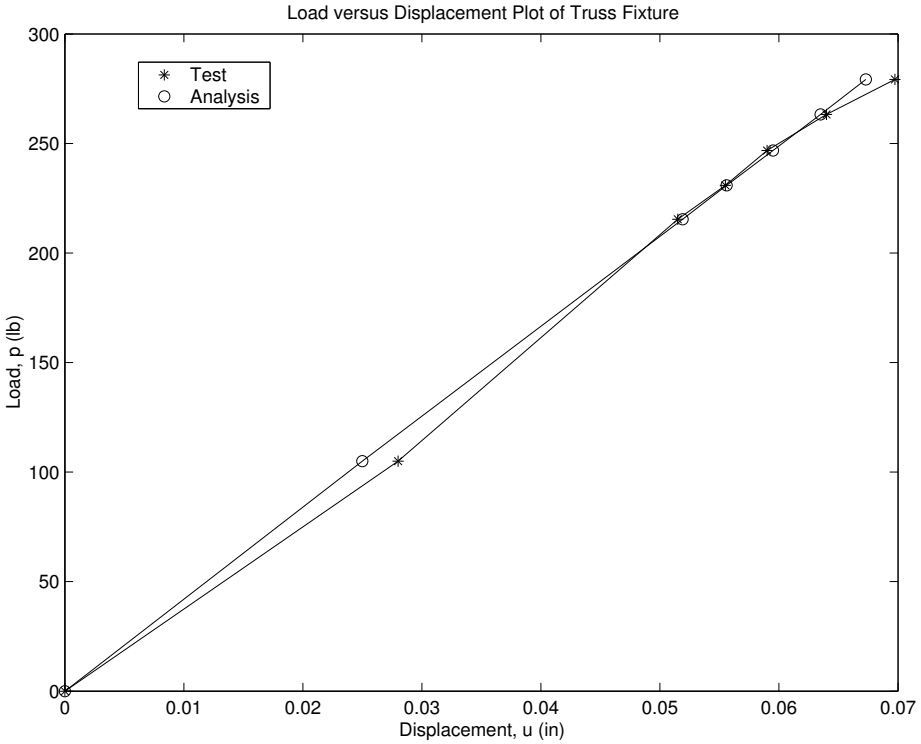

Figure 5.44: Correlation of Truss Model and Truss Testing

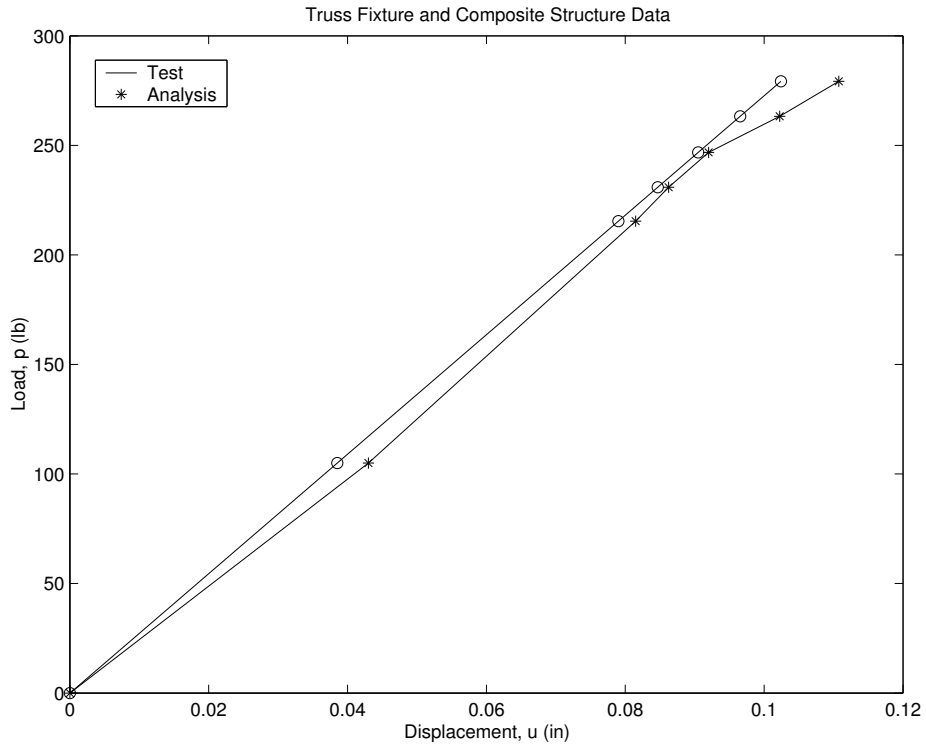

Figure 5.45: Correlation of Composite/Truss Model and Testing

environmental testing will determine the accuracy of the model.

We next performed a stress analysis of the ION–F stack. The SUG requirements stated in Table 5.1 were first investigated to determine the integrity of the stack. The results from the analysis were shown in Table 5.8. The margins of safety were calculated using Equation 5.1 and the required factors of safety. The results revealed that HokieSat and the ION–F stack exhibit no failures and pass the SUG structural requirements.

We next investigated survivability during sine burst testing. As stated above, the frequency of the sine burst signal is required to be less than one–third the fundamental frequency of the test item to prevent load coupling and dynamic amplification. Therefore, the frequency of the sine burst should be no more than 15.67 Hz as determined by the modal analysis. This low frequency could create test procedural limitations due to the relatively large stroke required at this low frequency. We will assume that a facility is available to conduct the stack tests; however, further investigation is recommended. The sine burst test corresponds to three uniaxial tests at 23.8 g's acceleration. We therefore performed a stress analysis for the sine burst test by applying uniform accelerations along each of the three orthagonal axes. The worst case stresses are exhibited while applying the acceleration along the spacecraft x-axis (major axis). The x-axis testing results are plotted in Figures 5.48 and 5.49. The other results are shown in Appendix A. The plots demonstrate that the HokieSat structure survives all test loading with no yielding or failures.

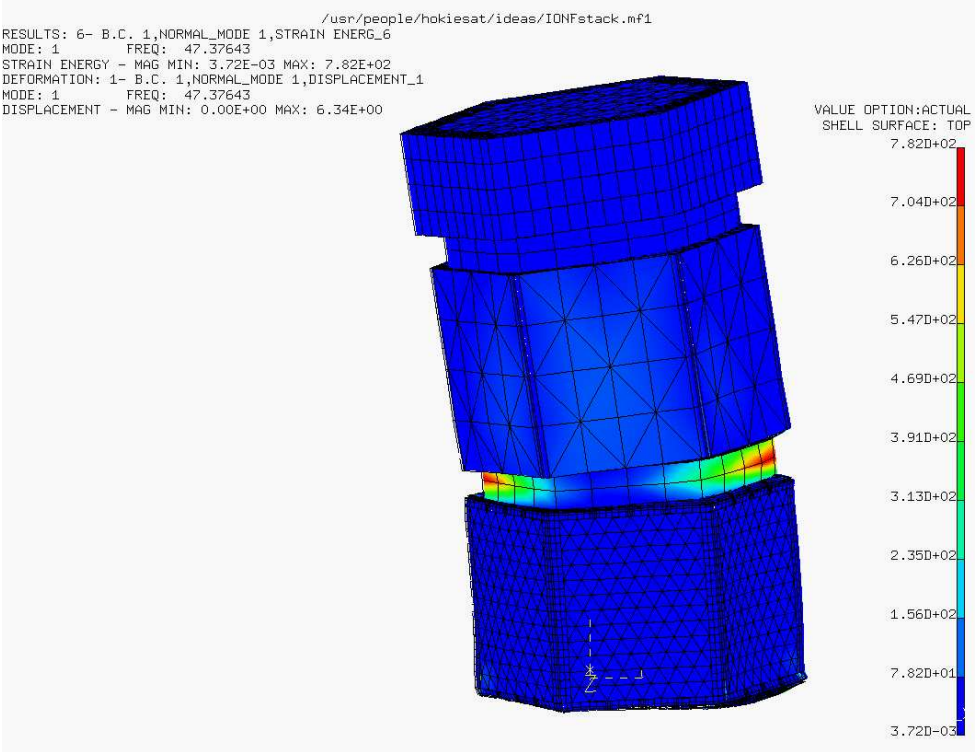

Figure 5.46: ION–F FEM First Mode ($f_n = 47$ Hz)

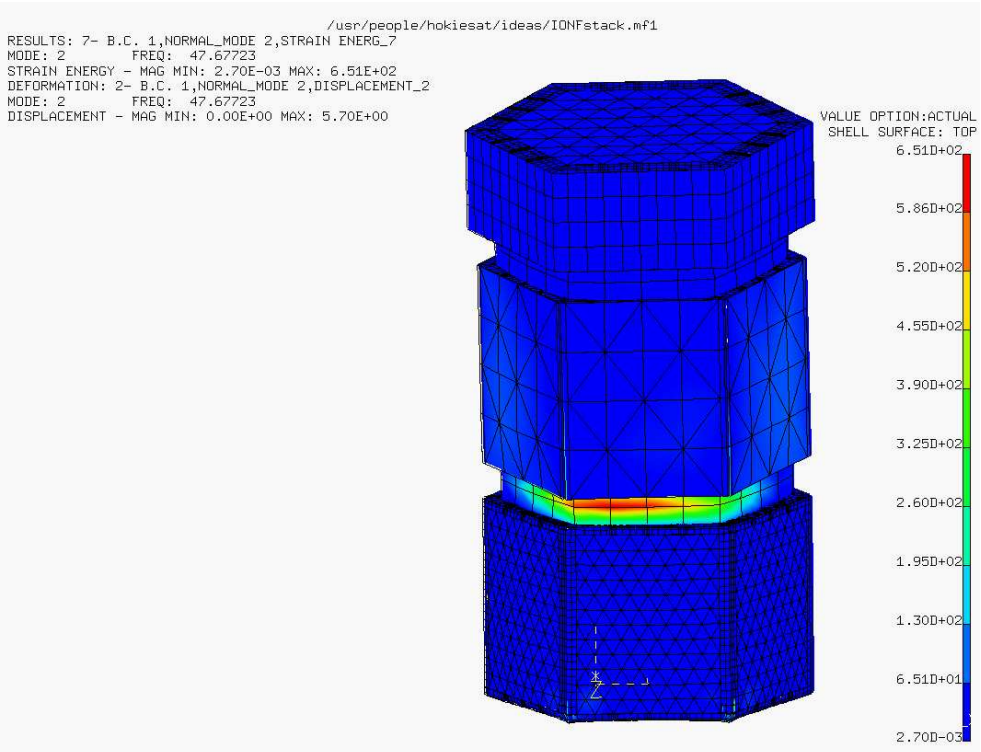

Figure 5.47: ION–F FEM Second Mode ($f_n = 48$ Hz)

Table 5.8: ION–F FEM Stress Analysis Results

Gravity Vector (g's)	$\sigma_{max}(ksi)$	MS_{yield}	$MS_{ultimate}$
$\{11, 11, 11\}$	24.2	0.157	0.122
$\{-11, -11, -11\}$	24.2	0.157	0.122
$\{11, -11, -11\}$	24.8	0.129	0.094
$\{-11, 11, -11\}$	22.0	0.273	0.234
$\{-11, -11, 11\}$	23.0	0.217	0.180
$\{-11, 11, 11\}$	24.8	0.129	0.094
$\{11, -11, 11\}$	22.0	0.273	0.234
$\{11, 11, -11\}$	23.0	0.217	0.180

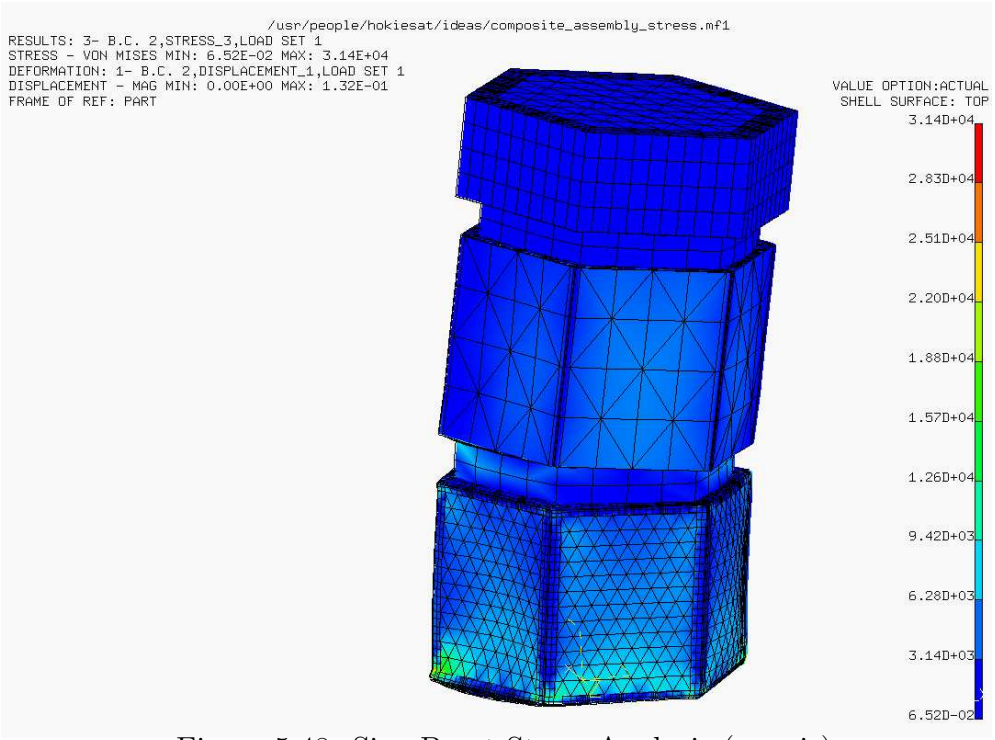

Figure 5.48: Sine Burst Stress Analysis (x–axis)

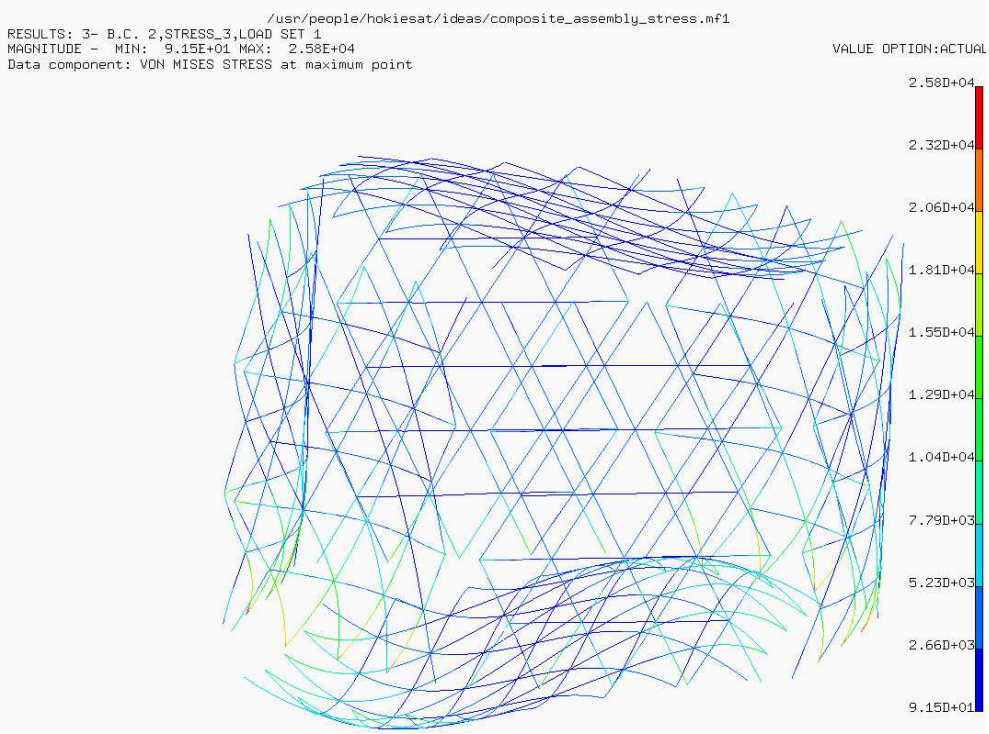

Figure 5.49: Sine Burst Rib Stress Analysis (x–axis)

5.6 Summary

In this chapter we presented the analysis and testing techniques used to verify the structural integrity of the HokieSat structure. The preliminary analysis was presented and the isogrid theory used in the approximation was derived. The isogrid finite element model was developed and verified using modal experimentation. The composite side panel finite element model was constructed using offset elements and the model was also verified using modal experimentation. We demonstrated a nominal 22% gain in structural efficiency by applying the composite side panel design. The composite side panel manufacturing and strength were verified using plate bend testing. The HokieSat prototype and flight structural assemblies underwent vibrational testing at NASA Wallops Flight Facility resulting in no catastrophic damage. We created a finite element model of the ION–F stack configuration and verified the boundary conditions using static testing. We determined the first two modes of the ION–F stack and performed a stress analysis on the stack to satisfy the NASA SHELS user's guide requirements. Finally, we performed a stress analysis under the sine burst testing conditions. We thus have verified the structural integrity of the HokieSat composite structure.

Chapter 6

Summary and Conclusions

The purpose of this thesis was to design, analyze, fabricate, and test a nanosatellite for flight qualification aboard the NASA STS. In Chapter 1, we began the design process with a literature review of past spacecraft missions. We then examined the designs of these spacecraft to determine the most plausible configuration for our mission. In Chapter 2, we investigated several materials and methods used to optimize the structural properties of spacecraft assemblies. We chose aluminum isogrid as the most efficient design for our program. We then described the design of the spacecraft and the entire satellite configuration in Chapter 3. In Chapter 4, we described the CNC manufacturing techniques used to fabricate the isogrid and the conventional methods used to fabricate the remaining structural components. We described the meticulous lay–up procedure required for the composite side panels. In Chapter 5, we presented the entire verification process used to determine survivability of the structure. We used isogrid theory to size the preliminary design of the spacecraft. We applied the theory to results of the finite element analysis to arrive at the design. We then create an isogrid finite element model to more accurately model the structure and increase our panel thicknesses to 0.250 inch. We then created the composite side panel model using offset shell elements and investigated the properties of the assembly. We verified the models using modal analysis techniques. We performed environmental testing on the satellite assembly at NASA Wallops Flight Facility. We devised integration methods to raise the fundamental frequency of the structure and reduce the dynamic amplification of the loading on critical components. We then used the data to create a FEM of the ION–F stack. We verified the boundary conditions of the model by correlating the displacement data recorded from static cantilever testing. We conducted a modal analysis revealing that the first mode of the ION–F stack is 47 Hz. Finally, we conducted a stack level stress analysis. We proved that the structure will survive all environmental and test loads.

We developed a satellite structure that incorporates a conventional isogrid design with a modern composite assembly technique. The isogrid configuration allows for efficient mounting of the components including several revolutionary nanotechnologies. We also demonstrated a 22% gain in structural efficiency by incorporating epoxied skins in the composite structural configuration. The environmental testing results demonstrated that the epoxied

honeycomb construction increased the stiffness of the zenith panel by over 156% and also increased dampening of the assembly. The testing showed a HokieSat structure fundamental frequency of 105 Hz. The composite side panel manufacturing used a space–rated 2216 gray epoxy which allowed for a simple lay–up procedure. The development process incorporated several undergraduate and graduate students at all levels. The students were able to fabricate and handle the hardware, and the environmental testing was conducted primarily by students. We verified the integrity of the key structure in the unique ION–F stack configuration using finite element analysis. This configuration is essential for ION–F to fly in one of the first autonomous formation flying missions.

Bibliography

[1] Alexandria Metal Finishers Inc., Lorton, VA. *Military Plating Specifications*, 2000.

[2] John R. Anderson. Structural Design and Manufacturing of Dawgstar Nanosatellite. Master's thesis, University of Washington, 2001.

[3] David M. Barnett, Suraj P. Rawal, and Kevin Rummel. Multifunctional Structures for Advanced Spacecraft. *Journal of Spacecraft and Rockets*, 38(2):226–230, 2001.

[4] Ann W. Bergquist. *VT HokieSat Side Panel Assembly Procedure*. Virginia Polytechnic Institute and State University, Blacksburg, VA, 2001. AA–22901–DOC001.

[5] Boeing Satellite Systems. Webpage. http://www.hsc.com/flash.html, 2002.

[6] C. E. Brackett. AFRL's Multi-Satellite Deployment System (MSDS). In *15th Annual AIAA/USU Conference on Small Satellites, Logan, Utah, August 13-16, 2001*. AIAA, 2001.

[7] Mark Campbell, R. Rees Fullmer, and Christopher D. Hall. The ION-F Formation Flying Experiments. In *Space Flight Mechanics 2000*. AAS/AIAA, 2000. AAS 00-108.

[8] Shelley B. Conkey, Chiachung Lee, Steve Chaykovsky, David Content, Armando Morell, and Jason Budinoff. Optimum Design of a Lightweight Mirror Using Aluminum Foam or Honeycomb Sandwich Construction - A Case Study for the GLAS Telescope. In *Current Developments in Lens Design and Optical Systems Engineering; Proceedings of the Conference, San Diego, CA, Aug. 2-4, 2000*, volume 4093, pages 325–332. Society of Photo-Optical Instrumentation Engineers, 2000.

[9] John T. Dorsey and James W. Dyess. *Structural Performance of Two Aerobrake Hexagonal Heat Shield Panel Concepts*. NASA, 1992. NASA Technical Memorandum 4372.

[10] Kristen Gledhill, Thomas D. Kim, John G. Paul, and Randy Boswell. The Next Generation of Solar Panel Substrates. In *Intersociety Energy Conversion Engineering Conference, Orlando, Florida, Jul. 30–Aug. 4, 1995*, volume 1, pages 333–336. ASME. AP–109.

[11] Joseph P. Greathouse, Mark V. Hines, Kevin K. Jezak, R. Gilbert Moore, Reed M. Nielson, Rex Ridenoure, and G. William Watt. The ISOSAT Small Satellite–A Design in Isogrid Technology. In *6th Annual AIAA Utah State University Conference on Small Satellites, Logan, Utah, Sept. 21–24, 1992*. A94–14322.

[12] H. R. Grooms, C. F. DeBarro, and S. Paydarfar. "What is an Optimal Spacecraft Structure?". *Journal of Spacecraft and Rockets*, 29:480–483, 1992. no. 4, July–August.

[13] E. Nathan Harris and Daniel R. Morgenthaler. Design and Testing of Multifunctional Structure Concept for Spacecraft. In *The 41st Structures, Structural Dynamics, and Materials Conderence and Exhibit, Atlanta, GA*. AIAA/ASME/ASCE/AHS/ASC, 2000. AIAA-2000-1555.

[14] Walter Holemans. *Private Correspondence*. Planetary Systems Corporation, Silver Spring, MD, 1999.

[15] Walter Holemans. *Lightband Interface Control Document*. Planetary Systems Corporation, Silver Spring, MD, 2000. PSC Document 2,000,421 REV B.

[16] Steven Huybrechts and Stephen W. Tsai. Analysis and Behavior of Grid Structures. *Composites Science and Technology*, 56:1001–1015, 1996.

[17] Cyrus D. Jilla and David Miller. Satellite Design: Past, Present and Future. *International Journal of Small Satellite Engineering*, 1, 1997. Online journal located at http://www.ee.surrey.ac.uk/EE/CSER/UOSAT/IJSSE/issue1/issue1.html.

[18] Thomas D. Kim. Fabrication and Testing of Composite Isogrid Stiffened Cylinder. *Composite Structures*, 45:1–6, May 1999.

[19] Thomas D. Kim and Christopher A. Rotz. Warping of Flat Composite Isogrid Panels. In *IEEE Aerospace Conference Proceedings*, pages 271–277. IEEE, February 1997.

[20] J. L. Koury, T. D. Kim, J. J. Tracy, and J. A. Harvey. Continous Fiber Composite Isogrid Structures for Space Applications. In *Proceedings of the 1993 Conference on Processing, Fabrication and Applications of Advanced Composites, Long Beach, California, Aug. 9–11 1993*, pages 193–198. A95–24630.

[21] R. A. Lauer, D. J. Podlesney, and D. A. Aievoli. The TIROS Isogrid Instrument Mounting Platform. In *The National Symposium and Workshop on Optical Platforms*, volume 493, pages 272–285. SPIE.

[22] Pat L. Mangonon. *The Principles of Materials Selection for Engineering Design*. Prentice Hall, Upper Saddle River, NJ, 1999.

[23] McDonnell Douglas Astronautics Co., Huntington Beach, CA. *Isogrid Design Handbook*, 1973.

[24] NASA. Webpage. http://www.nasa.gov, 2002.

[25] NASA Goddard Space Flight Center, Greenbelt, MD. *NASA Preferred Reliability Practices: Sine–Burst Load Test*, 1990. PT–TE–1420.

[26] NASA Goddard Space Flight Center, Greenbelt, MD. *SHELS User's Guide*, 1999. SSPP-SPEC-040.

[27] Bhavesh T. Patel, Susanne Schroll, and Andrew Lewin. On-orbit Performance of the ORBCOMM Spacecraft Constellation. In *Proceedings of the 13th Annual AIAA/USU Conference on Small Satellites, North Logan, Utah, August, 1999*. AIAA, 1999. SSC99-IV-6.

[28] M. Rahman, H. Mahfuz, A. Haque, E. Foster, Uday Vaidya, and S. Jeelani. Static and Buckling Analysis of Composite Isogrid Cylinders Using Finite Element Approach. In *International Conference on Advanced Composites. Hurghada, Egypt, Dec 15–18, 1998*, pages 673–679. A99–22048.

[29] Singiresu S. Rao. *Mechanical Vibrations, Second Edition*. Addison Wesley, Reading, MA, 1990.

[30] Thomas Sarafin. Designing Effective Static Tests for Spacecraft Structures. In *35th AIAA, Aerospace Sciences Meeting and Exhibit, Reno, Nevada, January, 6-9, 1997*. AIAA, 1997. A97–0882.

[31] Thomas P. Sarafin and Wiley J. Larson, editors. *Spacecraft Structures and Mechanisms–From Concept to Launch*. Microcosm Press and Kluwer Academic Publishers, Torrance, CA, 1995.

[32] Liam Sarsfield. *The Cosmos on a Shoestring: Small Spacecraft for Space and Earth Science*. RAND, Santa Monica, CA, 1998.

[33] Edward Silverman, Marvin Rhodes, and Jack Dyer. Composite Isogrid Structures for Spacecraft Components. *SAMPE Journal*, 35:51–59, 1999. no. 1, January–February.

[34] Paul Slysh. Expert System for Generation of Flat Patterns of Isogrid Shell Structures with Circular Bosses. In *SAWE Annual Conference, Dallas, Texas, May 20–22, 1985*. Society of Allied Weight Engineers. SAWE Paper No. 1675.

[35] Paul Slysh. Isogrid Structural Applications. In *SAWE Annual Conference, Philadelphia, Pennsylvania, May 24–26, 1976*. Society of Allied Weight Engineers. SAWE Paper No. 1096.

[36] Space Dynamics Laboratory, Logan, UT. *Isogrid Microspacecraft Structures Final Report*, 1994. SDL/94-037.

[37] Craig L. Stevens, Jana L. Schwartz, and Christopher D. Hall. Design and System Identification of a Nanosatellite Structure. In *2001 AAS/AIAA Astrodynamics Specialists Conference, Quebec City, Canada, Jul. 30–Aug. 2, 2001*. AAS/AIAA, 2002. AAS 01-352.

[38] Structural Dynamics Research Corporation, Milford, OH. *I-DEAS General Capabilities User's Guide*, 2001.

[39] US Department of Defense, Washington, DC. *Military Handbook: Metallic Materials And Elements For Aerospace Vehicle Structures*, 1990. MIL-HDBK-5H.

[40] US Department of Defense, Washington, DC. *Military Specification: Chemical Conversion Coatings on Aluminum and Aluminum Alloys*, 1990. MIL-C-5541E.

[41] S. S. Wang, S. Srinivasan, K. B. SU, and M. G. Dunham. Buckling and Postbuckling of Isogrid–Stiffened Fiber Composite Laminate Shells: Analyses and Experiments. In *American Society for Composites, Technical Conference, 9th, University of Deleware, Newark, Sept. 20–22, 1994*, pages 1182–1191.

[42] Steve Wasserzug. *Presentation and Private Correspondence.* NASA Goddard Space Flight Center, Greenbelt, MD, 1999. NASA/AFRL Space Shuttle Payload Safety Workshop.

[43] James R. Wertz and Wiley J. Larson, editors. *Space Mission Analysis and Design.* Microcosm Press and Kluwer Academic Publishers, Torrance, CA, 1992.

[44] Andrew Wilson. *Jane's Space Directory: 11th Edition.* Jane's Information Group Limited, Surrey, UK, 1995.

[45] Carl Wood, Dave Forrest, Brian McKinnon, and Dean Nelson. CATSAT Structural Design. In *10th Annual AIAA Utah State University Conference on Small Satellites, Logan, Utah, Sept., 1996.*

[46] Zhimin Zhang, Ming Feng, and Suzhen You. An Analysis of Nonlinear Post–Buckling for Laminated Composite Cylindrical Shells with Inside Triangular Isogrid Stiffners. In *Proceedings of the 7th Annual International Conference on Composite Materials, Guangzhou, China, Nov. 22–24, 1989*, volume 3, pages 236–243.

Appendix A

Finite Element Analysis Results

The appendix contains plots of the stress contours obtained in the sine burst test finite element analysis. Both the shell stresses and rib stresses are plotted. The results shown are the Von–Mises stresses calculated in the analysis.

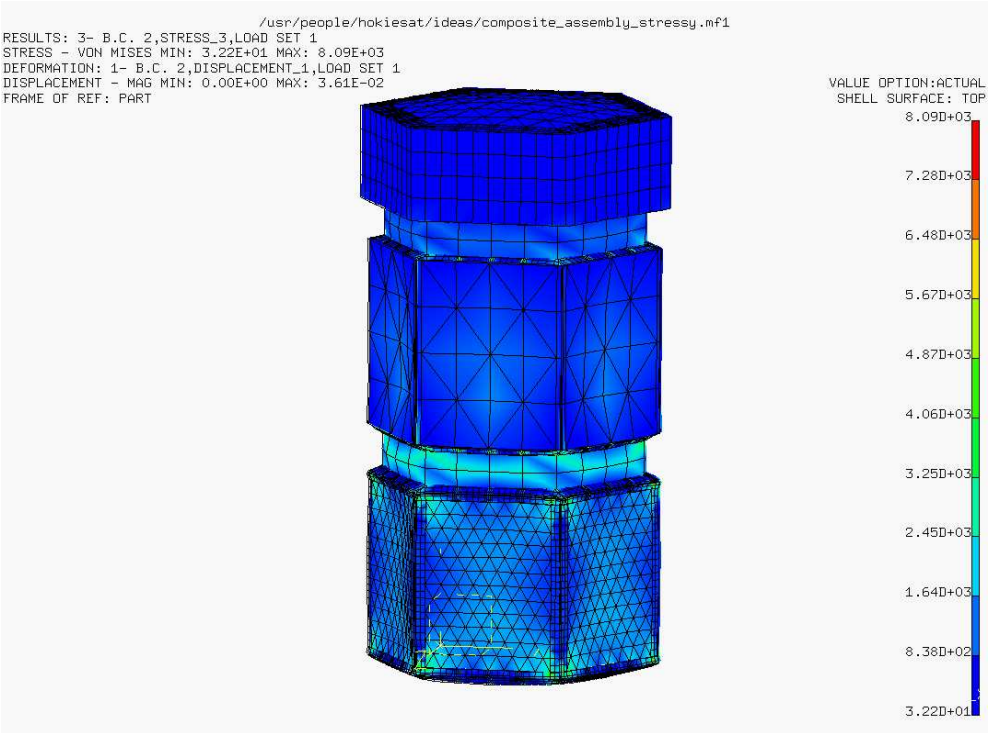

Figure A.1: Sine Burst Stress Analysis (y–axis)

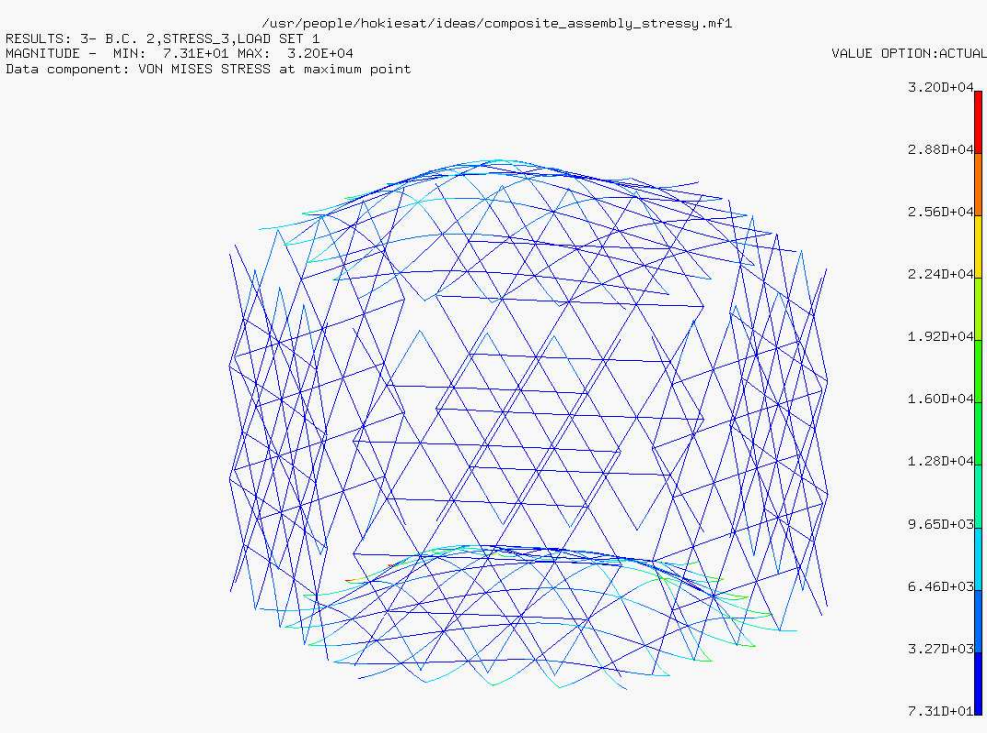

Figure A.2: Sine Burst Rib Stress Analysis (y–axis)

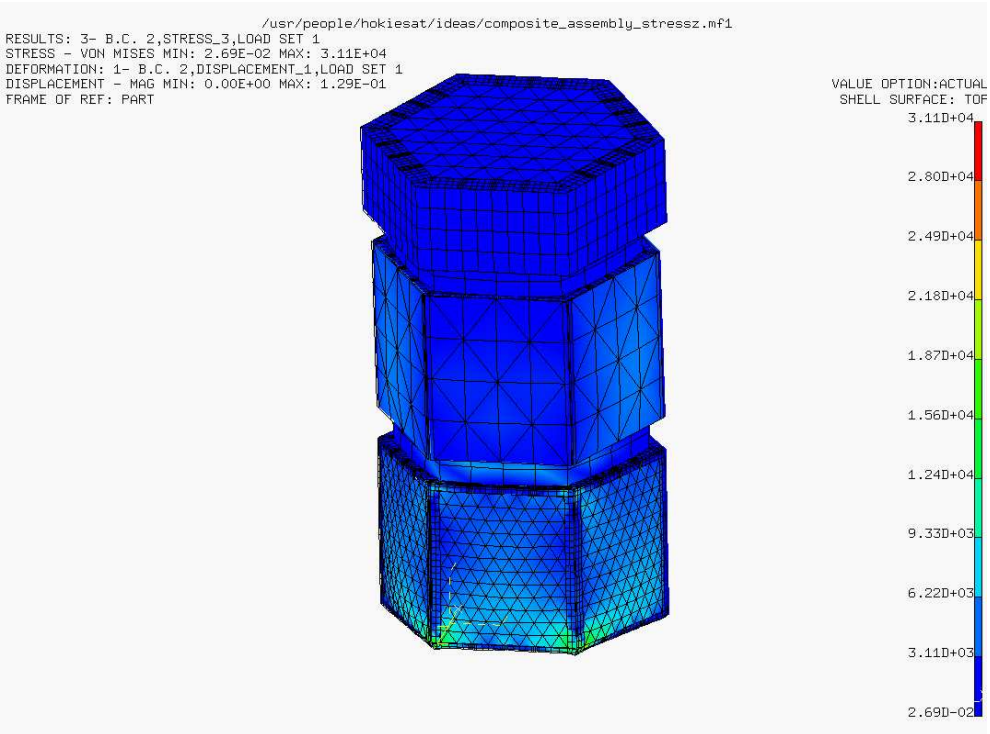

Figure A.3: Sine Burst Stress Analysis (z–axis)

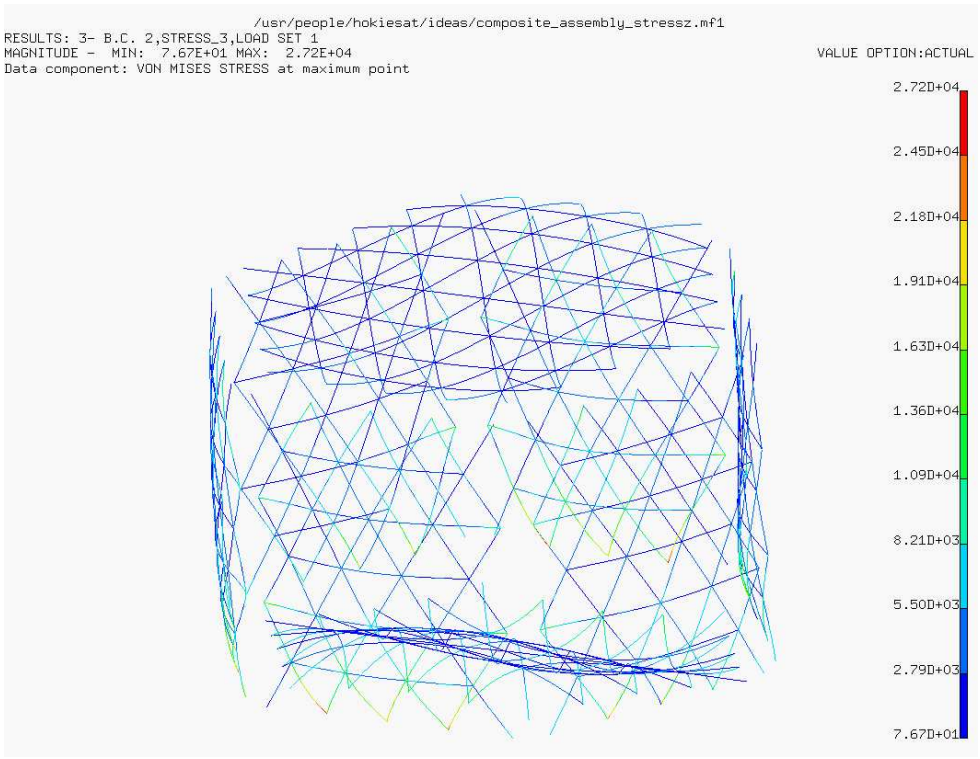

Figure A.4: Sine Burst Rib Stress Analysis (z–axis)

Vita

The author was born in Willingboro, NJ. He was raised on the Eastern Shore of Virginia in the town of Onancock. He attended Nandua High School where he graduated with honors in the Spring of 1996. He attended the engineering school at Virginia Tech in the Fall of that year. Craig entered the aerospace program in the Spring of 1998. He later became involved in the HokieSat project as an undergraduate in the Spring of 1999. The author was originally part of the structures and tether teams. He conducted research in spacecraft tether dynamics while serving as the structures system leader. In the Spring of 2000, Craig graduated from Virginia Tech, receiving a bachelor's degree in aerospace engineering. He remained at Virginia Tech and continued spacecraft structures research while pursuing his master's degree in aerospace engineering. Craig will attend NASA Goddard Space Flight Center in Greenbelt, Maryland where he will continue spacecraft structural research in the Mechanical Systems Analysis Branch. Craig is a member of the Sigma Gamma Tau aerospace honor society.